



# **EXHAUST PLUME TEMPERATURE EFFECTS ON NOZZLE AFTERBODY PERFORMANCE OVER THE TRANSONIC MACH NUMBER RANGE**

**C. E. Robinson and M. D. High**  
**ARO, Inc.**

**July 1974**

Approved for public release; distribution unlimited.

**PROPULSION WIND TUNNEL FACILITY**  
**ARNOLD ENGINEERING DEVELOPMENT CENTER**  
**AIR FORCE SYSTEMS COMMAND**  
**ARNOLD AIR FORCE STATION, TENNESSEE**

# ***NOTICES***

When U. S. Government drawings, specifications, or other data are used for any purpose other than a definitely related Government procurement operation, the Government thereby incurs no responsibility nor any obligation whatsoever, and the fact that the Government may have formulated, furnished, or in any way supplied the said drawings, specifications, or other data, is not to be regarded by implication or otherwise, or in any manner licensing the holder or any other person or corporation, or conveying any rights or permission to manufacture, use, or sell any patented invention that may in any way be related thereto.

Qualified users may obtain copies of this report from the Defense Documentation Center.

References to named commercial products in this report are not to be considered in any sense as an endorsement of the product by the United States Air Force or the Government.

**EXHAUST PLUME TEMPERATURE EFFECTS ON  
NOZZLE AFTERBODY PERFORMANCE OVER  
THE TRANSONIC MACH NUMBER RANGE**

**C. E. Robinson and M. D. High  
ARO, Inc.**

Approved for public release; distribution unlimited.

## FOREWORD

The work reported herein was conducted by the Arnold Engineering Development Center (AEDC) under joint sponsorship of the Air Force Flight Dynamics Laboratory (AFFDL) and AEDC, Air Force Systems Command (AFSC), under Program Element 63741F, Project 5975.

The experimental and analytical results presented were obtained by ARO, Inc. (a subsidiary of Sverdrup & Parcel and Associates, Inc.), contract operator of AEDC, AFSC, Arnold Air Force Station, Tennessee. The tests were conducted from April 4 through 6, 1972, under ARO Project No. PB0281 in support of Research Project No. PW5263 and from April 9 through 11, 1973, under ARO Project No. PF220. The manuscript was submitted for publication on August 13, 1973.

This technical report has been reviewed and is approved.

ELTON R. THOMPSON  
Research and Development  
Division  
Directorate of Technology

ROBERT O. DIETZ  
Director of Technology

## ABSTRACT

Results of an experimental and analytical research investigation on nozzle/afterbody drag are presented. Experimental afterbody (and boattail) drag coefficients and pressure distributions are discussed for an isolated, strut-mounted nozzle/afterbody model for the Mach number range from 0.6 to 1.5. Some data are also given for free-stream unit Reynolds numbers from one million to approximately four million per foot. The experimental data were obtained for the basic model with an air-cooled and a water-cooled Ethylene<sup>®</sup>/air combustor to provide hot-jet duplication as well as cold-jet simulation. The temperature of the nozzle exhaust gas was varied from 530°R (burner off) to approximately 2500°R for several nozzle pressure ratios from jet off to those corresponding to a moderately under-expanded exhaust plume. The initial series of experiments was conducted with the air-cooled combustor, and the effect of jet temperature on afterbody drag was somewhat masked by the effects of the secondary airflow from the cooling air. The general trend, however, shows a decreasing afterbody drag with increasing exhaust gas temperature and with decreasing secondary airflow at a fixed nozzle pressure ratio. The results from the water-cooled combustor show similar trends with increasing exhaust jet temperature. The differences between the cold-jet and hot-jet results are significant, and adjusting the cold-jet pressure ratio to correct for the changes in the jet specific heat ratio with temperature will account for most of the differences observed. A parallel analytical investigation is described which attempts to predict the afterbody drag of isolated nozzle/afterbody configurations. The effort to date has been moderately successful in accounting for the exhaust plume displacement effects (both those which occur because of the inviscid expansion and those which occur because of plume mixing) at free-stream conditions where subsonic flow exists over the entire afterbody. The analytical procedures used, with their merits and shortcomings, are discussed.

## CONTENTS

	<u>Page</u>
ABSTRACT . . . . .	iii
NOMENCLATURE . . . . .	vii
I. INTRODUCTION . . . . .	1
II. APPARATUS . . . . .	
2.1 Wind Tunnel . . . . .	2
2.2 Experimental Hardware . . . . .	2
2.3 Instrumentation . . . . .	4
III. PROCEDURES . . . . .	
3.1 Experimental Procedures . . . . .	5
3.2 Data Reduction Procedures . . . . .	6
IV. EXPERIMENTAL RESULTS . . . . .	
4.1 General . . . . .	8
4.2 Water-Cooled Combustor Configuration (Phase II) . . . . .	9
4.3 Air-Cooled Combustor Configuration (Phase I) . . . . .	12
V. THEORETICAL ANALYSIS . . . . .	
5.1 Physical Statement of Problem . . . . .	13
5.2 Numerical Methods . . . . .	14
5.3 Comparison of Theory and Experimental Results . . . . .	15
VI. CONCLUSIONS . . . . .	18
REFERENCES . . . . .	19

## APPENDIXES

## I. ILLUSTRATIONS

Figure

1. Basic Model Dimensions and Location in Test Section . . . . .	23
2. Model Installation Photographs . . . . .	24
3. Combustor Details . . . . .	26
4. Model Internal Details . . . . .	28
5. Schematic of Nozzle Configurations and Nozzle Pressure Instrumentation . . . . .	30
6. Range of Nozzle Total Pressure Ratio . . . . .	31
7. Comparison of Pressure Integration Boattail Drag Coefficient with Force Balance Boattail Drag Coefficient at $M_\infty = 1.2$ and $Re = 2.5 \times 10^6/ft$ . . . . .	31
8. Typical Boattail Static Pressure Distributions . . . . .	32
9. Typical Schlieren Photographs at $M_\infty = 1.1$ and $Re = 2.5 \times 10^6/ft$ . . . . .	37

<u>Figure</u>	<u>Page</u>
10. Effect of Nozzle Pressure Ratio on Turbojet Nozzle Component Drag Coefficients at Various Exhaust Jet Temperatures Using a Water-Cooled Combustor at $Re = 2.5 \times 10^6/ft$ . . . . .	40
11. Qualitative Effect of Entrainment and Plume Shape on Boattail Drag . . . . .	45
12. Comparison of the Cold-Flow Data Corrected for Specific Heat Ratios to the Experimental Hot-Flow Data at $Re = 2.5 \times 10^6/ft$ . . . . .	46
13. Comparison of Two Methods of Presenting Drag Coefficient Data . . . . .	48
14. Effect of Reynolds Number on Boattail Pressure Distribution at $M_\infty = 0.6$ . . . . .	49
15. Effect of Reynolds Number on Boattail Pressure Drag Coefficient at Various Exhaust Jet Temperatures Using a Water-Cooled Combustor at a Nozzle Pressure Ratio of 1.5 . . . . .	50
16. Effect of Nozzle Pressure Ratio on Component Drag Coefficients at Various Reynolds Numbers Using a Water-Cooled Combustor . . . . .	51
17. Comparison of Boattail Drag Coefficient Levels Using Water-Cooled and Air-Cooled Combustors at $M_\infty = 0.9$ . . . . .	56
18. Military Nozzle Internal Pressure Distribution Cold Flow Using an Air-Cooled Combustor . . . . .	57
19. Effect of Secondary Airflow Ratio on Transverse Nozzle Static Pressure Using an Air-Cooled Combustor . . . . .	58
20. Effect of Secondary Airflow Ratio on Turbojet Nozzle Component Drag Coefficients, Cold Flow, Using an Air-Cooled Combustor at $Re = 2.5 \times 10^6/ft$ . . . . .	59
21. Effect of Nozzle Pressure Ratio on Turbojet Nozzle Component Drag Coefficients at Various Exhaust Jet Temperatures Using an Air-Cooled Combustor at $Re = 2.5 \times 10^6/ft$ . . . . .	61
22. Effect of Nozzle Pressure Ratio on Turbofan Nozzle Component Drag Coefficients at Various Exhaust Jet Temperatures Using an Air-Cooled Combustor . . . . .	66
23. Schematic of the Various Flow Regions Involved in the Afterbody Drag Calculation Problem . . . . .	71
24. Effective Displacement Boundaries for the External Flow at $M_\infty = 0.6$ and $Re = 2.5 \times 10^6/ft$ . . . . .	72
25. Effective Displacement Boundaries for the External Flow at $M_\infty = 0.9$ and $Re = 2.5 \times 10^6/ft$ . . . . .	73
26. Afterbody Pressure Distribution: Comparison Between Experiment and Theory for Various Plume Temperatures at $M_\infty = 0.6$ and $Re = 2.5 \times 10^6/ft$ . . . . .	74

<u>Figure</u>	<u>Page</u>
27. Afterbody Pressure Distribution: Comparison Between Experiment and Theory for Various Plume Temperatures at $M_\infty = 0.9$ and $Re = 2.5 \times 10^6/ft$ . . . . .	75
28. Comparison of Theoretical and Experimental Boattail Drag Coefficients at $Re = 2.5 \times 10^6/ft$ . . . . .	76
29. Afterbody Pressure Distribution: Comparison Between Experiment and Theory for $M_\infty = 1.2$ and $Re = 2.5 \times 10^6/ft$ . . . . .	77

## II. TABLES

I. Measurement Uncertainty . . . . .	78
II. Nozzle Boattail Surface Pressure Instrumentation . . . . .	79
III. Forebody and Afterbody Surface Pressure Instrumentation . . . . .	80
IV. Boundary Conditions . . . . .	81
V. Computational Methods . . . . .	81

## NOMENCLATURE

$A_i$	Boattail incremental surface area, $ft^2$
BPR	Bypass ratio
$C_{DAB}$	Afterbody drag coefficient based on body cross-sectional area
$C_{DBT}$	Boattail drag coefficient based on body cross-sectional area
$C_{DBTF}$	Boattail friction drag coefficient based on body cross-sectional area
$C_{DBTP}$	Boattail pressure drag coefficient based on body cross-sectional area
$C_{DT}$	Total drag coefficient based on body cross-sectional area
$C_{DTP}$	Total pressure drag coefficient
$C_{FB}$	Average skin-friction coefficient
$C_{Fi}$	Local skin-friction coefficient
$C_p$	Pressure coefficient
$D_{BTF}$	Boattail integrated friction drag force, lbf
$D_{BTFs}$	Boattail incremental friction drag force, lbf



$D_{BTpp}$	Boattail integrated pressure drag force, lbf
$F_A$	Balance axial force, lbf
$F_N$	Balance normal force, lbf
$F_Y$	Balance side force, lbf
$f/a$	Combustor fuel/air ratio
$M_m$	Balance moment force, in.-lbf
$M_\infty$	Free-stream Mach number
MOC	Method of characteristics
NPR	Nozzle pressure ratio ( $p_{tj}/p_\infty$ )
$p_{cs}$	Combustion chamber static pressure, psia (Fig. 5c)
$p_{E3}$	Nozzle exit static pressure at 15-deg radial position from top (air-cooled model), psia
$p_{E5C}$	Nozzle exit static pressure, calculated (water-cooled model), psia
$p_{E6}$	Nozzle exit static pressure at 200-deg radial position from top (air-cooled model), psia
$p_e$	Nozzle exit static pressure (water-cooled model), psia
$p_{eav}$	Nozzle exit static pressure [ $\frac{1}{2}(p_{E3} + p_{E6})$ ] air-cooled model, psia
$p_i$	Boattail surface pressure at incremental position $i$ ( $i$ ranges from 403 to 448; see Table II), psia
$p_{t\infty}$	Total pressure, psia
$p_{tj}$	Total jet pressure, psia
$p_\infty$	Free-stream static pressure, psia
$q_l$	Local dynamic pressure, psf
$q_\infty$	Free-stream dynamic pressure, psf

$Re$	Reynolds number per foot
$Re_i$	Local Reynolds number on afterbody and boattail
Region A	Nozzle internal flow (see Fig. 26)
Region B	Model external flow (see Fig. 26)
Region C	Nozzle internal boundary layer (see Fig. 26)
Region D	Model external boundary layer (see Fig. 26)
Region E	Plume and external flow mixing layer (see Fig. 26)
$S$	Cross-sectional area based on maximum diameter of model (76.387 in. <sup>2</sup> )
$S_i$	Boattail incremental projected area, ft <sup>2</sup>
STA.	Model station from model theoretical nose, in.
$T_{AV}$	Mass-averaged exhaust gas temperature
$T_{GAS}$	Exhaust gas temperature, °R
$W_1$	Primary airflow rate, lbm/sec
$W_2$	Secondary airflow rate, lbm/sec
$\gamma$	Ratio of specific heats, $C_p/C_v$
$\Delta C_D$	Change in boattail drag coefficient, jet on to jet off
$\delta$	Boundary-layer displacement thickness, ft
$\theta$	Local boattail surface angle, deg

## SECTION I INTRODUCTION

A significant amount of testing is involved in developing a new aircraft and power plant. Traditionally, airframe tests have been carried out with careful simulation of the external flow over the airframe but with a rather approximate simulation of the flow issuing from the engine. Similarly, engine tests have been conducted with very careful simulation of the flows internal to the engine but with little or no consideration of the external flow.

In order to properly evaluate afterbody drag, realistic simulation of the internal as well as the external flow is required. The hot-jet exhaust simulation is generally obtained by using a cold fluid (e.g., unheated air) and adjusting the nozzle pressure ratio to match the hot-jet initial inclination angle. Such a procedure then attempts to account for the differences in the plume expansion caused by changes in the jet specific heat ratios with exhaust gas temperature. The plume displacement effects which are simulated in the above manner are inviscid in nature, and although in theory the inviscid plume boundaries are simulated, the effective jet boundaries will differ because of the viscous mixing at the interface of the exhaust flow and the external boattail flow. The nature of the viscous region depends largely on the gradients existing between the internal nozzle flow and the external flow over the afterbody. To investigate this viscous-inviscid interaction, which is particularly strong at transonic speeds, it is necessary to duplicate rather than simulate the engine exhaust gases. The research reported herein is a parallel experimental and analytical effort to determine the effects of the hot jet on the boattail drag. The analytical investigation is a continuing effort to predict the afterbody drag on nozzle/afterbody models. These predictions will have to ultimately account for the effect of jet entrainment of the boattail flow as well as the plume displacements caused by viscous mixing on the afterbody drag. With sufficiently accurate prediction techniques available, the proper procedure for simulating a hot-jet exhaust flow with a cold fluid may be developed.

The experimental portion of the research reported herein was conducted in two phases, which were differentiated by the combustor design. Phase I was conducted using an air/ethylene combustor which had air cooling around the combustor liner. During the Phase I investigation, it was observed that the secondary airflow (cooling air) affected the boattail pressure distribution, hence producing drag. This effect opposed the trends resulting from the introduction of the hot jet. Because of the secondary airflow effect, the water-cooled combustor was designed (Phase II) to eliminate secondary airflow and isolate the jet exhaust temperature effect on boattail and afterbody drag. During Phase I, two nozzle configurations representing a typical turbojet nozzle installation and a typical turbofan with low-bypass (1:1) nozzle installation at a military power setting were used. The Phase II investigation utilized the turbojet nozzle installation at a military power setting. Data were obtained for these configurations over the transonic Mach number range.

## SECTION II APPARATUS

### 2.1 WIND TUNNEL

The AEDC 16-Ft Propulsion Wind Tunnel (16T) is a continuous flow, closed-circuit wind tunnel capable of operation within a Mach number range from 0.20 to 1.60. Tunnel 16T can be operated within a stagnation pressure range from 120 to 4000 psfa, depending on Mach number, with a stagnation temperature variation capability from approximately 80°F to a maximum of 160°F. Tunnel air is removed and replaced with conditioned make-up air from an atmospheric dryer to facilitate control of vitiation caused by combustion and to control the specific humidity of the tunnel air.

### 2.2 EXPERIMENTAL HARDWARE

7/5 = 1.22  
The experimental hardware used during the investigation reported herein was the Air Force Flight Dynamics Laboratory (AFFDL)/Lockheed isolated nozzle model previously used for cold-flow nozzle studies. The model, described fully in Ref. 1, was modified to accommodate an Ethylene®/air combustor, which was used to provide hot exhaust jet duplication of a typical turbojet operation (Section 2.2.1). The AFFDL/Lockheed isolated nozzle model is an axisymmetric body with an overall length of approximately 153 in. The model had a 14-deg, half-angle conical nose, which was faired into the primary model diameter of 9.86 in. A boundary-layer trip consisting of 0.055-in.-diam steel spheres spot-welded to a trip ring at a circumferential spacing of four sphere diameters was located on the conical nose 12 in. aft of the cone vertex. The external surfaces of the afterbody and boattail used were the AFFDL/Lockheed configuration CDE1 (Convergent-Divergent Ejector, military power setting) described in Ref. 2. The model was mounted in Tunnel 16T on a strut with an aft sweep angle of 31.8 deg. A sketch showing the basic external model dimensions and the model location in the wind tunnel test section is shown in Fig. 1 (Appendix I). Installation photographs of the model are presented in Fig. 2.

The internal model configurations deviated from the AFFDL/Lockheed CDE1 configuration in order to accommodate the combustor. High-pressure air, which was used to simulate the nozzle exhaust for the cold-flow portion of testing and which was used as an oxidizer in the combustion of Ethylene, was ducted through the strut to a plenum in the forward section of the model.

#### 2.2.1 Combustor

An Ethylene/air combustor based on a National Advisory Committee for Aeronautics (NACA) design (Ref. 2) was used to provide hot exhaust jet duplication. (Ethylene ( $C_2H_4$ ) is a gaseous hydrocarbon fuel which, when burned in air, produces exhaust products which

very closely duplicate the exhaust products of JP-4 burned in air.) Two combustor configurations were used during the experimental investigation. The overall dimensions of the two configurations were similar, and many components were interchangeable. The first combustor used secondary airflow for cooling the combustor liner and nozzle, whereas the second combustor and nozzle were water cooled.

The flow straighteners forward of the combustor and the flameholder were the same for both combustors. The flameholder consisted of four doughnut rings interconnected with fuel flow passages, and the forward doughnut ring served as the fuel injection ring. Ignition was accomplished by injecting a small quantity of tri-ethyl borane (TEB, a pyrophoric fuel) into a retainer mounted on the flameholder. Flow mixers were placed at the rear of the flameholder at radial positions of 45, 135, 225, and 315 deg (0 deg represented the top of the model) to mix the hot flow from the combustion zone with the air around the outside of the flameholders. This was done for both combustors to provide a uniform temperature profile at the exit of the combustor. The physical differences in these configurations because of the different cooling schemes is explained in the following paragraphs. A schematic of the basic burner and a photograph of the flameholder are shown in Fig. 3.

#### **2.2.1.1 Air-Cooled Combustor**

The air-cooled combustor liner was constructed from stainless steel and had an overall length of 27.45 in., an inside diameter of 6.15 in., and a wall thickness of 0.125 in. (Fig. 4a). The combustor liner terminated in a sonic throat with a contraction ratio of 2.36. Secondary airflow for cooling was ducted to the secondary flow annulus from the primary stream through a variable position sleeve valve (Fig. 4a). The two air streams, primary and secondary, were mixed at the exit plane of the combustor sonic nozzle and were exited through the common nozzle. Flow conditioners in both the primary and the secondary air streams were used to provide a uniform flow field to the combustor and secondary flow annulus, respectively.

#### **2.2.1.2 Water-Cooled Combustor**

The water-cooled combustor was constructed from copper with an inside diameter of 6.15 in. and a wall thickness of 0.125 in. (Fig. 4b). The combustor terminated with a convergent-divergent nozzle with a throat diameter of 3.6 in. The contraction ratio for this combustor was 2.92. Cooling water was supplied to the combustor through the model strut and flow passages internal to the model (Fig. 4b). A continuous water flow rate of 70 gal/min was maintained throughout the investigation.

#### **2.2.2 Nozzle Configurations**

Two nozzle configurations were used in conjunction with the air-cooled combustor. Each configuration utilized the AFFDL/Lockheed convergent-divergent ejector afterbody and boattail external surfaces (Configuration CDE1) and force balances. The internal

military nozzle configuration was constructed from stainless steel and had a throat diameter of 4.8 in. and an expansion ratio of 1.0, with a length-to-diameter ratio of 1.25 (Fig. 5a). Since the burner was operated choked, the effective area ratio of the nozzle was 1.44 for this configuration. A secondary air passage sleeve was used to reduce the annulus area around the combustor, thereby restricting the secondary airflow to just the amount required for cooling the combustor liner (approximately 15 percent of primary airflow). The secondary air passage sleeve was removed for the 1:1 bypass nozzle configuration, allowing a secondary airflow rate nearly equal to the primary stream. The 1:1 bypass nozzle configuration was also constructed of stainless steel and had an expansion ratio of 1.06 (Fig. 5b). The nozzle was preceded by a 7.5-in. mixing chamber to better simulate the mixing region of the hot core and cold annulus air experienced in turbofan engines.

The internal nozzle configuration used with the water-cooled combustor was a convergent-divergent (CD) military nozzle with a nominal design area ratio of 1.43 and a divergence angle of 6.4 deg. Because of design requirements imposed by water cooling, the base area (4.78 in.<sup>2</sup>) of the CD nozzle was significantly larger than the air-cooled military turbojet nozzle (Fig. 5c).

## 2.3 INSTRUMENTATION

Critical flow venturi meters were used to measure the total air and Ethylene flows. Secondary airflow rate for the air-cooled combustor was determined from pressure and temperature measurements in the secondary flow annulus at a known cross-sectional area. The primary airflow was then found by subtracting the secondary airflow from the total airflow through the venturi.

Two thin-walled cylindrical ring force balances were used on the air-cooled combustor configuration for measurement of nozzle external drag and nacelle afterbody drag, respectively. The balances contained metallic bellows seals that prevented air from leaking through the balance flexures. For each of the two cylindrical ring balances, the effective area of the bellows, which was determined from balance calibration, was used to make appropriate pressure-area corrections to the balance data. Static pressures along the body external surfaces were also measured.

The combustion chamber pressure probe was located adjacent to the tri-ethyl borane line (Fig. 3). The military nozzle air-cooled combustor configuration had six static pressure orifices at approximately the 15- and 200-deg radial locations (two rows of three orifices located internally, approximately 180 deg apart). The 1:1 bypass nozzle had only four nozzle static pressure orifices, with an additional total and static pressure measurement made in the secondary flow passage. The location of the internal pressure instrumentation for the two air-cooled combustor nozzles is shown in Figs. 5a and b. In addition, the water-cooled combustor configuration was instrumented with three static pressure orifices in the combustor and two static pressure orifices in the divergent nozzle (Fig. 5c).

Measurement uncertainty values are presented in Table I (Appendix II) for some of the more important parameters.

## SECTION III PROCEDURES

### 3.1 EXPERIMENTAL PROCEDURES

The experimental investigation was divided into two phases. Phase I utilized the air-cooled combustor configuration and the two associated nozzles, whereas Phase II utilized the water-cooled combustor configuration. The experimental procedures were slightly different for these two phases and will be enumerated separately.

#### Phase I Procedure

1. Wind tunnel Mach number and Reynolds number conditions were established, and jet-off data were obtained.
2. Cold flow was established through the model at a specified setting of the secondary airflow rotating sleeve valve, and a series of nozzle pressure ratios were set. Data were obtained at each ratio.
3. The total airflow through the model was fixed, and the rotating sleeve valve was varied from its fully closed to its fully open position to obtain secondary airflow effects. This was usually done at a nozzle pressure ratio near that set for hot-flow operation.
4. The combustor mixture was ignited and, for a given fuel/air ratio, a nozzle static pressure ratio was set (using  $p_{E3}/p_{\infty}$  as the controlling ratio). Data were obtained at four basic fuel/air ratios as near to the same nozzle pressure ratio as possible.

When setting the selected pressure ratio with the hot flow, both the fuel and the airflow were varied at a given fuel/air ratio.

#### Phase II Procedure

1. Wind tunnel Mach number and Reynolds number conditions were established, and jet-off data were obtained.
2. Cold flow was established through the model, and a series of nozzle pressure ratios were set. Data were obtained at each ratio.
3. The combustor mixture was ignited, and the fuel/air ratio was set to obtain the desired temperature. A series of nozzle pressure ratios were set by varying fuel and airflow to maintain a constant fuel/air ratio. Data were obtained at each nozzle pressure ratio. The nozzle pressure ratio survey was conducted at four fuel/air ratios.

Schlieren photographs were obtained at each of the nozzle pressure ratios for the hot exhaust jet duplication and at selected pressure ratios for the cold exhaust jet simulation.

### 3.2 DATA REDUCTION PROCEDURES

The primary performance parameters presented in this report are the afterbody and boattail drag coefficients obtained from an integration of the experimental pressure distributions and the computed skin friction. Both drag coefficients were calculated using similar relationships. The relationships used in calculating the boattail drag coefficient are presented here to demonstrate the general technique employed.

$$C_{DBT} = C_{DBTp} + C_{DBTF} \quad (1)$$

The pressure drag coefficient is

$$C_{DBTp} = \frac{144 (D_{BTpp})}{q_{\infty} S} \quad (2)$$

where  $q_{\infty}$  is the free-stream dynamic pressure and  $S$  is the projected area based on the maximum diameter of the model. The boattail pressure drag ( $D_{BTpp}$ ) is calculated from the experimental pressures by the following equation:

$$D_{BTpp} = 0.210486 p_{\infty} - \sum_{i=403}^{i=448} p_i S_i \quad (3)$$

Here,  $i$  represents an individual pressure measurement location (see Tables II and III);  $p_i$  is the experimental pressure, and  $S_i$  is the projected area over which the measured pressure acts. The friction drag coefficient is calculated from the relationship

$$C_{DBTF} = \frac{144 (D_{BTF})}{q_{\infty} S} \quad (4)$$

where  $D_{BTF}$  is the total friction force obtained by summation of the incremental friction forces

$$D_{BTF} = \sum_{i=403}^{i=448} (C_{FB}) (q\ell) (A_i) (\cos \theta_i) \quad (5)$$

where  $C_{FB}$  is the average skin-friction coefficient based on the local Reynolds number,  $q\ell$  is the local dynamic pressure,  $A_i$  is the area of the external surface segment, and  $\theta_i$  is the local boattail surface angle. The afterbody friction drag coefficient is obtained from the empirical correlation of local skin-friction coefficient versus Reynolds number



developed by Sivells and Payne (Ref. 3) for incompressible turbulent flow over a flat plate with zero pressure gradient.

$$C_{fi} = \frac{0.088 (\log Re_i - 2.3686)}{(\log Re_i - 1.5)^3} \quad (6)$$

The internal performance parameters of the exhaust jet were obtained in the following manner for the water-cooled and air-cooled models.

In the case of the water-cooled model, three static pressure orifices located at various axial positions in the water-cooled combustion chamber (Fig. 5c) were used to obtain the chamber static pressure. The pressure measured by the orifice farthest downstream (just ahead of the start of the throat contraction) was used to calculate the exhaust jet total pressure,  $p_{tj}$ , in the following manner:

$$p_{tj} = p_{cs} \left( \frac{p_t}{p} \right) \quad (7)$$

where  $p_t/p$  is the subsonic isentropic pressure ratio based on the chamber contraction ratio of 2.92. The isentropic pressure ratio is a weak function of the ratio of specific heats ( $p_t/p$  decreases 2.0 percent for a change in  $\gamma$  from 1.40 to 1.30). Because of this dependence on  $\gamma$ ,  $p_{tj}$  was calculated with an iteration procedure wherein the initial calculation was made using an assumed exhaust jet temperature. Exhaust jet temperature was calculated in the iteration loop using the relationship given in Eq. (8). The physical geometry of the chamber and the measured pressure and mass flow rate were used in the calculation

$$T_{Gas} = \left[ \frac{p_{tj} K_F A_T K_z}{w_t} \right]^2 \quad (8)$$

where  $K_F$  is Fleigner's constant and is a function of  $\gamma$ ,  $A_T$  is the physical throat area,  $K_z$  is the nozzle throat discharge coefficient determined from cold-flow test of the nozzle, and  $w_t$  is the total mass flow rate in the chamber. The total mass flow is given by

$$w_t = w_a + w_f \quad (9)$$

where  $w_a$  is the chamber airflow rate measured by a critical flow venturi and  $w_f$  is the ethylene flow rate calculated from the  $T_{Gas}$  value in the iteration loop and an assumed combustion efficiency of 80 percent. The entire iteration procedure was made necessary because a change in the thermodynamic quality of the gaseous ethylene (from a perfect gas to a saturated vapor) resulted in a deviation from the perfect gas law and prevented the venturi measuring system (originally designed to measure a gaseous ethylene flow) from giving accurate flow measurements.

In the case of the air-cooled model tests, the problem encountered with ethylene quality was also suspected, which made the gas temperature an unknown since fuel flow was not known. In this model the only pressure measured in the combustion chamber was made with the extra, open TEB supply line shown in Fig. 3a. This orifice did not give an accurate chamber pressure with cold flow in the chamber because of a relatively high air velocity in that region of the chamber. However, when there was combustion in the chamber a correlation of the  $p_{tj}$  calculated for the water-cooled model with the pressure measured with the TEB line showed less than a 1-percent deviation between the two. Based on this correlation, Eq. (8) was again used to compute the actual gas temperature for the hot flow conditions using the pressure from the TEB line for  $p_{tj}$ . The main uncertainty in this procedure was the discharge coefficient for the air-cooled nozzle, which was assumed equal to unity.

The complexity of the combustor and nozzle fabrication resulted in the loss of some of the nozzle pressure taps which were planned. Because of the loss of these pressure taps, two additional pressures were calculated for use in presenting the data: a calculated nozzle exit static pressure,  $p_e$ , for the water-cooled model and a measured average nozzle exit static pressure,  $p_{e_{av}}$ , for the air-cooled model. The water-cooled  $p_e$  was calculated from Eq. (10) as follows:

$$p_e = p_{tj} \left( \frac{p}{p_{tj}} \right) \quad (10)$$

where  $p/p_{tj}$  is the isentropic pressure ratio based on the effective area ratio of the nozzle (1.48) and is a function of  $\gamma$ . This calculated nozzle exit pressure was higher than the measured pressure ( $p_{E5}$ ) at the nozzle exit by approximately 2 percent. [However, the measured  $p_{E5}$  was probably reduced slightly by the low pressure in the base region of the nozzle. The nozzle exit static pressure for the air-cooled combustor configuration ( $p_{e_{av}}$ ) was taken to be the arithmetic average (Eq. 11) of the two measured pressures 180 deg apart located near the nozzle exit plane (Fig. 5a). Thus,

$$p_{e_{av}} = \frac{1}{2} (p_{E3} + p_{E6}) \quad (11)$$

## SECTION IV EXPERIMENTAL RESULTS

### 4.1 GENERAL

The experimental investigation was conducted in two phases. Phase I utilized the air-cooled combustor configuration with both a military turbojet and a 1:1 bypass military turbofan nozzle configuration. Data were obtained using the turbojet nozzle configuration at Mach numbers of 0.6, 0.9, 1.1, 1.2, and 1.5 over the nozzle pressure ratio range shown in Fig. 6 at a Reynolds number of  $2.5 \times 10^6/\text{ft}$ . Four nominal temperatures (1000°, 1500°, 2000°, and 2500°R) were investigated at each Mach number. Data were also obtained with the turbojet nozzle using cold exhaust jet simulation for comparison with the hot exhaust jet duplication.

The 1:1 bypass turbofan nozzle configuration was also investigated at Mach numbers of 0.6, 0.9, 1.1, 1.2, and 1.5 at a Reynolds number of  $2.5 \times 10^6/\text{ft}$ . Two primary stream temperatures of approximately  $1000^\circ$  and  $1500^\circ\text{R}$  were investigated. Cold exhaust jet simulation data for comparison with the hot-jet duplication conditions were also obtained. Cold- and hot-plume data (at the specified fuel/air ratios) were also obtained at a Reynolds number of  $4.75 \times 10^6/\text{ft}$  and Mach numbers of 0.6, 0.9, and 1.1.

Phase II of the experimental investigation was conducted using the water-cooled combustor configuration. The investigation was conducted at a Reynolds number of  $2.5 \times 10^6/\text{ft}$  over the same Mach number range as Phase I, at four nominal exhaust gas temperatures. The cold exhaust jet simulation conditions were repeated during Phase II for data comparison with the hot exhaust jet duplication. During Phase II, an extensive Reynolds number survey (from  $1.0 \times 10^6/\text{ft}$  to  $3.0 \times 10^6/\text{ft}$ ) was also conducted at Mach numbers of 0.6 and 0.9 over the nominal-fuel/air ratio range. Schlieren photographs were taken at selective nozzle pressure ratios to supplement the pressure data obtained during Phase II.

The afterbody and boattail drag coefficients were chosen as the primary parameters to compare nozzle/afterbody performance with hot exhaust jet duplication to the performance obtained using cold exhaust plume simulation. Two methods of determining these drag coefficients were used during Phase I. The first method utilized the force balances and measured drag force, whereas the second method obtained drag by an integration of measured pressure distribution over the afterbody and boattail with a computed skin friction added. A comparison of the boattail drag coefficients obtained using each method is shown in Fig. 7. The agreement between the two methods is good. Because of the close agreement with balance data and the ever-present possibility of balance shifts caused by the internal complexity of the model, the drag coefficients obtained by pressure integration plus a computed skin friction are presented in this report.

## 4.2 WATER-COOLED COMBUSTOR CONFIGURATION (PHASE II)

Typical pressure distributions over the boattail obtained from the water-cooled combustor are shown in Figs. 8a through d. The effect that changing the exhaust jet nozzle pressure ratio has on the boattail pressure distribution is shown in Figs. 8a and b for Mach numbers 0.9 and 1.1, respectively. For both Mach numbers, increasing the nozzle pressure ratio caused an increase in the pressure on the boattail. The effect was felt upstream of the boattail on the afterbody at Mach number 0.9 as shown by the pressure difference at the forwardmost station of the boattail. At Mach 1.1, an imbedded shock occurred on the boattail and restricted the effect of the exhaust plume to the portion of the boattail downstream of the shock. However, the shock tended to move upstream with increasing nozzle pressure ratio. The effect of exhaust plume temperature on pressure distribution at Mach numbers 0.9 and 1.1 is shown in Figs. 8c and d. Increasing exhaust temperature generally causes an increase in pressure on the boattail at Mach number 0.9, with the effect being felt on the afterbody as well. At Mach 1.1, the imbedded shock limited the effect of temperature to the segment of the boattail downstream of

the shock location. To illustrate the extent of the influence of the exhaust plume, the pressure distribution along essentially the entire model length is shown in Fig. 8e for the conditions given in Fig. 8a. Schlieren photographs at the three exhaust plume temperatures shown in Fig. 8d at Mach number 1.1 are presented in Figs. 9a through c.

The component drag coefficients (boattail drag coefficient,  $C_{DBT}$ , afterbody drag coefficient,  $C_{DAB}$ , and total drag coefficient,  $C_{DT}$ —which is the sum of  $C_{DBT}$  and  $C_{DAB}$ ) as a function of nozzle pressure ratio for each of the five Mach numbers and a Reynolds number of  $2.5 \times 10^6/\text{ft}$  are shown in Figs. 10a through e. In each case, the cold-plume simulation data are presented with the varying hot-plume duplication for comparison. Above a nozzle pressure ratio of 5.66 (nozzle completely filled),  $C_{DBT}$  decreased with increasing pressure ratio. The level of drag coefficient obtained with the hot-exhaust duplication at a given nozzle pressure ratio generally decreased with increasing exhaust temperature. At the subsonic Mach numbers 0.6 and 0.9, the afterbody drag coefficient,  $C_{DAB}$ , decreased slightly with both pressure ratio and exhaust plume temperature increases (Figs. 10a and b). At the supersonic Mach numbers of 1.1, 1.2, and 1.5, however,  $C_{DAB}$  was completely insensitive to changes in either of the variables. This insensitivity to pressure ratio and exhaust plume temperature changes is caused by the inability of the pressure ratio and temperature effects to move upstream of the imbedded shock on the boattail (Figs. 8b and d).

The mechanism which governed the behavior of boattail drag was investigated by Bergman in Ref. 4. The qualitative results of his investigation are presented in Fig. 11. Bergman proposed that the boattail drag coefficient (cold flow) was dominated by two physical effects. The first was a displacement outward of the external flow streamlines caused by the exhaust plume emitting from the model nozzle. The outward displacement of the streamlines resulted in stronger flow recompression on the boattail and thereby had a beneficial effect on drag. The shape of the exhaust plume is a function of nozzle pressure ratio for fixed tunnel conditions. The second effect, entrainment, began when the exhaust plume velocity was approximately equal to free-stream velocity. It increased boattail drag by increasing boattail velocity and effectively lowering the boattail pressure. The net effect on boattail drag is a superposition of the two effects.

The cold-flow  $C_{DBT}$  obtained during this investigation had the general shape and characteristics obtained by Bergman (Fig. 10a). No data were obtained at the low nozzle pressure ratios (less than 4.0) with a hot exhaust; however, it is hypothesized that the general behavior will be retained at the higher temperatures. For a fixed pressure ratio, the hot exhaust plume will spread more than the cold plume, causing a lower drag on the boattail. The effect of exhaust plume temperature on entrainment is unknown, however, and the entire problem is the subject of a continuing analytical investigation guided by the experimental data obtained during this investigation.

#### 4.2.1 Matching of the Plume Inclination Angle

If the changes in boattail drag caused by changes in nozzle pressure ratio are primarily inviscid in nature (i.e., caused by changes in the inviscid plume shape), then corrections to the cold flow nozzle pressure ratio can be made to simulate the change in plume shape produced by changes in the exhaust gas temperature. The effect of increasing the exhaust gas temperature is to decrease the specific heat ratio ( $\gamma$ ) of the exhaust gas with a resulting increase in the exhaust plume initial inclination angle and maximum diameter. Thus, in order to simulate a hot-jet plume ( $\gamma < 1.4$ ) operating at a given pressure ratio using cold air ( $\gamma = 1.4$ ), the nozzle pressure ratio must be increased to offset the effect of  $\gamma$ . The correction for  $\gamma$  effects is to adjust the nozzle pressure ratio at a constant value of drag coefficient to match initial jet inclination angles. The measured performance with the theoretical change in the nozzle pressure ratio predicted from changes in  $\gamma$  at the five free-stream Mach numbers investigated are compared in Figs. 12a through e. The correction for  $\gamma$  compensates for a large percentage of the exhaust gas temperature-induced effects. The effect is corrected more accurately at the higher nozzle pressure ratios than at the lower pressure ratios. The effectiveness of the  $\gamma$  correction also appears to be dependent on the free-stream Mach number. The  $\gamma$  correction agrees more closely at  $M_\infty = 1.2$ . At free-stream Mach numbers less than 1.2 the effect of plume temperature is slightly larger than the  $\gamma$  effects predict, while at  $M_\infty = 1.5$ , the  $\gamma$  correction is larger than the measured effects of plume temperature.

#### 4.2.2 Method of Presenting Data

Historically, nozzle/afterbody drag has been presented as a function of total nozzle pressure ratio (NPR), defined as  $p_{tj}/p_\infty$ . For a fixed area ratio nozzle this introduces into consideration a varying nozzle exit static to total pressure ratio ( $p_e/p_{tj}$ ) with  $\gamma$  which must be properly accounted for when the hot-jet effects on afterbody and boattail performance are evaluated. This variation of  $p_e/p_{tj}$  with  $\gamma$  can be eliminated from the observed effects if the nozzle/afterbody performance is presented as a function of nozzle static pressure ratio ( $p_e/p_\infty$ ). A comparison of the two methods of data presentation is shown in Figs. 13a and b for total drag coefficient,  $C_{DT}$ , at Mach 1.1. At a constant value of NPR the effect of jet temperature on drag appears to be more pronounced than it is for constant values of  $p_e/p_\infty$ . This is caused by the variation in  $p_e/p_{tj}$  with  $\gamma$  discussed above. The manner of variation of  $p_e/p_{tj}$  is shown by superimposing on Fig. 13a lines of constant  $p_e/p_\infty$ . A presentation of the exhaust jet temperature effects on nozzle/afterbody performance as a function of  $p_e/p_\infty$  (Fig. 13b) tends to collapse the data spread observed in Fig. 13a.

The method of data presentation in this report is dictated by the measured parameters available. In the Phase II investigation the total nozzle pressure ratio, NPR, was chosen because the measured chamber pressure,  $p_{tj}$ , was more reliable than was the nozzle exit static pressure measurement. For the Phase I investigation, the nozzle exit static pressure measurement was more reliable, and therefore the data were presented as a function of nozzle exit static pressure ratio. Both methods are valid and present the same information as long as the variation of  $p_e/p_\infty$  with  $\gamma$  is considered.

### 4.2.3 Reynolds Number Effect

To determine the effect of Reynolds number on boattail drag coefficient, a Reynolds number survey from  $1.0 \times 10^6$  to  $3.0 \times 10^6/\text{ft}$  was conducted at Mach numbers of 0.6 and 0.9. Drag data were obtained with cold and hot exhaust plumes. The effect of Reynolds number on boattail pressure distribution is presented in Fig. 14 at Mach 0.6 for the cold-flow data. The effect of varying Reynolds number from  $1.5 \times 10^6$  to  $3.0 \times 10^6/\text{ft}$  is imperceptible. The variation of the boattail pressure drag with Reynolds number at a constant nozzle pressure ratio and various gas temperatures is shown in Fig. 15. At both Mach 0.6 and 0.9, the effect of Reynolds number on  $C_{DBT}$  is very small over the range investigated. Figures 16a through f present the drag coefficients obtained at Mach 0.6 and 0.9 at each of the Reynolds numbers as a function of nozzle pressure ratio.

## 4.3 AIR-COOLED COMBUSTOR CONFIGURATION (PHASE I)

Phases I and II of the experimental investigation were conducted using the same external afterbody and boattail configuration (Section 2.2.2). The size of the base region was enlarged for the Phase II model because of requirements imposed by water cooling the combustor and nozzle (Fig. 5). This larger base area affected the level of the boattail drag, resulting in greater drag at a given nozzle static pressure ratio than was measured on the Phase I model (Fig. 17). A correction for base area effect for the cold exhaust plume at Mach 0.9 was made using the results obtained in Ref. 5 and shown in Fig. 17 to illustrate that the base area was responsible for the Phase II increased drag. The corrected Phase II drag coefficient was comparable to the level measured in Phase I. Sufficient base pressure data to allow correction of  $C_{DBT}$  for the remainder of the data were not available; therefore, in reviewing the results of Phase I and comparing them to Phase II, one should remember that the effect of base area was present and the absolute levels will not be comparable. The trends remain the same, however, for both phases.

### 4.3.1 Effect of Secondary Airflow on Nozzle Performance (Phase I)

Secondary airflow to provide combustor cooling during hot operation for the air-cooled combustor was introduced into the nozzle as described in Section 2.2. During cold-flow operation, the secondary airflow was maintained, and it affected the internal nozzle performance as shown in Figs. 18 and 19. The nozzle pressure ratio as a function of axial station increased with increasing secondary airflow ratio ( $W_2/W_1$ ), indicating that a larger annular portion of the available nozzle area was used by the lower-energy, secondary airflow. During an analysis of the experimental data, a disagreement between the two nozzle static pressures ( $p_{E3}$  and  $p_{E6}$ ) was observed. These pressures are located in a common axial plane 1 in. upstream of the nozzle exit and approximately 180 deg apart. Throughout the cold-exhaust plume investigation, the agreement between these pressures was affected by  $W_2/W_1$  (Fig. 19). Agreement was good for airflow ratios between four and ten percent; however, for airflow ratios less than four or greater than ten percent,  $p_{E3}$  and  $p_{E6}$  differed significantly. This disagreement has not been satisfactorily explained, but it was probably a combination of secondary airflow effects and combustor

misalignment. This internal nozzle effect was transmitted to the boattail external forces through the change in plume shape and size. Figures 20a through e are a presentation of the boattail drag coefficient (cold flow) as a function of measured nozzle static pressure ratio. Lines of constant  $W_2/W_1$  are identified. As  $W_2/W_1$  increased, boattail drag coefficient increased at a constant nozzle static pressure ratio of all Mach numbers, with the exception of Mach 0.6. This effect of secondary airflow on the boattail performance partially obscured the effects of exhaust-jet temperature.

#### 4.3.2 Effect of Hot Exhaust on Nozzle Performance (Phase I)

A presentation of the component drag coefficients as a function of nozzle static pressure ratio for each of five Mach numbers is shown in Figs. 21a through e. The drag coefficients were obtained over a wide range of exhaust gas temperatures, using the cold-exhaust plume to establish the relationship between boattail drag coefficient and pressure ratio. Because of the disagreement between the measured values of  $p_{E3}$  and  $p_{E6}$ , an average of the two pressures was used to represent the nozzle static pressure ratio. The boattail drag coefficient for the hot-exhaust plume was then determined at specific values of nozzle static pressure ratio and was compared to the cold-plume drag coefficient on the assumption that the relationship between drag coefficient and pressure ratio remains generally the same even though the exhaust gas temperature is increased. The experimental results of Phase II verified this assumption. The effects of exhaust gas temperature and increasing secondary airflow have opposing trends and tend to cloud the effect of exhaust plume temperature.

#### 4.3.3 One-To-One (1:1) Bypass Nozzle

Component drag coefficients measured on the 1:1 bypass nozzle configuration at each of the Mach numbers (0.6, 0.9, 1.1, 1.2, and 1.5) are presented in Figs. 22a through e as a function of nozzle pressure ratio. The component drag coefficients were determined at a unit Reynolds number of  $4.75 \times 10^6$  for the 1:1 bypass nozzle configuration at Mach numbers of 0.6, 0.9, and 1.1 and are compared in Figs. 22a through c with the coefficients obtained at  $2.5 \times 10^6/\text{ft}$ . Both  $C_{DBT}$  and  $C_{DAB}$  at Mach numbers 0.6 and 0.9 were higher at a Reynolds number of  $4.75 \times 10^6/\text{ft}$  than at  $2.5 \times 10^6/\text{ft}$ . The effect of Reynolds number was more pronounced on  $C_{DAB}$  than on  $C_{DBT}$ . At a free-stream Mach number of 1.1, the Reynolds number change had no effect on  $C_{DBT}$  and only a slight effect on  $C_{DAB}$ .

## SECTION V THEORETICAL ANALYSIS

### 5.1 PHYSICAL STATEMENT OF PROBLEM

The initial attempts to provide analytical prediction of the pressure distribution and drag of an isolated nozzle/afterbody configuration were carried out under the usual

assumption that the viscous-inviscid interaction could be accounted for by an iteration scheme. Such a scheme involves an iteration between the five distinct but dependent regions of the total flow field which are identified in Fig. 23. Region A represents the inviscid core of the internal nozzle and is normally supersonic. Region B, also assumed to be inviscid in nature, is the external flow around the model and can be subsonic, supersonic, or mixed flow. Regions C and D are viscous boundary layers internal to the nozzle and external to the body, respectively. At the lip of the nozzle, the viscous boundary layers merge to form a viscous mixing region, E. In general, the boundary conditions for each region are provided by the solution of the adjacent region. The inviscid regions, A and B, can be defined by specifying either a solid boundary or a pressure boundary. Region A will be defined by a solid boundary consisting of the nozzle plus the displacement thickness from Region C and by the external displacement boundary from Region E. Region B will be defined by a solid boundary consisting of the boattail plus the displacement thickness from Region D and by the internal displacement boundary from Region E. The solutions of Regions A and B will provide the pressures at the boundaries. These pressures, plus the physical nozzle and afterbody coordinates, allow a solution of the boundary layers, Regions C and D. Conditions from Regions C and D are used as starting conditions for the viscous mixing region, E. The axial pressure gradient and the location of a reference line are also required for Region E. The internal and external displacement thicknesses are computed with respect to this reference line. The boundary conditions for each region listed are summarized in Table IV.

## 5.2 NUMERICAL METHODS

The computational technique used to solve the descriptive equations for the entire flow field involves an iteration between the inviscid flow fields, A and B, and the viscous flow fields, C, D, and E. The procedure currently used for carrying out the iteration is given below:

1. The nozzle flow properties in Region A are computed using the nozzle physical coordinates and a quiescent atmosphere at the free-stream static pressure in Region B.
2. The physical coordinates of the afterbody and the inviscid boundary of Region A are used to compute the flow-field properties in Region B.
3. The inviscid flow field properties in Regions A and B are matched by recomputing the plume expansion (Region A) with the computed pressure gradient from Region B. A single iteration is usually sufficient for this matching.
4. The turbulent, viscous boundary-layer characteristics in Regions C and D are computed using the pressure distributions from Regions A and B, respectively, along with the physical coordinates of the model.



5. The flow properties in the free-shear turbulent mixing layer in Region E are computed using the inputs from the viscous boundary layers C and D and the inviscid reference line from Region A.
6. The displacements and boundary-layer characteristics from the viscous layers (Regions C, D, and E) are used to correct the model plus the plume boundary to recompute the flow fields A and B to begin the second iteration. Region A may or may not need to be recomputed since small corrections are usually produced on this flow from the viscous effects.

Computer programs have been developed for the numerical solution of the flow properties in the regions discussed (Table V). Region A can be solved using the axisymmetric Method of Characteristics Program developed by Lockheed (Ref. 6). This program is used for supersonic flow and is also employed to solve Region B when the external flow field is supersonic. If Region B is subsonic, a program developed by Pratt & Whitney (Ref. 7) is used for its solution. This solution is carried out using a numerical solution of the nonlinear, transonic flow equation. The equation is written in the form of a Poisson equation with the nonlinear terms on the left-hand side. The solution is then performed by the method of successive substitutions starting with the solution of the Laplace equation. The treatment of imbedded shocks limits the practical utility of this program to afterbody flows which are subsonic everywhere. The turbulent boundary-layer calculations, over either the external afterbody/boattail or the internal nozzle (Regions C and D), are made with the implicit finite-difference scheme of Patankar (Ref. 8). The viscous mixing region E can also be solved with the Patankar program, employing a second option using boundary-layer assumptions.

The scope of this report does not allow a detailed description of the calculation techniques used in these various computer programs. However, the reader is directed to the cited references for a more complete description.

The computational technique outlined above does not include the effect of entrainment on the boattail pressure distribution. This effect is necessary for a complete analytical solution to the problem, and efforts to incorporate the entrainment effect on the boattail pressures in the computational technique are being carried out at AEDC. The computational technique is also inadequate when nearly normal shockwaves are located on the boattail of the afterbody.

### 5.3 COMPARISON OF THEORY AND EXPERIMENTAL RESULTS

The methods described were used to compute the pressure fields over the aft portion of the isolated nozzle model and, finally, the drag over the afterbody and boattail. These efforts are reasonably successful at the subsonic Mach numbers for the air-cooled model, which has a small base area. During the course of making the drag calculations, it was found that certain approximations could be made to shorten the iteration process when the external stream was subsonic. First, because of the low nozzle pressure ratios used

during subsonic flight (see Fig. 6), matching the nozzle exit static pressure to free-stream static pressure ratio is the primary parameter required to match the inviscid plume shapes. Hence, changing the plume total temperature from 520 to 2700°R had only a negligible effect on the inviscid plume boundaries, which are shown in Figs. 24 and 25 for  $M_\infty = 0.6$  and 0.9, respectively. Secondly, mixing was primarily from the high-energy plume into the low-energy external flow, and the internal displacement boundary did not vary significantly with respect to temperature. These two effects combine to allow the external flow and boundary-layer-mixing iteration to be carried out without affecting the basic plume boundary calculation.

Although the inviscid pressure distribution could be calculated initially without any boundary-layer displacement corrections to the afterbody/boattail contour, an attempt was made to shorten the iteration cycle by making the displacement corrections from boundary-layer calculations carried out using the experimental pressure distribution. The resulting displacement thickness for  $M_\infty = 0.6$  is shown as the dashed line in Fig. 24. The external displacement boundaries for four plume temperatures are also shown. Initial conditions for the viscous mixing region were matched to the internal and external boundary-layer characteristics at the nozzle exit plane. Using these results as an input boundary for the inviscid external flow solution, a much steeper pressure gradient was computed on the boattail than was measured. When this predicted pressure was imposed on the external boundary layer, separation was predicted at the point noted in Fig. 24.

As can be seen from this result, the attempt to shorten the viscous-inviscid iteration cycle by using the boundary-layer characteristics from the experimental pressure was not successful since the second iteration indicated boundary-layer separation not predicted from the experimental pressure distribution. The calculation procedure outlined in Section 5.2 does not have any method available to predict displacement thicknesses in the separated region. This requires a detailed prediction of the reverse flow profiles and the extent of the separation (or abnormally thick boundary layer) region. Recently there has come to the attention of the authors a calculation procedure developed for the separated turbulent boundary layer imbedded in the transonic flow over a bump on a wind tunnel wall (Ref. 9). It is possible that such a procedure can be incorporated into the method outlined previously, and an attempt will be made to do so. Since such a calculation procedure was not available at the time of writing, it was necessary to smoothly fair in an effective displacement boundary from the point of separation to the effective plume displacement boundary in order to predict the experimental pressure distribution from the corrected body shape. The fairing was arbitrary and was carried out in a manner so that the experimental data agreed with the analytical results. Efforts are still under way to develop reasonable criteria to use in making the correction to the body and plume displacement. Two points appear evident when the displacement corrections are made: (1) the downstream variation of the initial plume displacement effects remain very small and can be predicted during the first cycle of the viscous-inviscid iteration, and (2) the changes in the pressure distribution between iterations cause very little change in the boundary-layer characteristics ahead of the point where separation was initially predicted. This small change was probably caused by (1) the weak viscous-inviscid iteration present on the particular

afterbody used and (2) the fact that the analysis was done at subsonic Mach numbers where shock/boundary-layer iterations are not present. The strong interaction region from the apparent separation point to the apparent point of attachment to the exhaust plume does have to be iterated on to predict the correct experimental afterbody pressure distribution. The final fairings for the displacement boundaries used in the external flow calculations are shown in Fig. 24 for  $M_\infty = 0.6$ . Similar results are shown in Fig. 25 for  $M_\infty = 0.9$ . Preliminary calculations indicated that a region of locally supersonic flow existed over the shoulder of the afterbody at  $M_\infty = 0.9$ . The afterbody shape was modified somewhat to eliminate this locally supersonic region so that the external flow could be treated as wholly subsonic. It was realized that the pressures would not be well predicted in the modified region; however, it was felt that these effects of modification would be sufficiently localized so that the pressure near the end of the boattail would be adequately predicted.

Using the boundaries shown in Figs. 24 and 25, external flow solutions were carried out for  $M_\infty = 0.6$  and 0.9. Pressure distributions over the body are shown in Fig. 26 at  $M_\infty = 0.6$  for different nozzle plume temperatures. The numerical method predicts the general data trend over the body. It is noted that the method predicts boattail pressures that increase at an increasing rate with temperature. The data generally support this trend, although the agreement is not perfect.

Pressure distributions over the body are shown in Fig. 27 for  $M_\infty = 0.9$ . Similar theoretical trends with temperature and agreement with the data over the boattail were noted for  $M_\infty = 0.6$ . The pressure over the shoulder of the afterbody is not well predicted in the region from 10 to 16 in. upstream of the nozzle exit, since the body was modified in this area for the analytical model.

The pressure and skin friction over the boattail shown in Figs. 26 and 27 were integrated to obtain drag. The results of these integrations are presented in Fig. 28 as boattail drag coefficient versus exhaust gas temperature and are compared with the experimental data obtained with both the air-cooled and the water-cooled combustors. The slope of the curve of drag coefficient as a function of exhaust gas temperature for the two experimental configurations agrees closely, while the slope obtained from theory is steeper. The absolute levels of drag coefficient predicted by theory and obtained experimentally with the air-cooled combustor configuration are in fair agreement at an exhaust gas temperature of 530°R. The absolute level of the drag coefficient obtained with the water-cooled combustor at 530°R exhaust gas temperature was higher than those obtained from the air-cooled combustor and theoretical predictions. This difference is attributed to the large base area of the water-cooled combustor discussed previously.

A plot of the pressure data shown in Fig. 29 at  $M_\infty = 1.2$  is typical of the data when the external stream is supersonic. A Method of Characteristics calculation is shown for comparison in Fig. 29. The data and the theoretical prediction agree quite well over the shoulder of the afterbody, but not over the boattail. First, there was apparently a disturbance at the metric break between the afterbody and the boattail (6 in. upstream

of the nozzle exit) that was not predicted by the MOC. Second, a shock was located approximately 4 in. upstream of the nozzle exit. There is no method currently available to predict either the location or the strength of this shock. To assume that the flow separates immediately behind the shock and reattaches near the maximum diameter of the plume would require a turning angle which yields a pressure rise across the shock of the same order as was measured. However, this type of analysis is not sufficiently accurate to evaluate the drag over the afterbody.

## SECTION VI CONCLUSIONS

The effect of exhaust plume temperature on afterbody and boattail drag was investigated for two combustor and three internal nozzle configurations installed in an isolated pod. The investigation provided both experimental and analytical data for the internal and external flow fields. The significant results and conclusions are summarized below. (It should be emphasized that the following results and conclusions were obtained for a particular isolated external boattail configuration and may not necessarily be the same for other configurations.)

1. For the water-cooled combustor configuration with a turbojet military nozzle, the maximum change in total drag coefficient at a Reynolds number of  $2.5 \times 10^6/\text{ft}$  was 160 boattail drag counts at Mach 1.1 and 90 counts at Mach 0.6 over an exhaust gas temperature range from  $530^\circ$  to approximately  $2700^\circ\text{R}$ . For each of the Mach numbers investigated, drag coefficient decreased monotonically with increasing exhaust gas temperature at a constant nozzle pressure ratio.
2. From the hot-flow data obtained, it appears that correcting the cold-flow exhaust pressure ratio for changes in specific heat ratio will compensate for a large percentage of the effect of a hot exhaust on afterbody performance. The apparent displacement and entrainment effects produced by differences in viscous mixing between hot and cold exhausts also have to be considered.
3. Exhaust plume temperature affected the afterbody drag coefficient at Mach 0.6 and 0.9. The effect was negligible at Mach 1.1, 1.2, and 1.5.
4. A Reynolds number survey from  $1.0 \times 10^6$  to  $3.0 \times 10^6/\text{ft}$  was conducted at Mach 0.6 and 0.9 for the water-cooled combustor configuration. The effect of Reynolds number variation on total boattail drag coefficient was less than 30 drag counts over the range of the investigation for both Mach numbers 0.6 and 0.9.

5. The boattail drag coefficient obtained with the air-cooled combustor, military nozzle configuration during the cold-exhaust plume investigation showed a strong influence of secondary airflow. When presented as a function of average nozzle static pressure ratio, the boattail drag increased with an increase in percentage of secondary airflow.
6. The boattail drag coefficient obtained with the air-cooled combustor/military nozzle configuration behaved in the same manner as that obtained with the water-cooled configuration. The maximum change in boattail drag coefficient at a Reynolds number of  $2.5 \times 10^6/\text{ft}$  was 182 drag counts at Mach 0.9 and 50 drag counts at Mach 1.5 over an exhaust gas temperature range from  $530^\circ$  to approximately  $2900^\circ\text{R}$ .
7. The boattail drag coefficient decreased with increasing exhaust jet temperature at all of the free-stream Mach numbers of the investigation for the 1:1 bypass turbofan nozzle configuration. The temperature effect agreed in general with the results obtained with the water-cooled/military nozzle configuration.
8. Analytical techniques to calculate the effect of temperature on boattail drag coefficient were begun with emphasis placed on subsonic Mach numbers 0.6 and 0.9. The developed method agrees well with the experimental results obtained from the air-cooled combustor. This method does not account, however, for the effect of entrainment and base area on boattail pressure distribution.

## REFERENCES

1. "Experimental and Analytical Determination of Integrated Airframe-Nozzle Performance." AFFDL-TR-72-101, Vol. 1, October 1972.
2. Faget, M. A. and Dettwyler, H. R. "Initial Flight Investigation of a Twin-Engine Supersonic Ram Jet." NACA RM L50H10, September 1950.
3. Sivells, J. C. and Payne, R. G. "A Method of Calculating Turbulent Boundary-Layer Growth at Hypersonic Mach Numbers." AEDC-TR-59-3 (AD208774), February 1959.
4. Bergman, D. "Effects of Engine Exhaust Flow on Boattail Drag." Journal of Aircraft, Vol. 8, No. 6, June 1971, pp. 434-439.

5. Aulehla, F. and Latter, K. "Nozzle/Airframe Interference and Integration." AGARD-LS-53, May 1972.
6. Prozan, R. J. "Development of a Method of Characteristics Solution for Supersonic Flow of an Ideal, Frozen, or Equilibrium Reacting Gas Mixture." Technical Report LMSC/HREC A782535, April 1966.
7. "Users Manual for the External Drag and Internal Nozzle Performance Deck (Deck X1) Transonic/External Flow Analysis (Applicable to Deck V)." Pratt and Whitney Aircraft, PWA-3465, Supplement F, Part II, September 1968.
8. Patankar, S. V. "Heat and Mass Transfer in Turbulent Boundary Layers." Ph.D. Thesis, Imperial College of Science and Technology, London, England, May 1967.
9. Kuhn, G. D. and Nielsen, J. N. "Prediction of Turbulent Separated Boundary Layers." AIAA Paper No. 73-663, presented at the AIAA 6th Fluid and Plasma Dynamics Conference, Palm Springs, California, July 1973.

**APPENDIXES**

**I. ILLUSTRATIONS**

**II. TABLES**

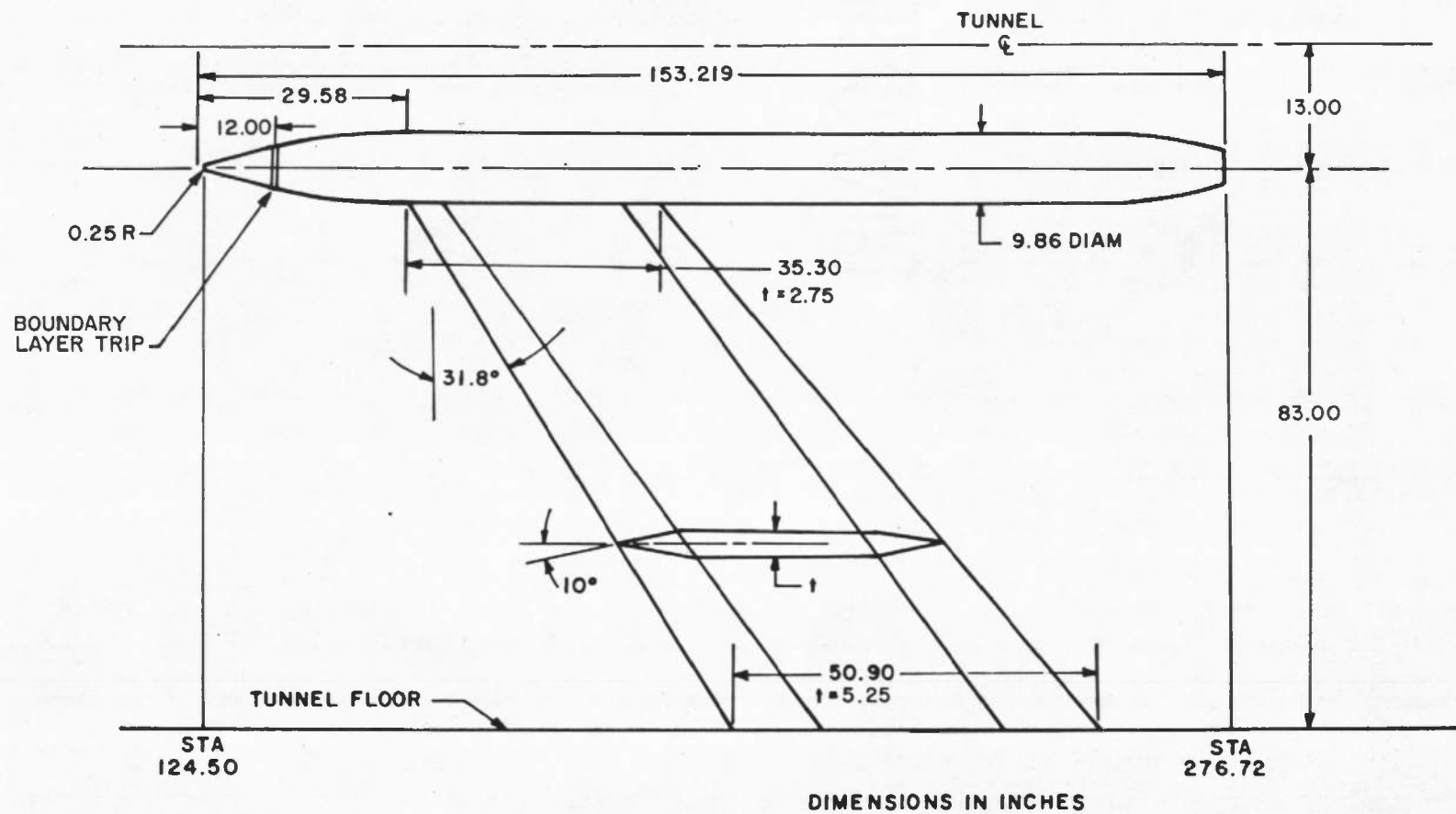
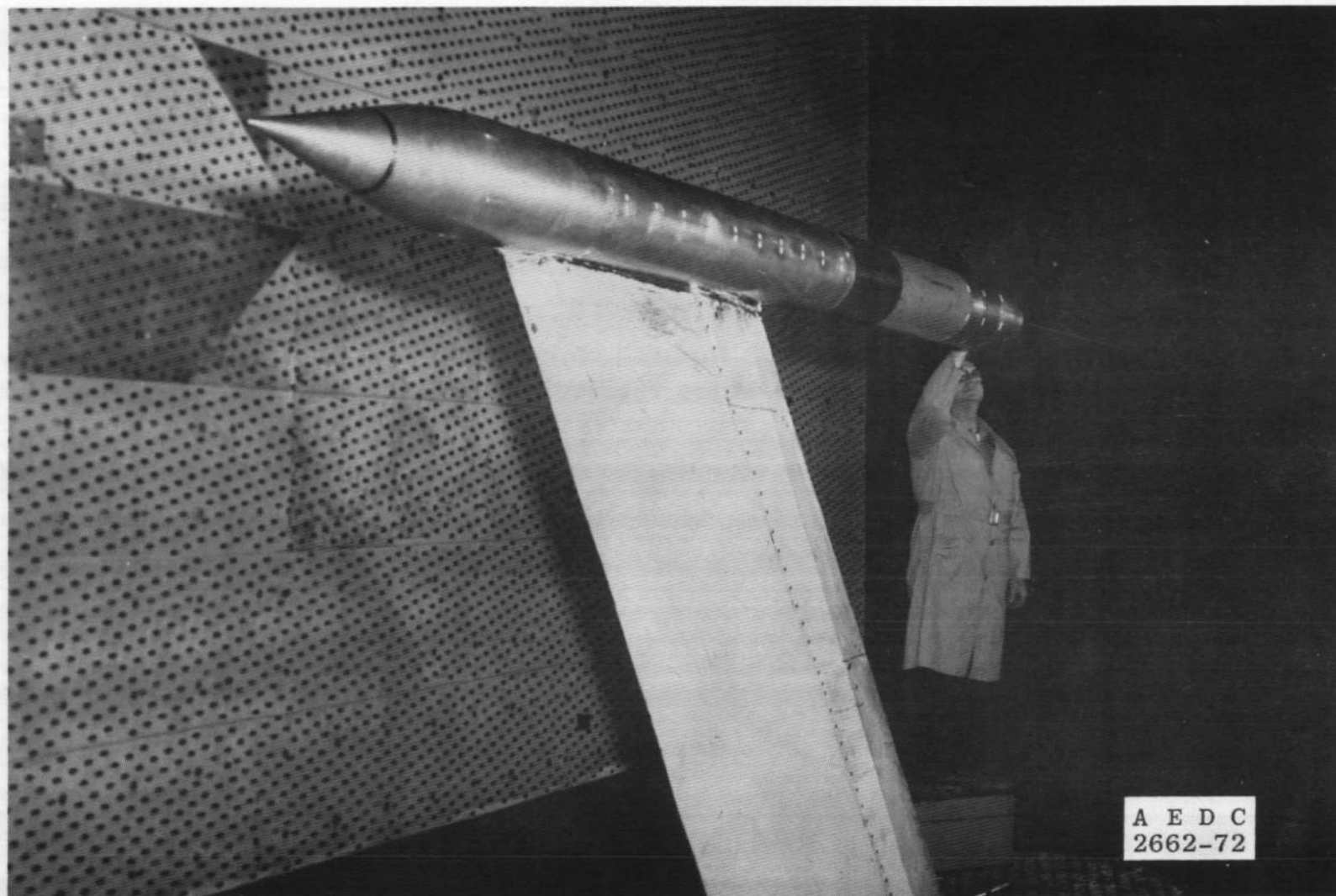
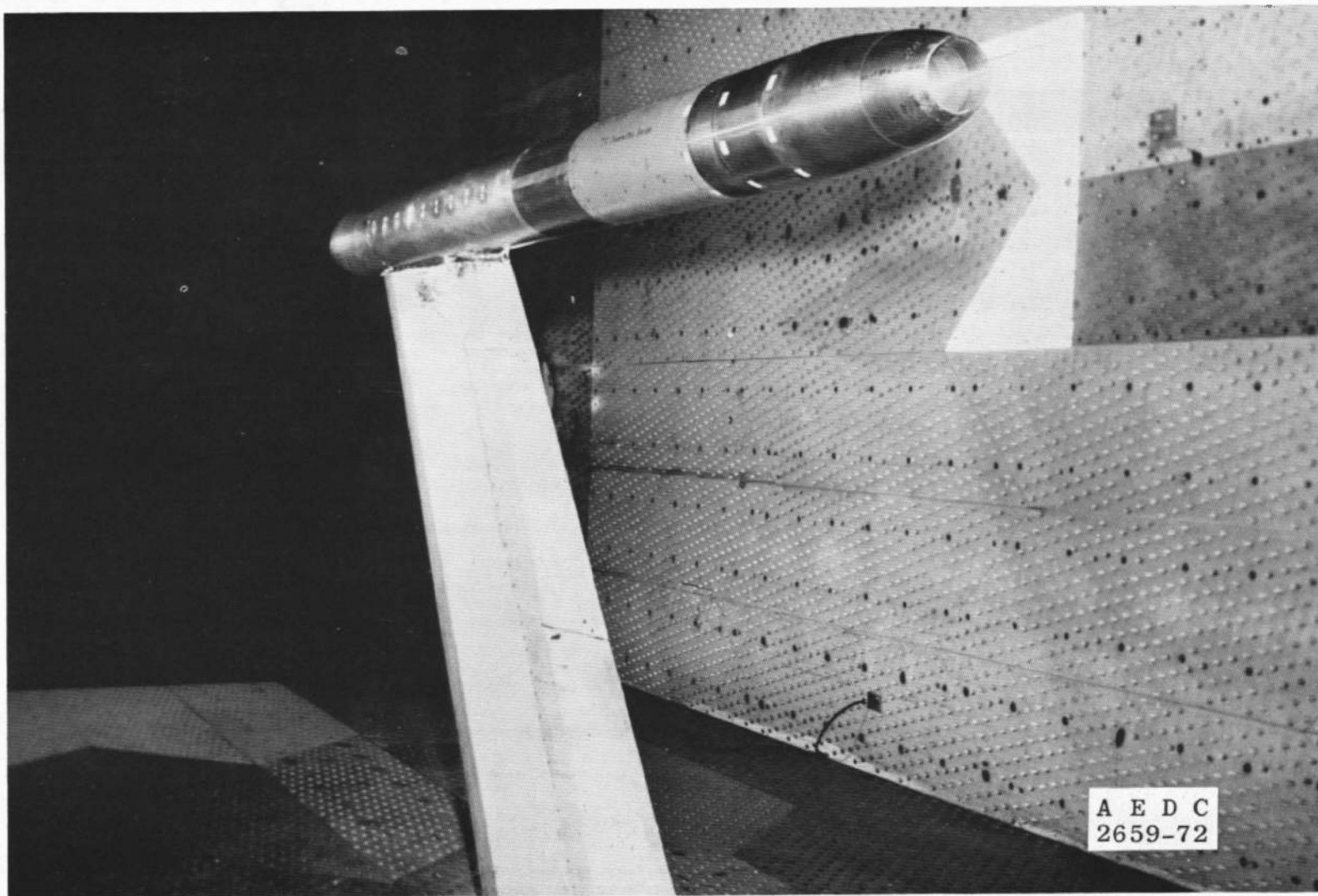


Fig. 1 Basic Model Dimensions and Location in Test Section

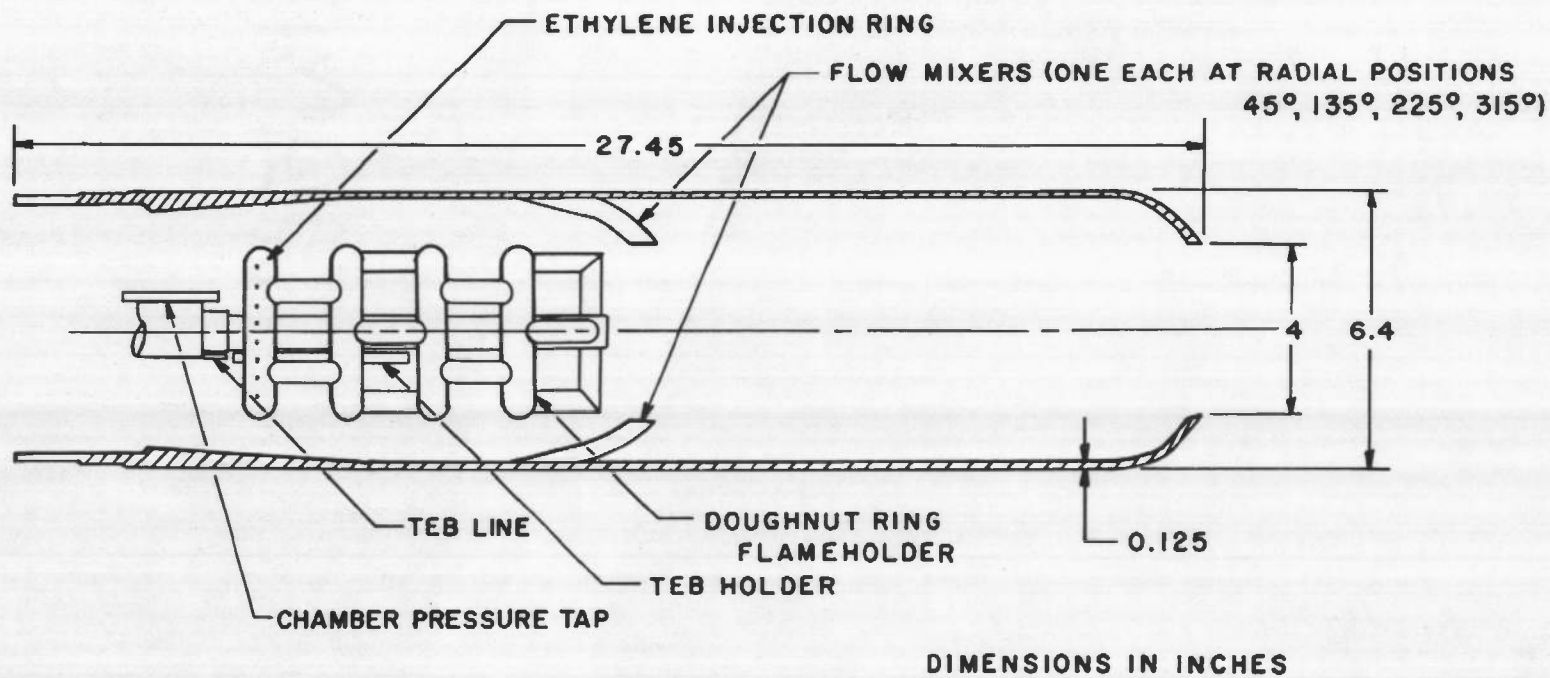




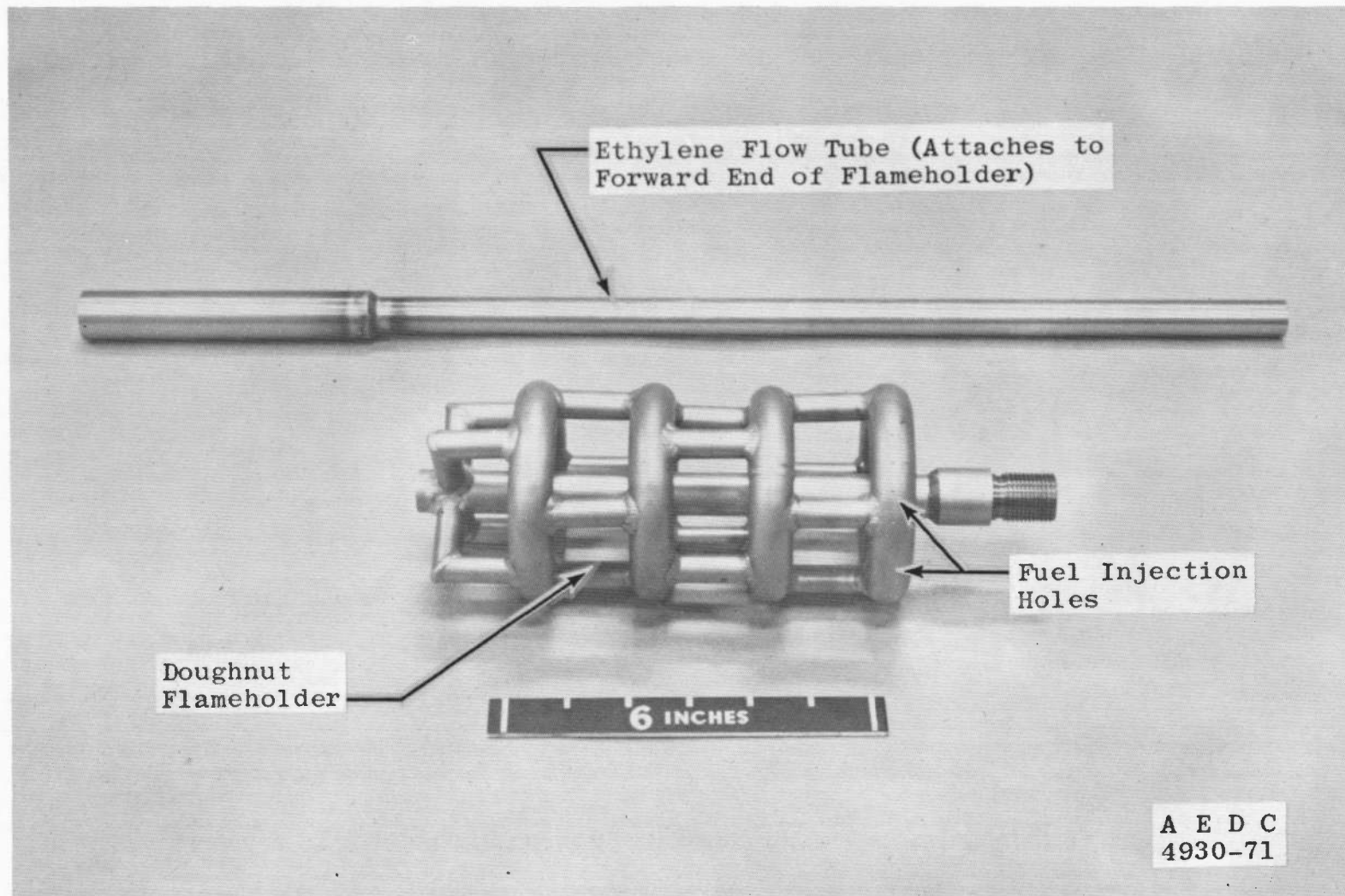
a. View Looking Downstream  
Fig. 2 Model Installation Photographs



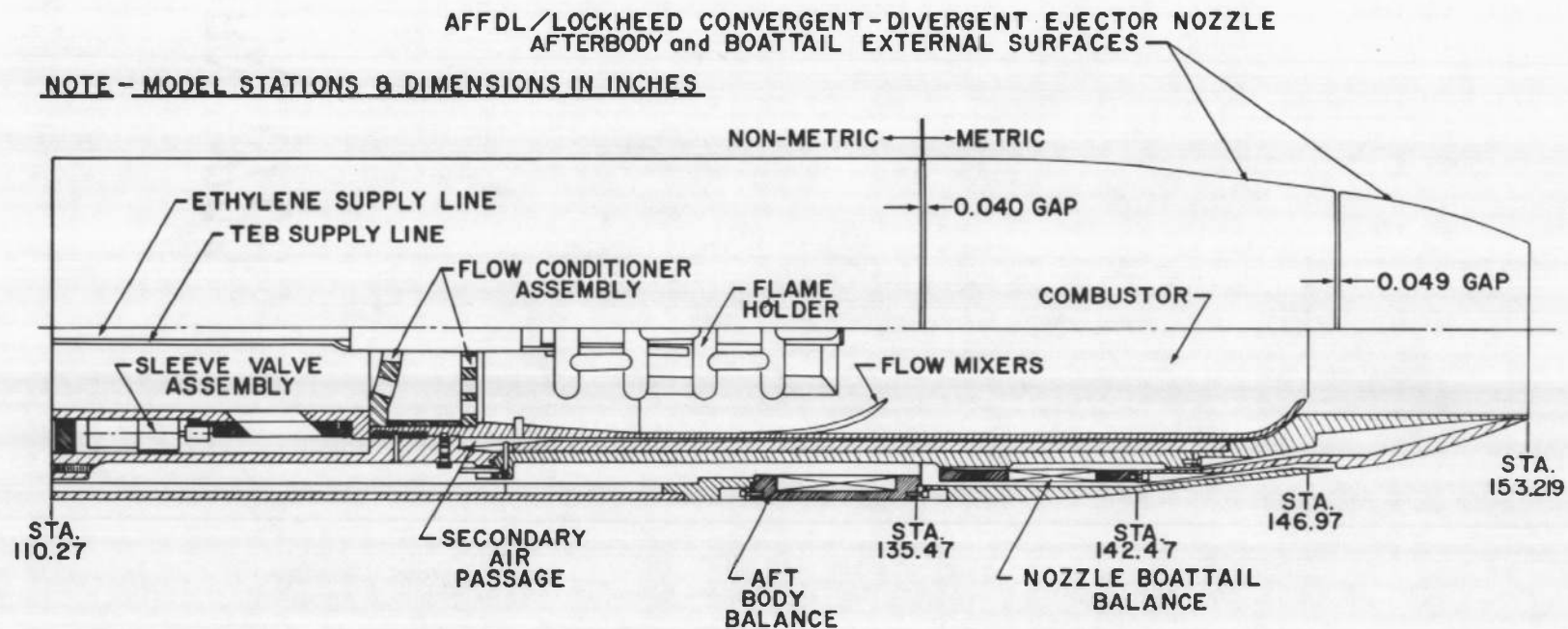
b. View Looking Upstream  
Fig. 2 Concluded



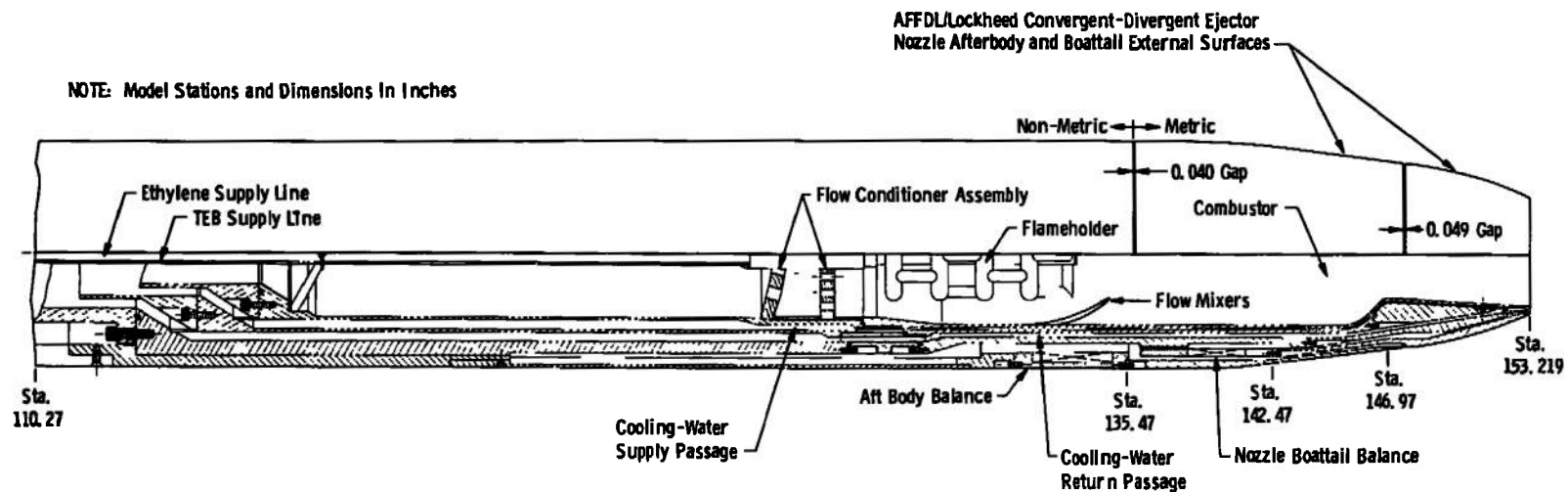
a. Sketch of Combustor  
Fig. 3 Combustor Details



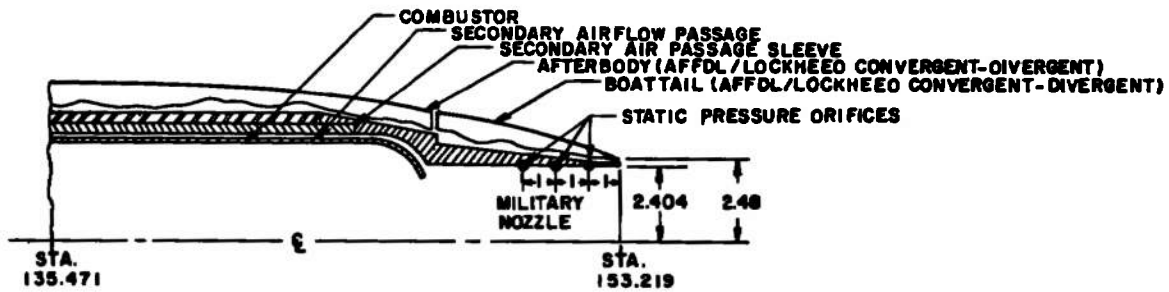
b. Flameholder  
Fig. 3 Concluded



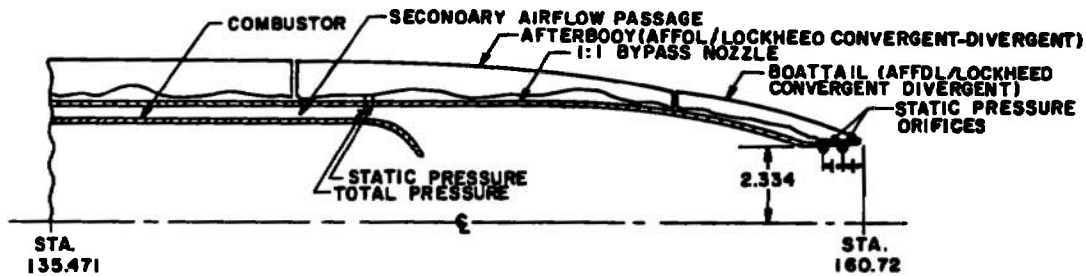
a. Air-Cooled Combustor  
Fig. 4 Model Internal Details



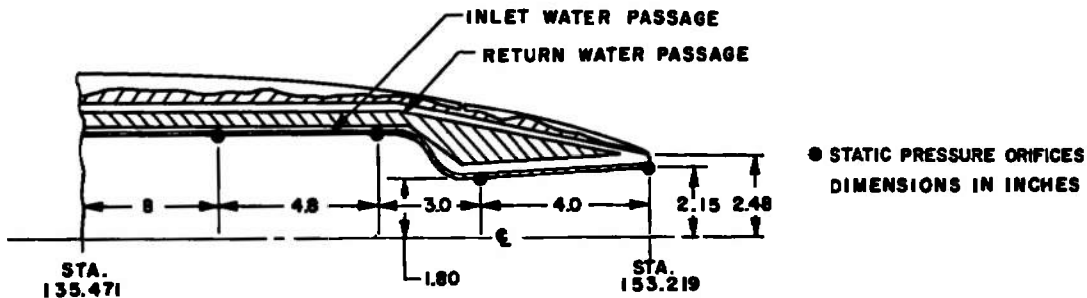
b. Water-Cooled Combustor  
Fig. 4 Concluded



a. Air-Cooled Combustor, Turbojet Military Nozzle



b. Air-Cooled Combustor, Turbofan Military Nozzle (1:1 Bypass Ratio)



c. Water-Cooled Combustor, Turbojet Military Nozzle

Fig. 5 Schematic of Nozzle Configurations and Nozzle Pressure Instrumentation



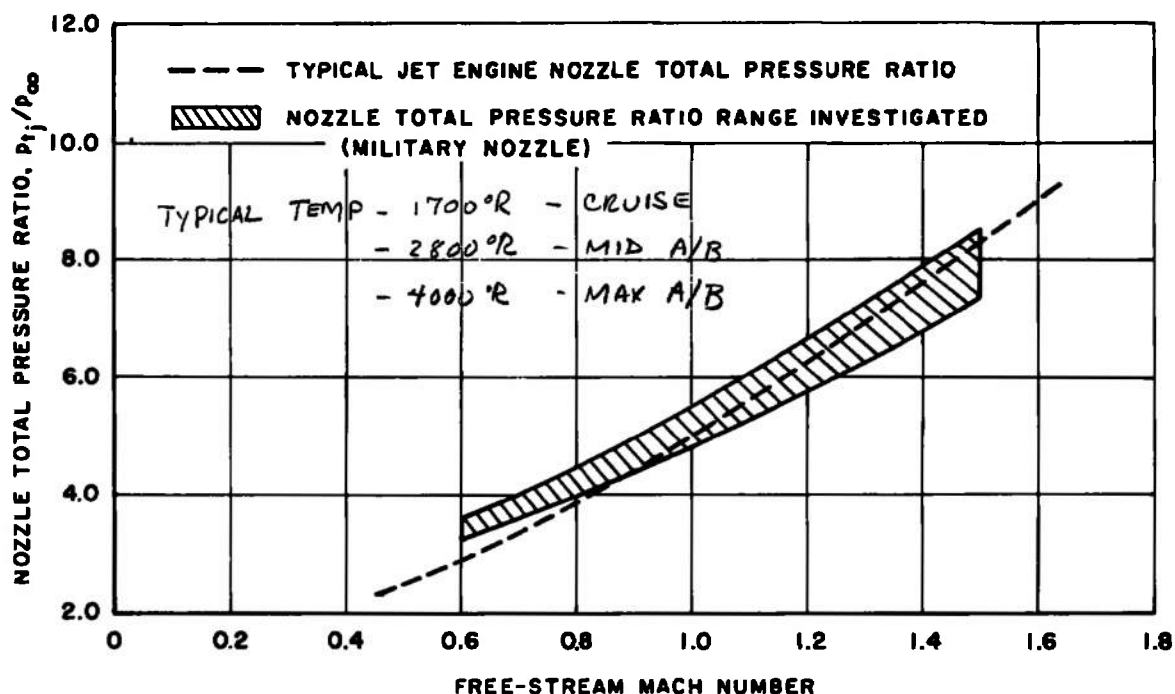
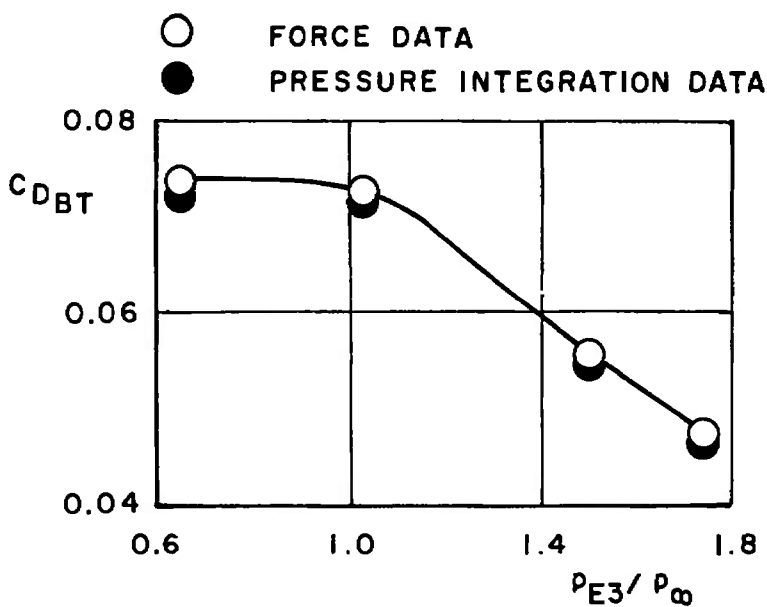
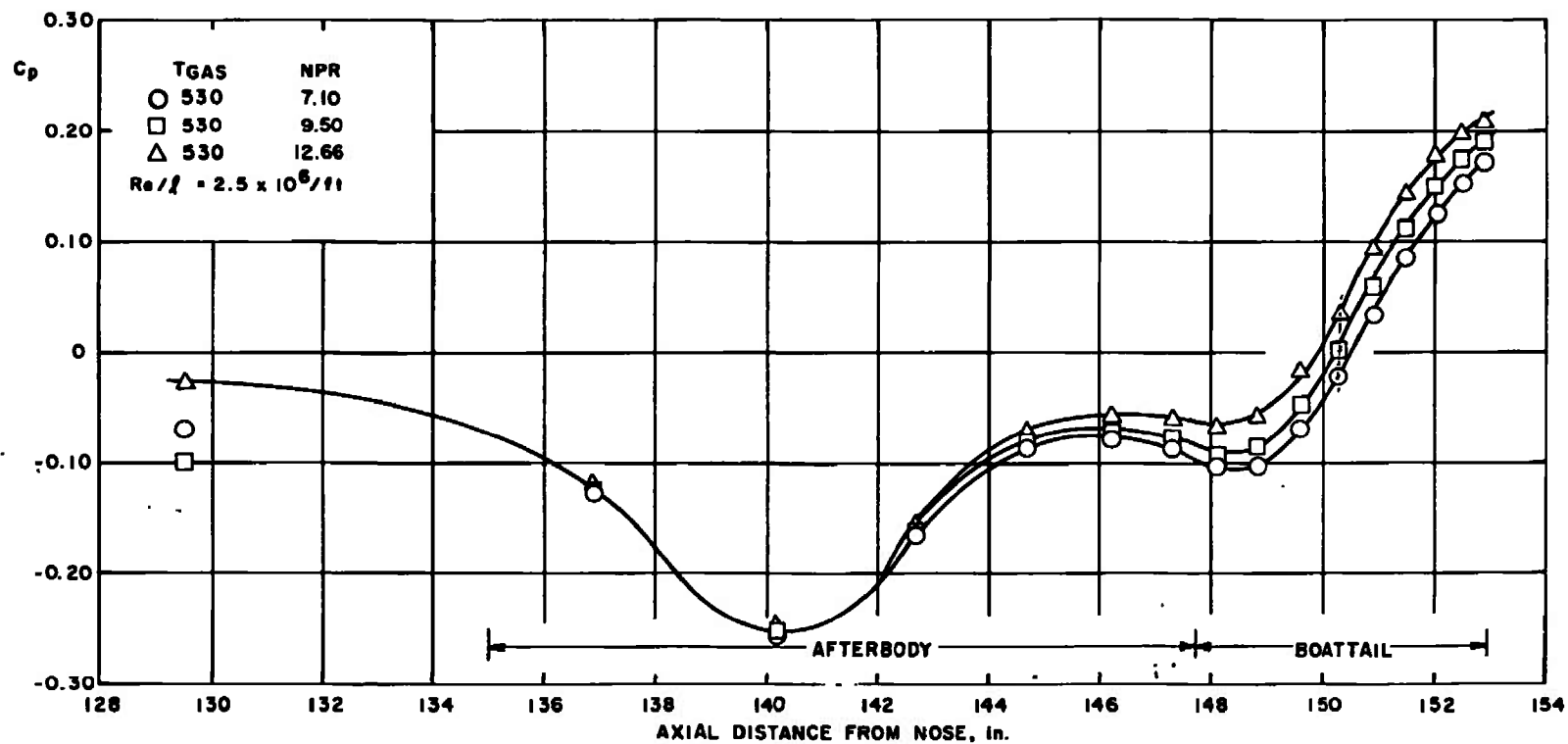


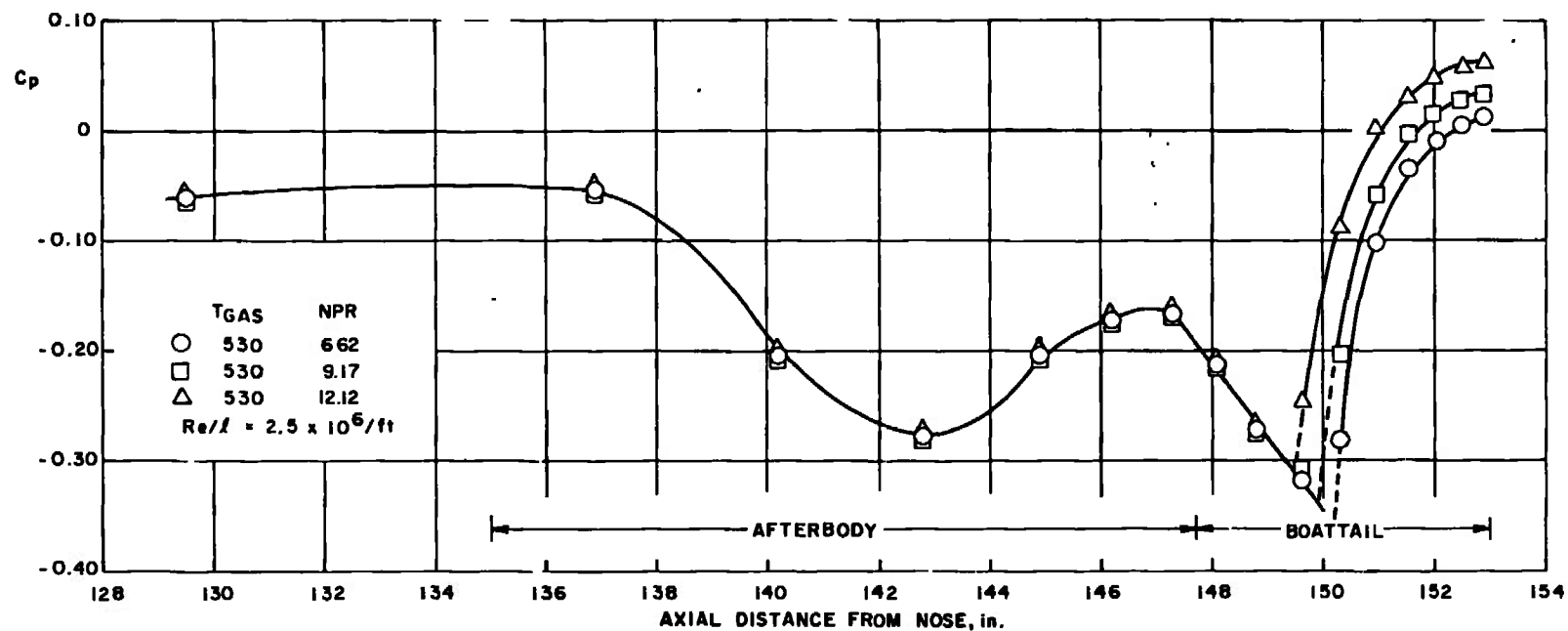
Fig. 6 Range of Nozzle Total Pressure Ratio

Fig. 7 Comparison of Pressure Integration Boattail Drag Coefficient with Force Balance Boattail Drag Coefficient at  $M_{\infty} = 1.2$  and  $Re = 2.5 \times 10^6/ft$

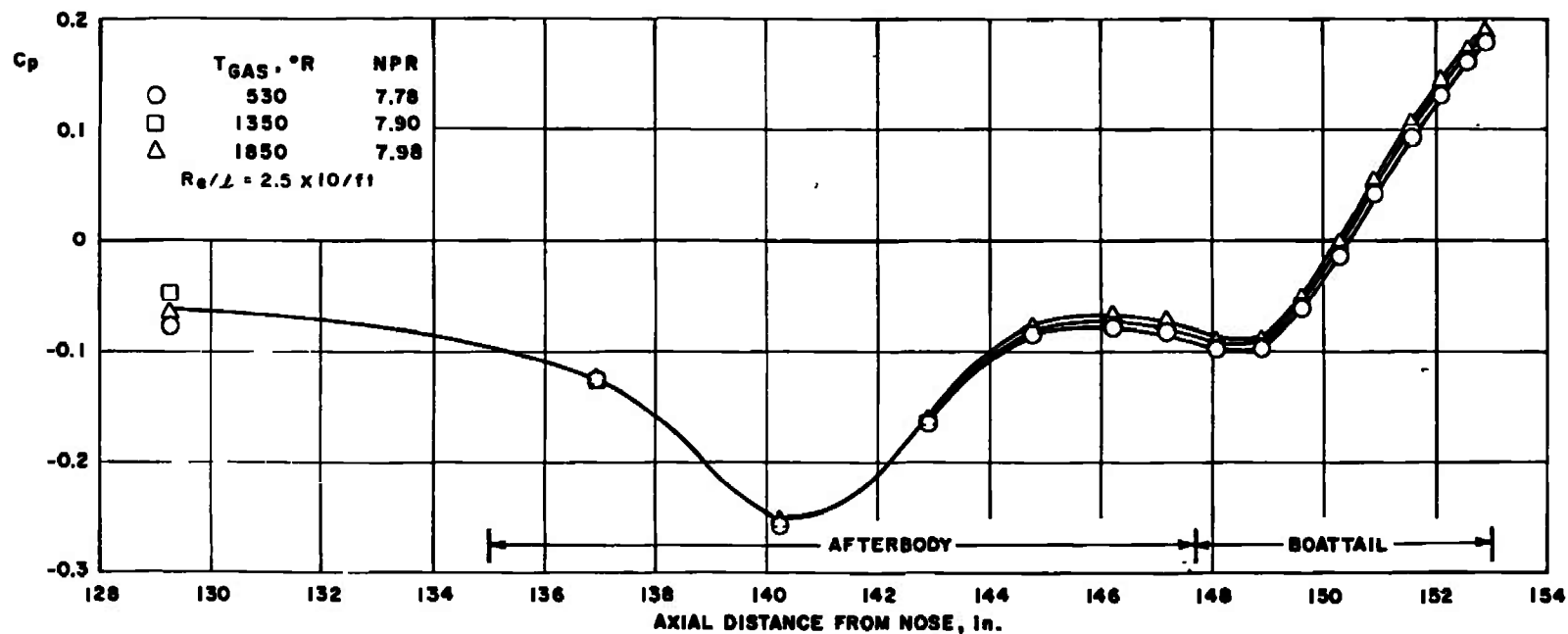




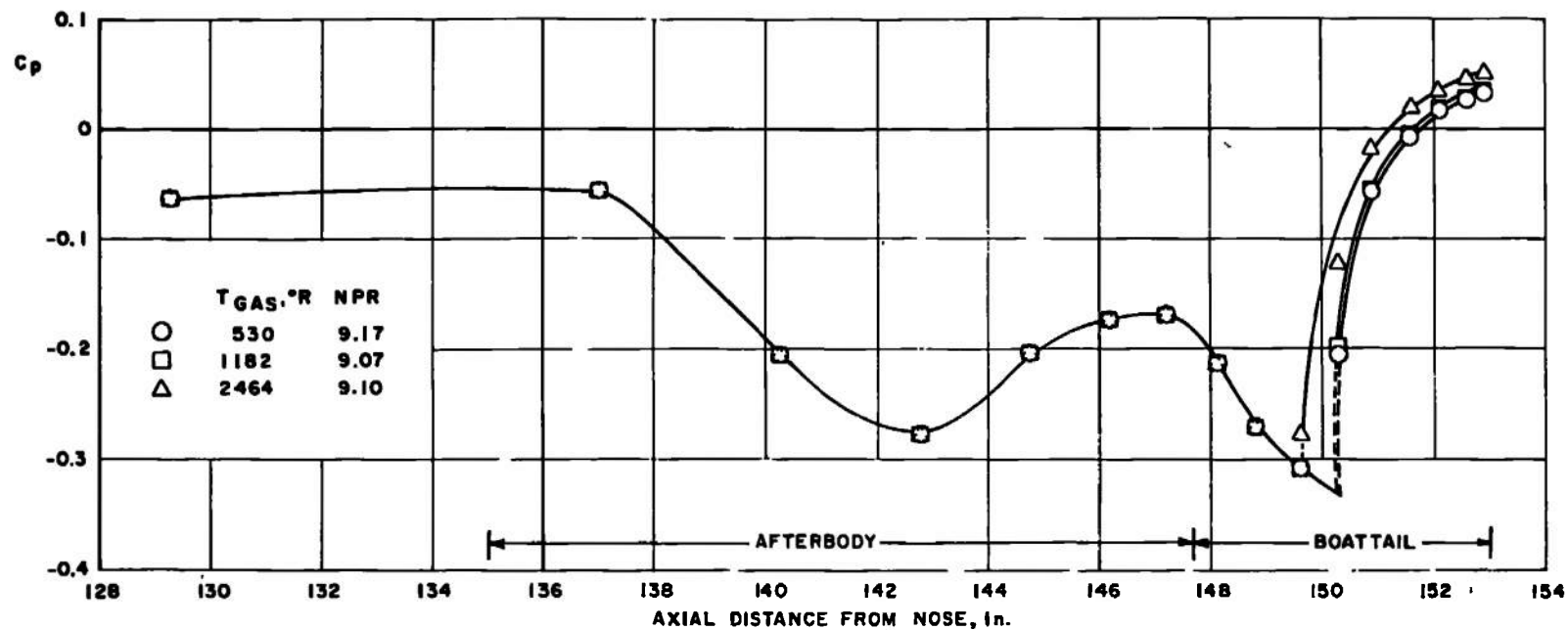
a. Effect of Static Pressure Ratio at  $M_\infty = 0.9$   
 Fig. 8 Typical Boattail Static Pressure Distributions



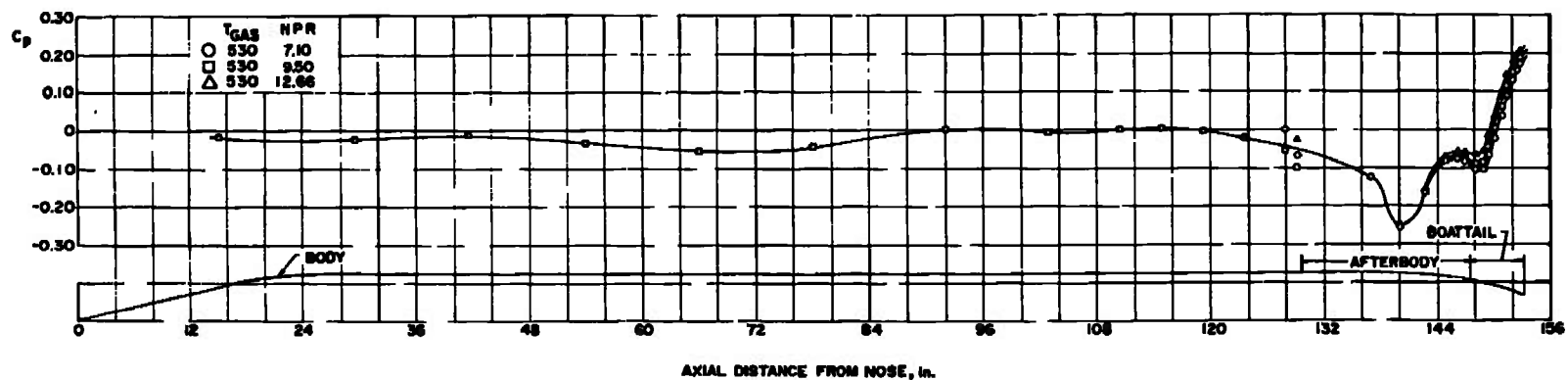
b. Effect of Static Pressure Ratio at  $M_\infty = 1.1$   
Fig. 8 Continued



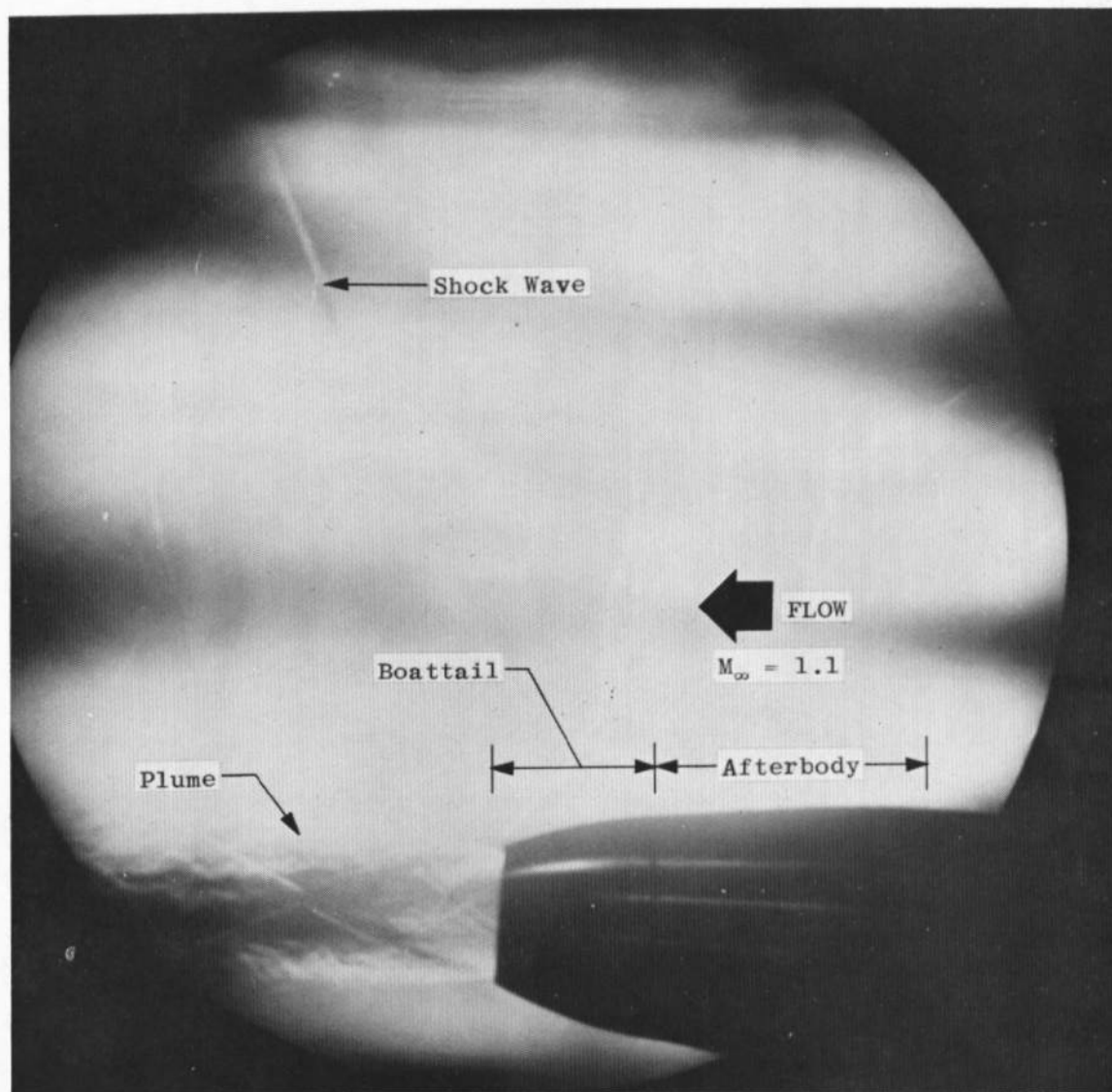
c. Effect of Exhaust Plume Temperature at  $M_\infty = 0.9$   
Fig. 8 Continued



d. Effect of Exhaust Plume Temperature at  $M_\infty = 1.1$   
Fig. 8 Continued

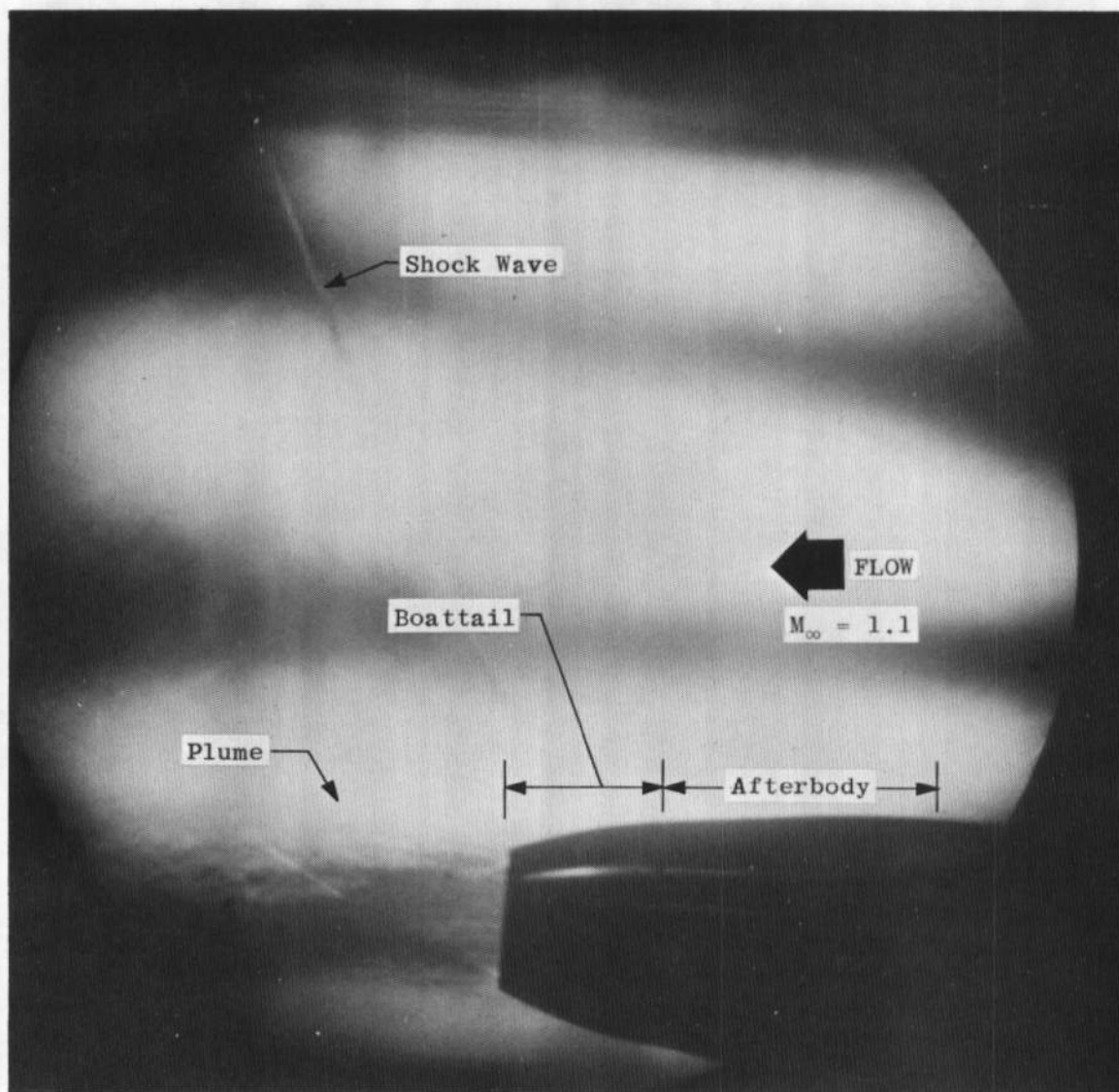


e. Pressure Distribution over Model at  $M_\infty = 0.9$   
Fig. 8 Concluded

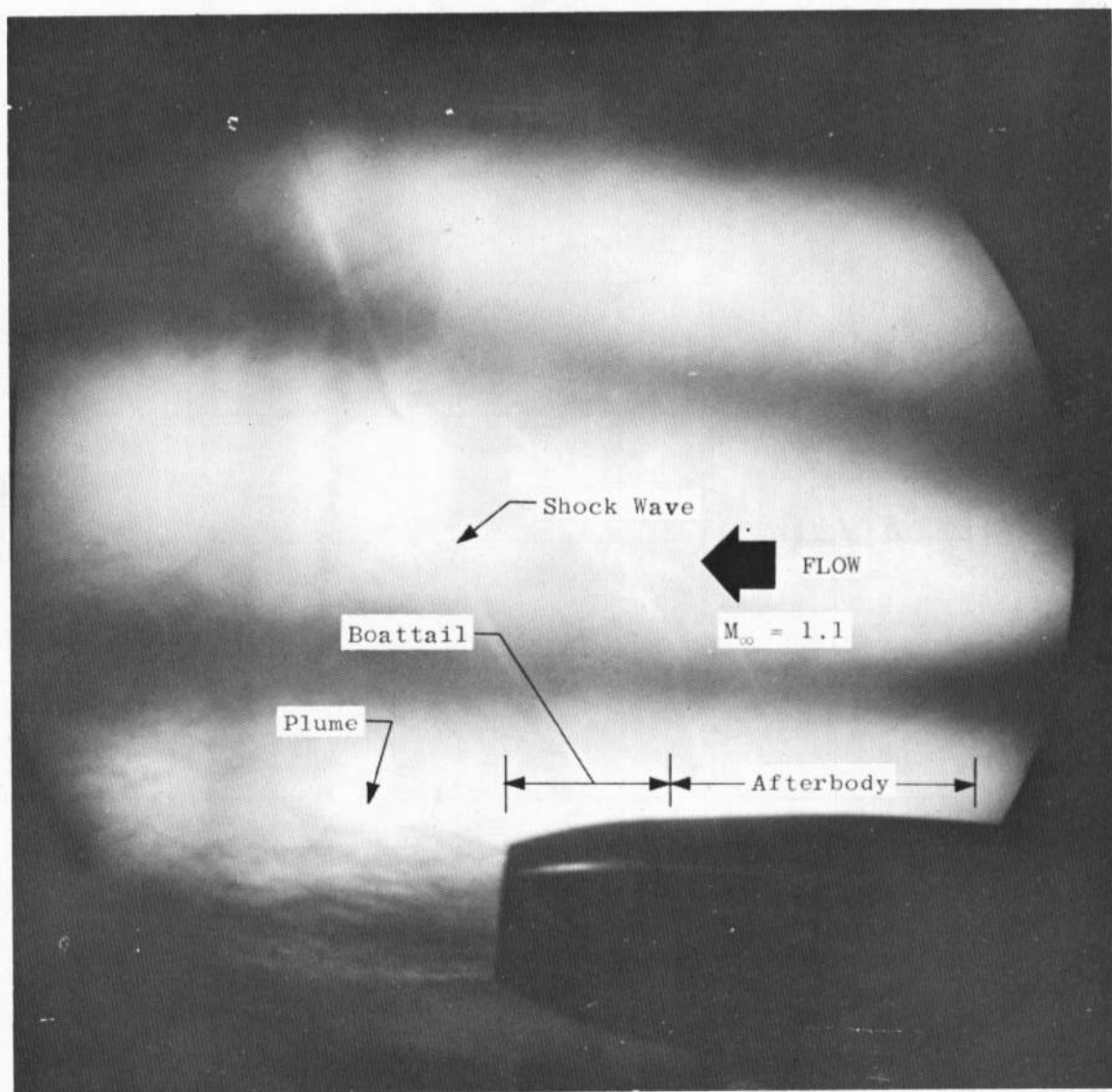


a.  $T_{GAS} = 530^\circ R$ ,  $NPR = 9.17$

Fig. 9 Typical Schlieren Photographs at  $M_\infty = 1.1$  and  $Re = 2.5 \times 10^6/ft$

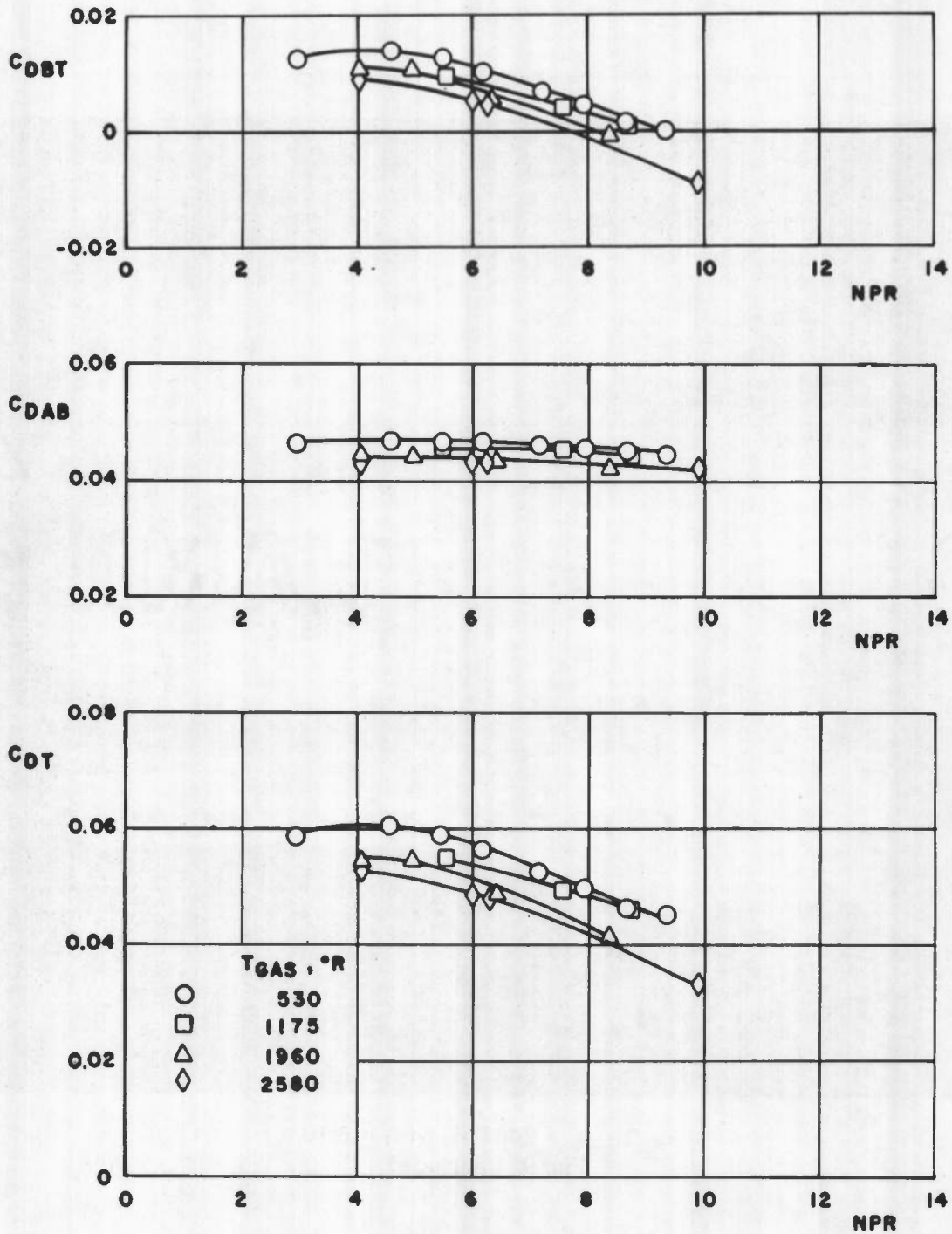


b.  $T_{GAS} = 1182^{\circ}R$ ,  $NPR = 9.07$   
Fig. 9 Continued



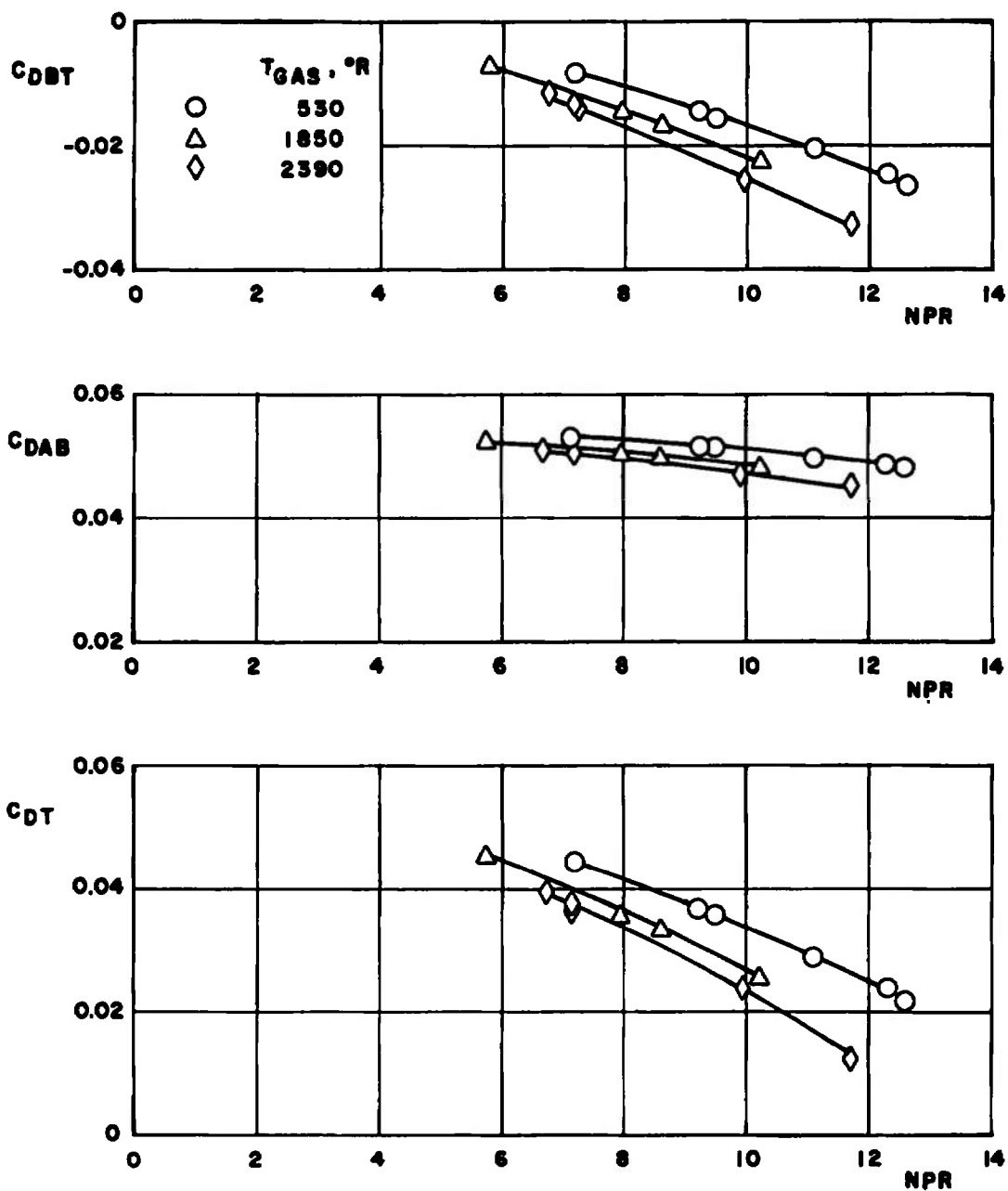
c.  $T_{GAS} = 2464^{\circ}R$ ,  $NPR = 9.10$   
Fig. 9 Concluded



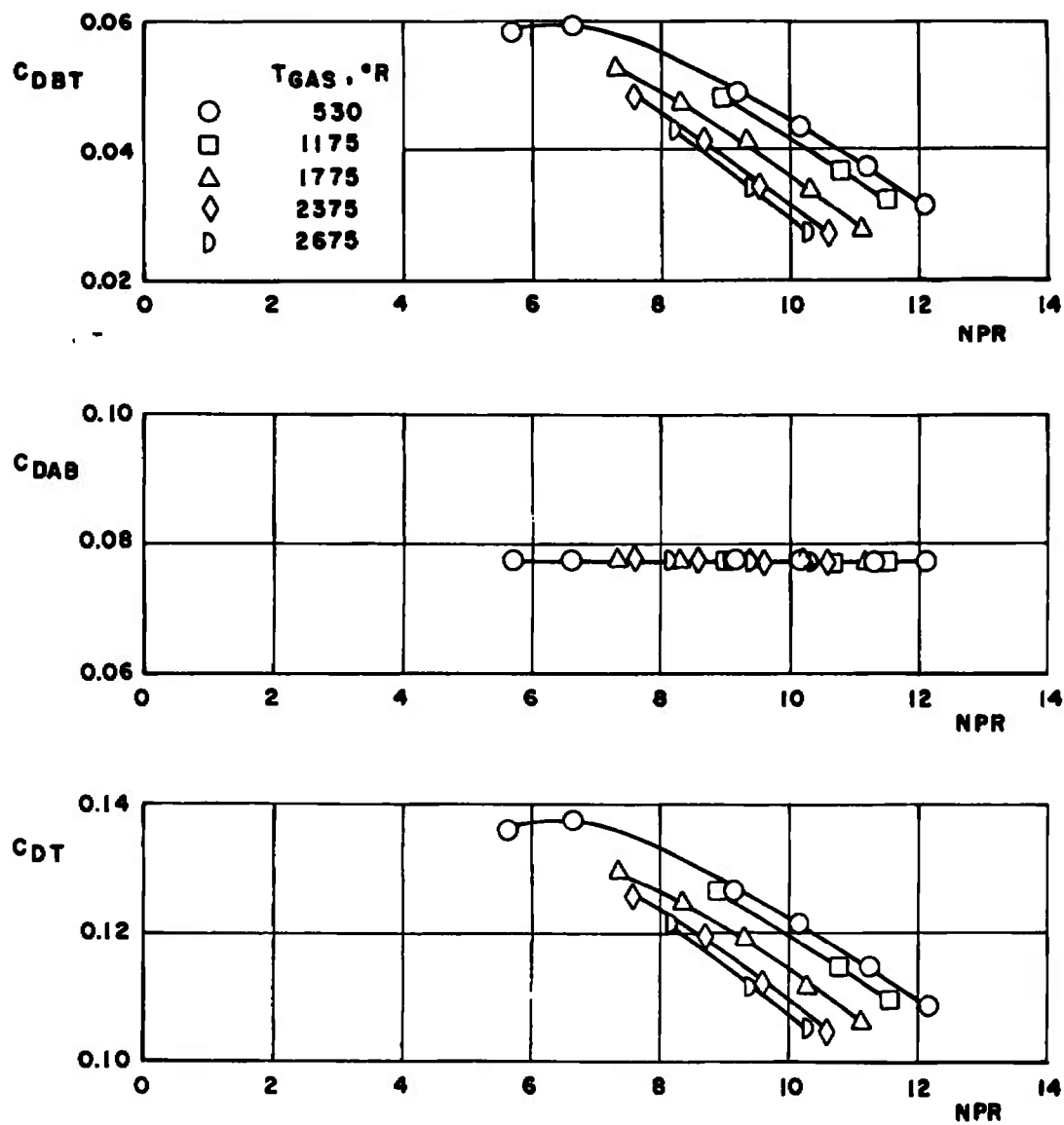


a.  $M_{\infty} = 0.6$

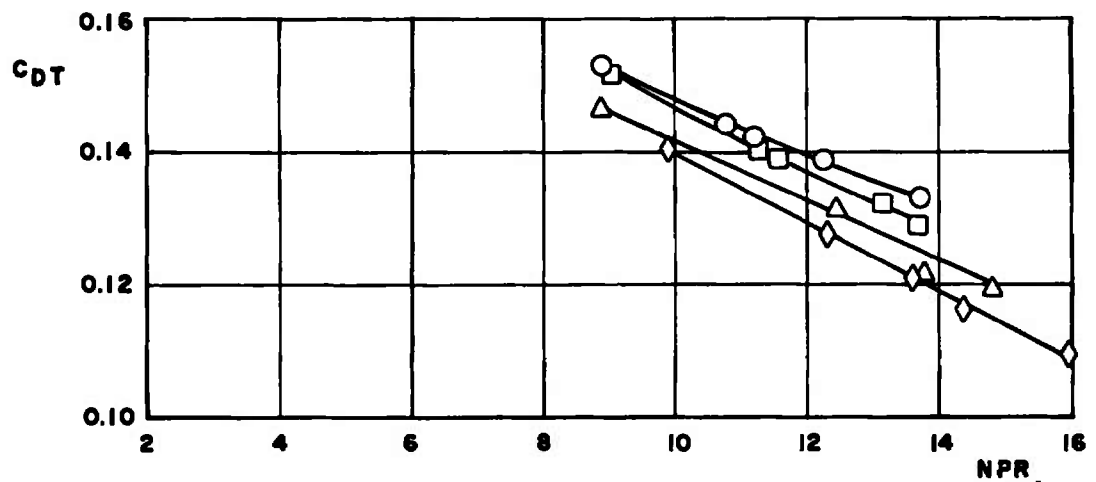
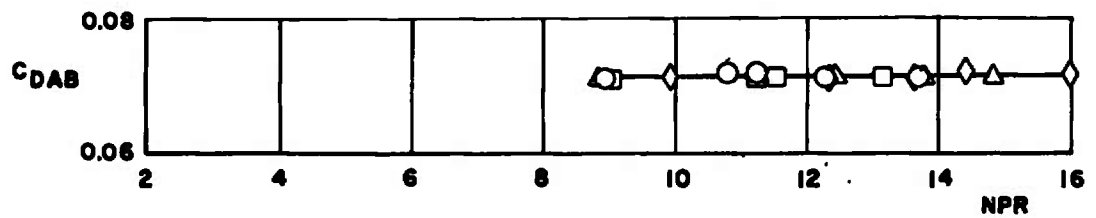
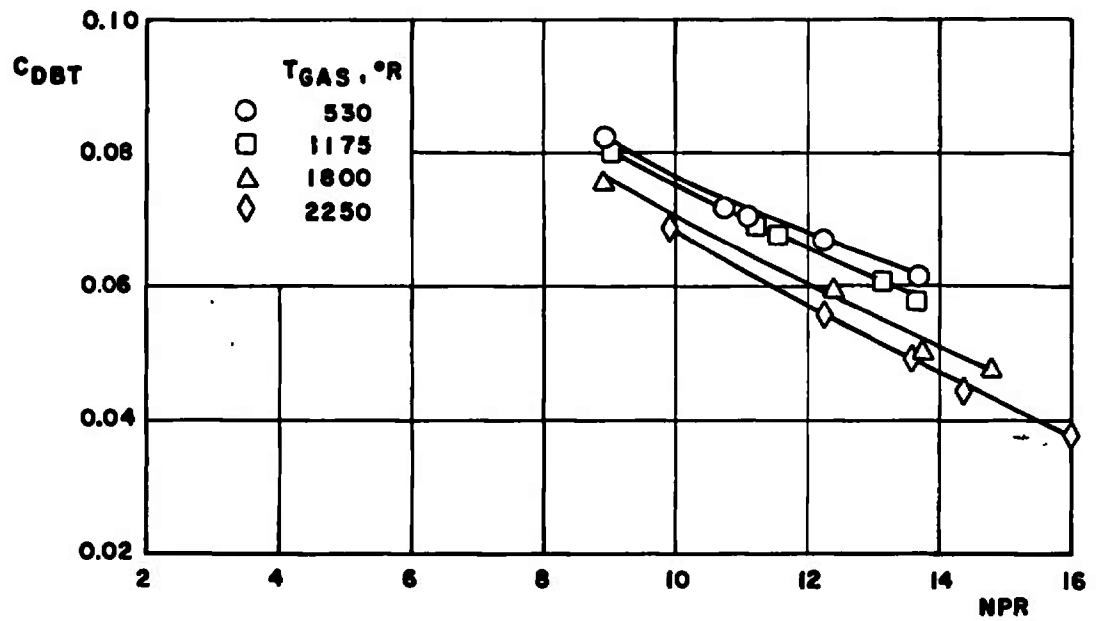
Fig. 10 Effect of Nozzle Pressure Ratio on Turbojet Nozzle Component Drag Coefficients at Various Exhaust Jet Temperatures Using a Water-Cooled Combustor at  $Re = 2.5 \times 10^6/ft$



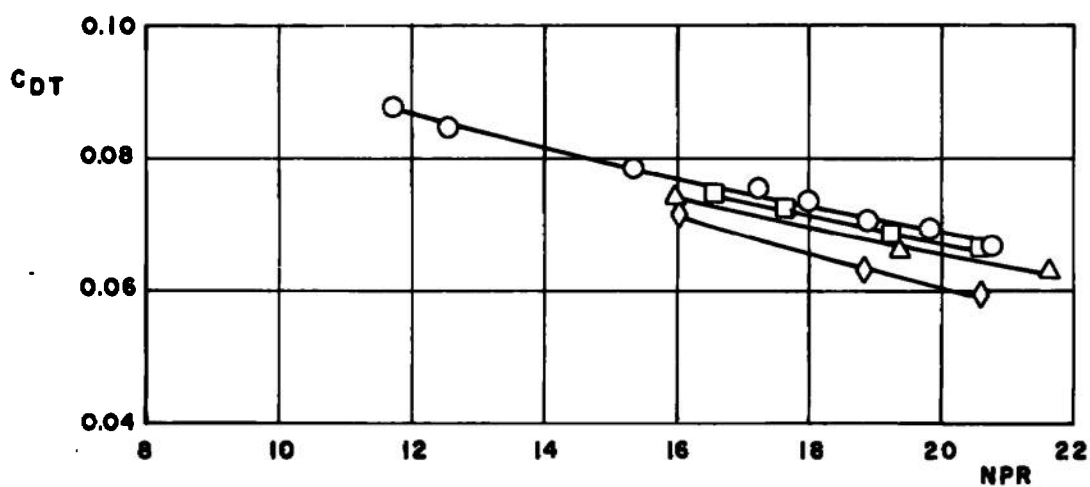
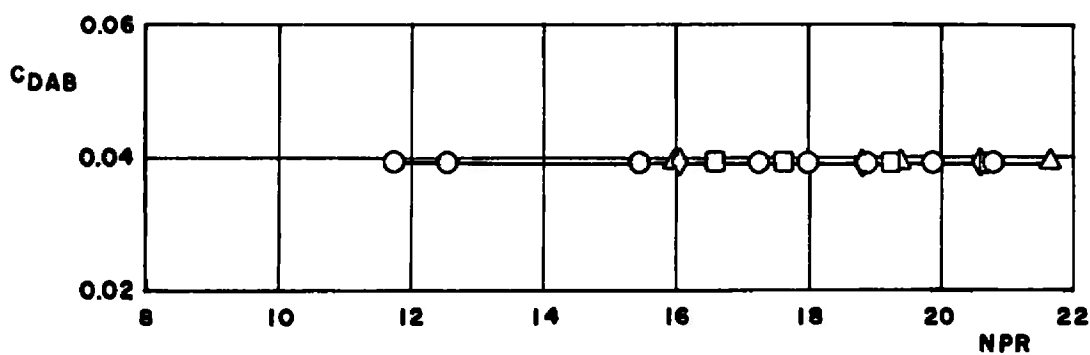
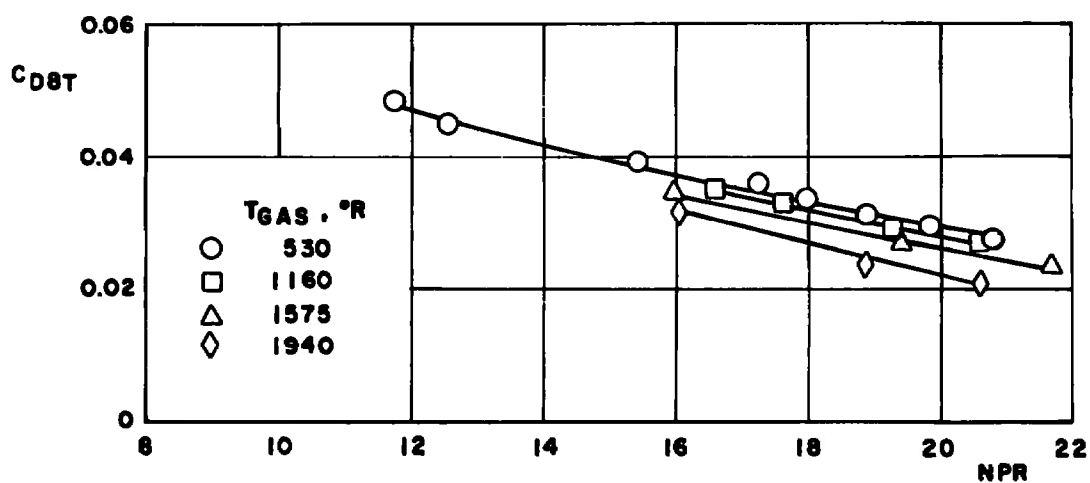
b.  $M_\infty = 0.9$   
Fig. 10 Continued



c.  $M_\infty = 1.1$   
Fig. 10 Continued



d.  $M_{\infty} = 1.2$   
Fig. 10 Continued



e.  $M_{\infty} = 1.5$   
Fig. 10 Concluded

$$M_{\infty} = 0.85$$

$$\Delta C_D = (C_{D\text{JET-ON}} - C_{D\text{JET-OFF}})$$

Convergent Nozzle

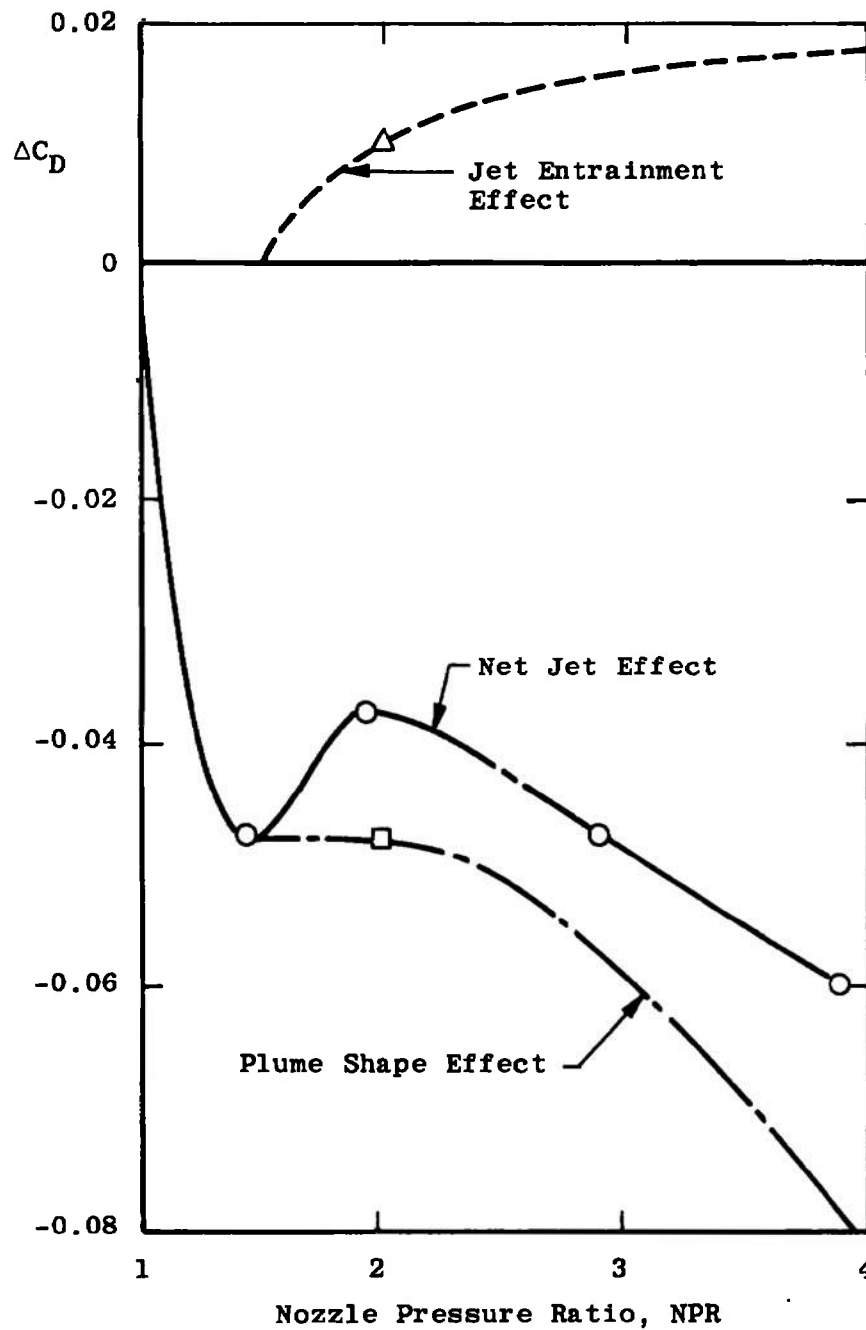


Fig. 11 Qualitative Effect of Entrainment and Plume Shape on Boattail Drag

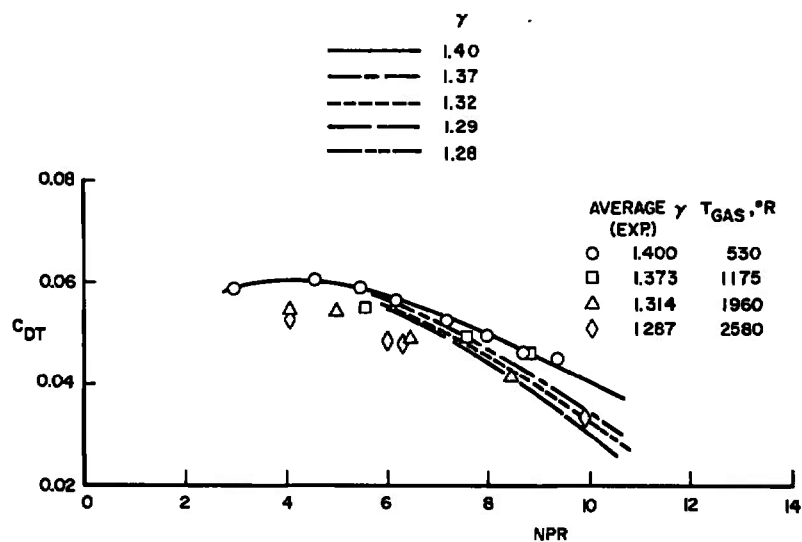
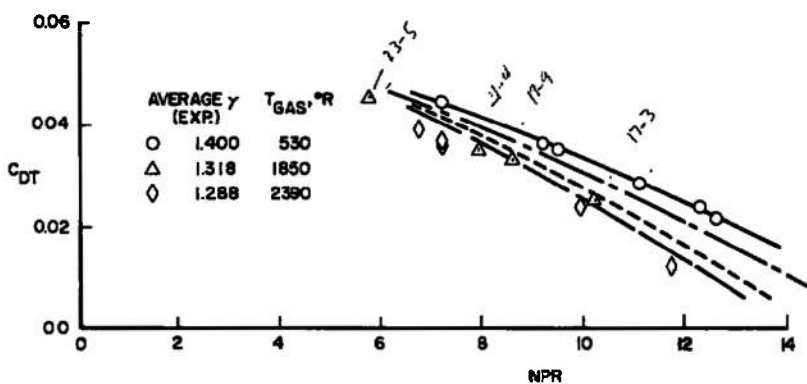
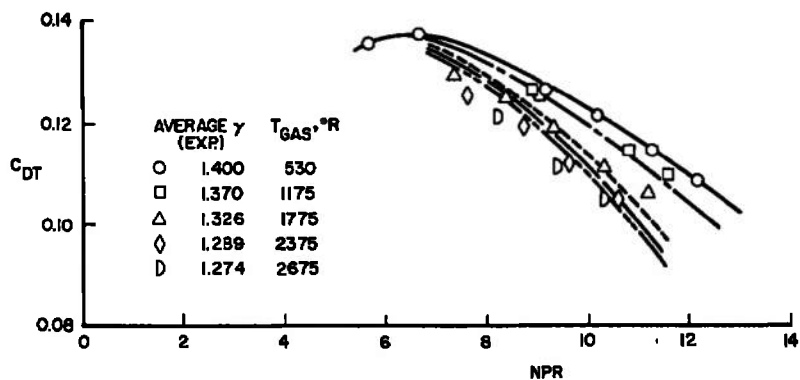
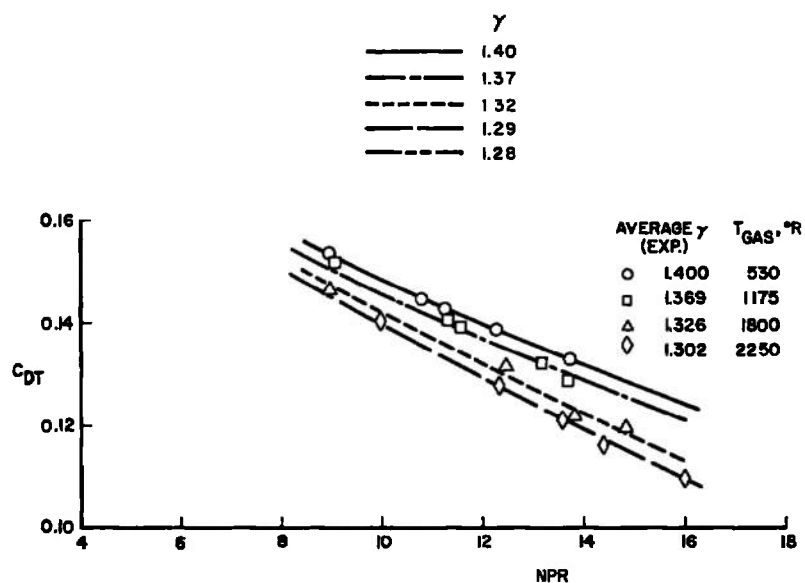
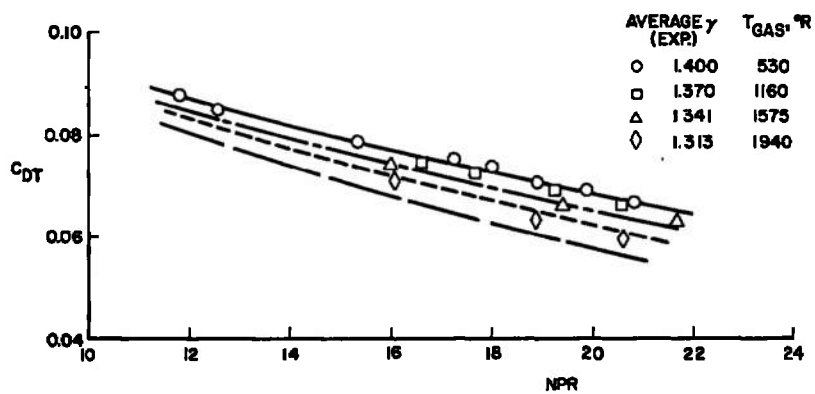
a.  $M_\infty = 0.6$ b.  $M_\infty = 0.9$ c.  $M_\infty = 1.1$ 

Fig. 12 Comparison of the Cold-Flow Data Corrected for Specific Heat Ratios to the Experimental Hot-Flow Data at  $Re = 2.5 \times 10^6 / ft$



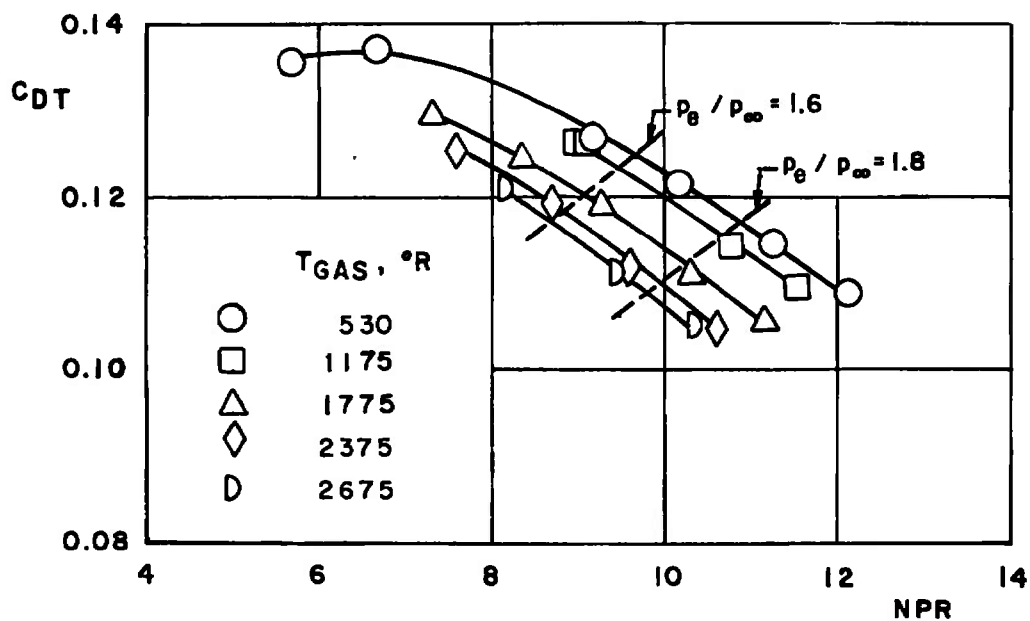
d.  $M_\infty = 1.2$



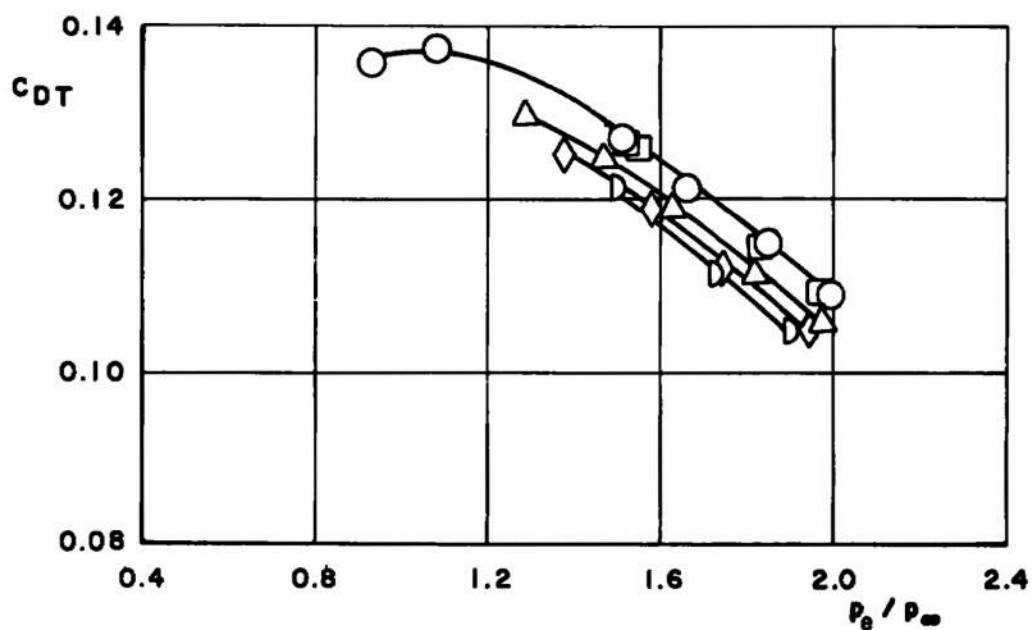
e.  $M_\infty = 1.5$

Fig. 12 Concluded





a. Boattail Drag Coefficient as a Function of Nozzle Total Pressure Ratio at  $M_\infty = 1.1$



b. Boattail Drag Coefficient as a Function of Nozzle Static Pressure Ratio at  $M_\infty = 1.1$

Fig. 13 Comparison of Two Methods of Presenting Drag Coefficient Data

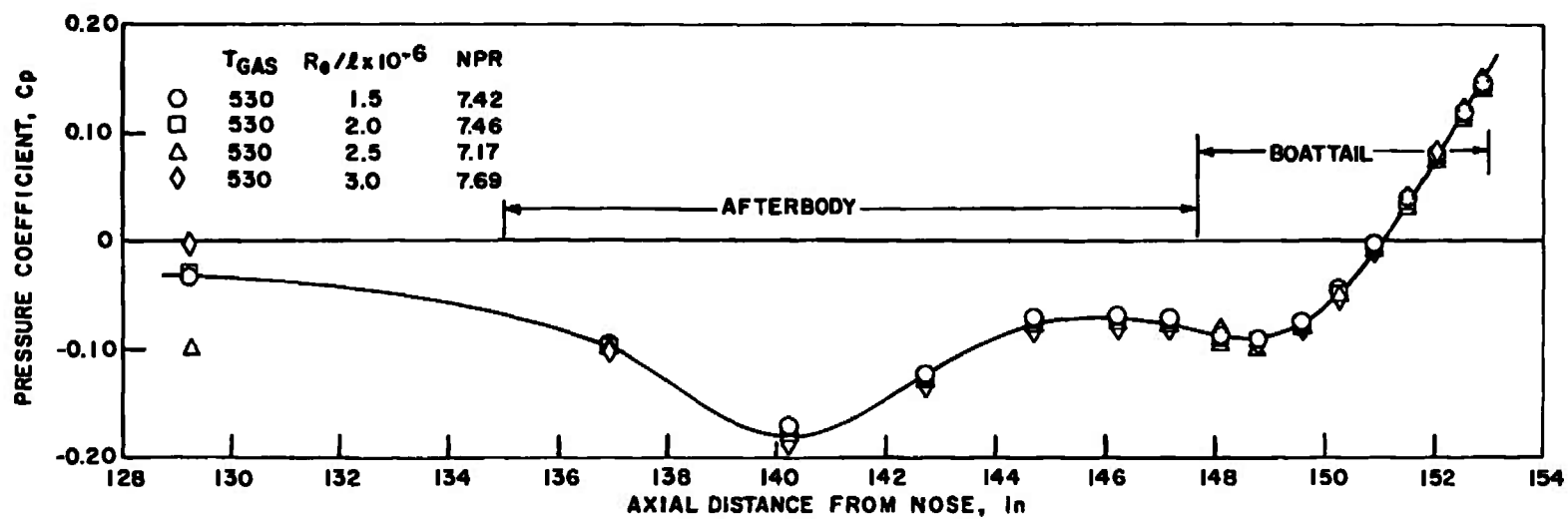
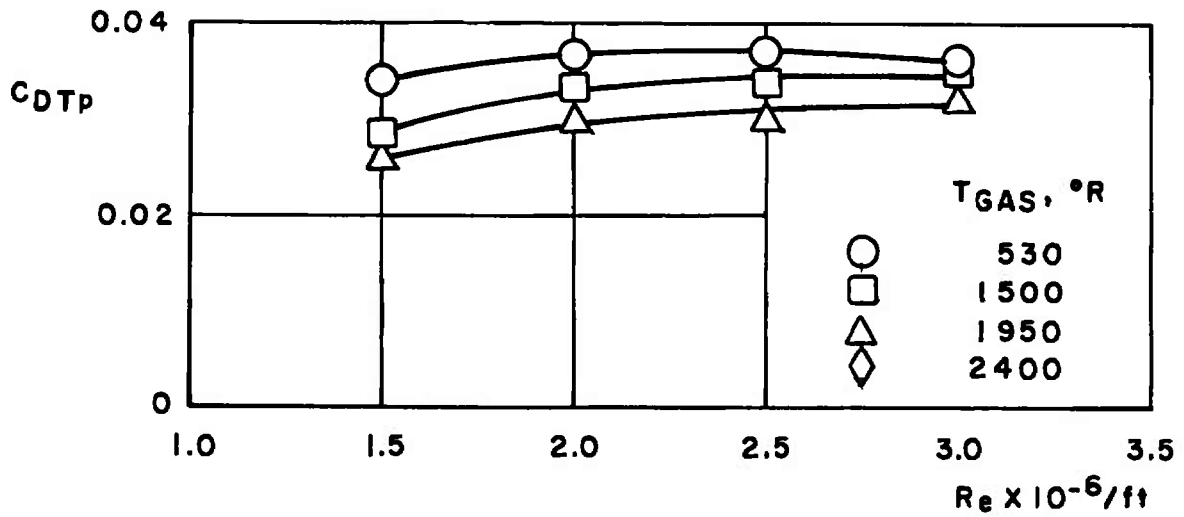
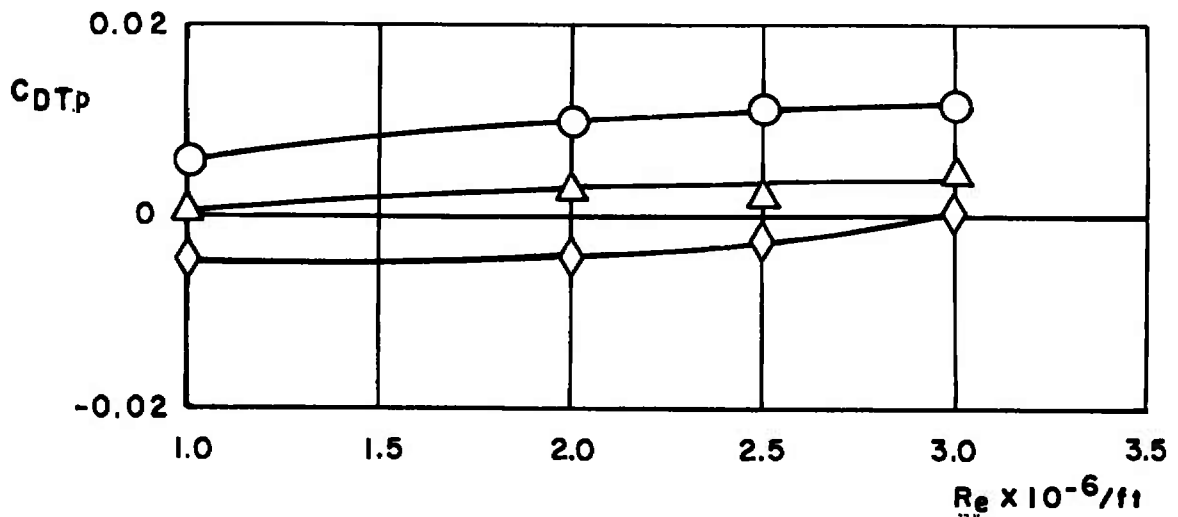


Fig. 14 Effect of Reynolds Number on Boattail Pressure Distribution at  $M_\infty = 0.6$



a.  $M_\infty = 0.6$



b.  $M_\infty = 0.9$

Fig. 15 Effect of Reynolds Number on Boattail Pressure Drag Coefficient at Various Exhaust Jet Temperatures Using a Water-Cooled Combustor at a Nozzle Pressure Ratio of 1.5

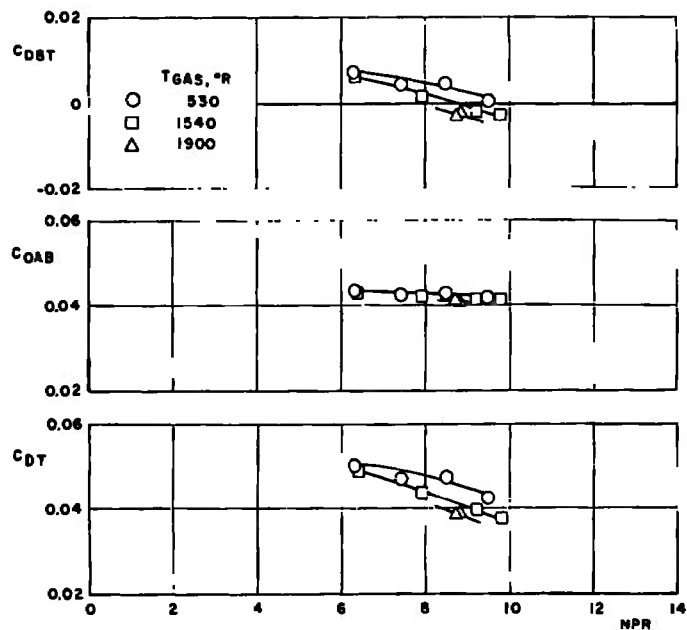
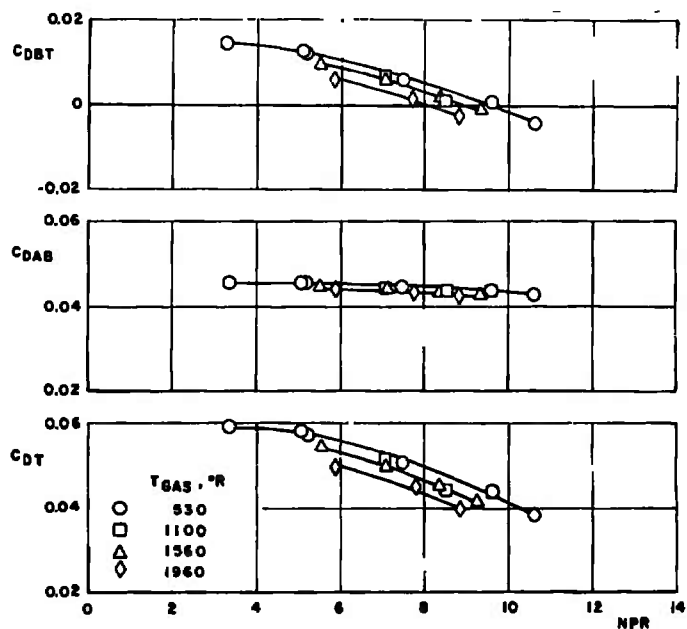
a.  $M_\infty = 0.6, Re = 1.5 \times 10^6/ft$ b.  $M_\infty = 0.6, Re = 2.0 \times 10^6/ft$ 

Fig. 16 Effect of Nozzle Pressure Ratio on Component Drag Coefficients at Various Reynolds Numbers Using a Water-Cooled Combustor

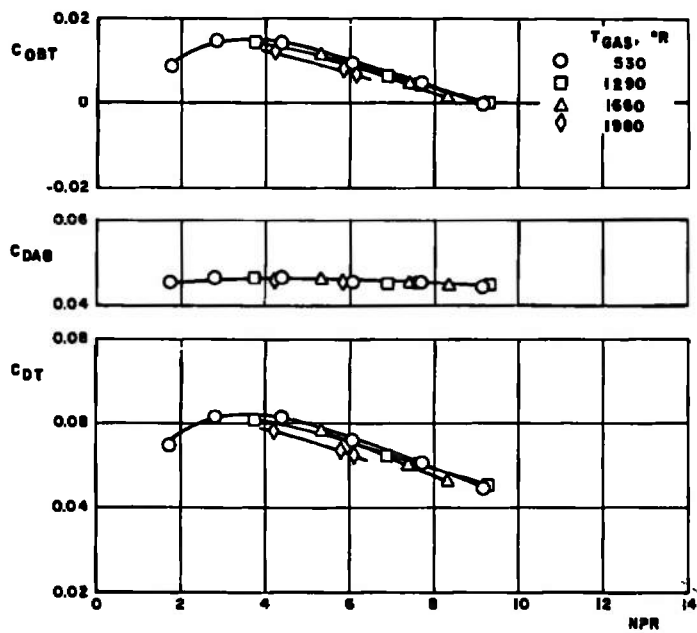
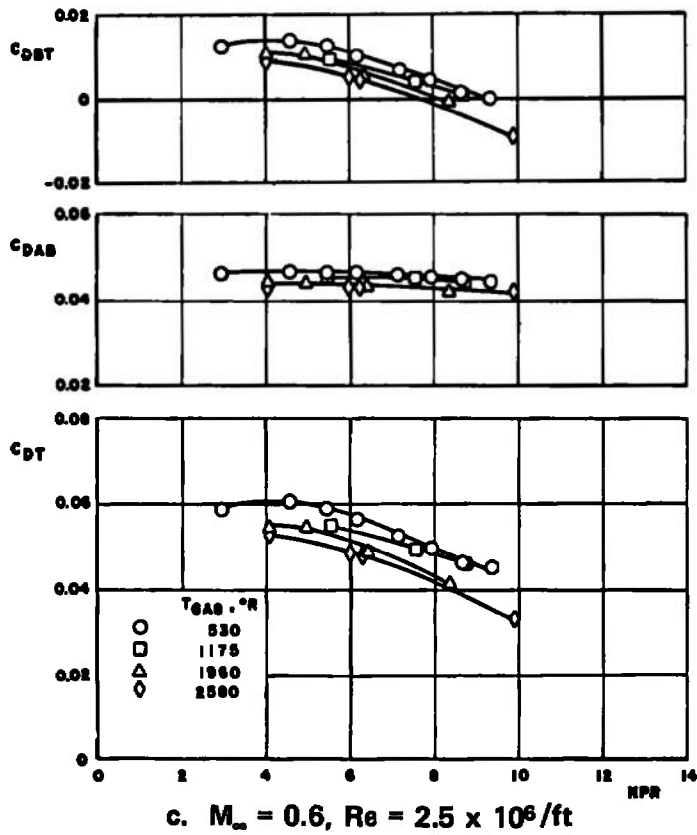
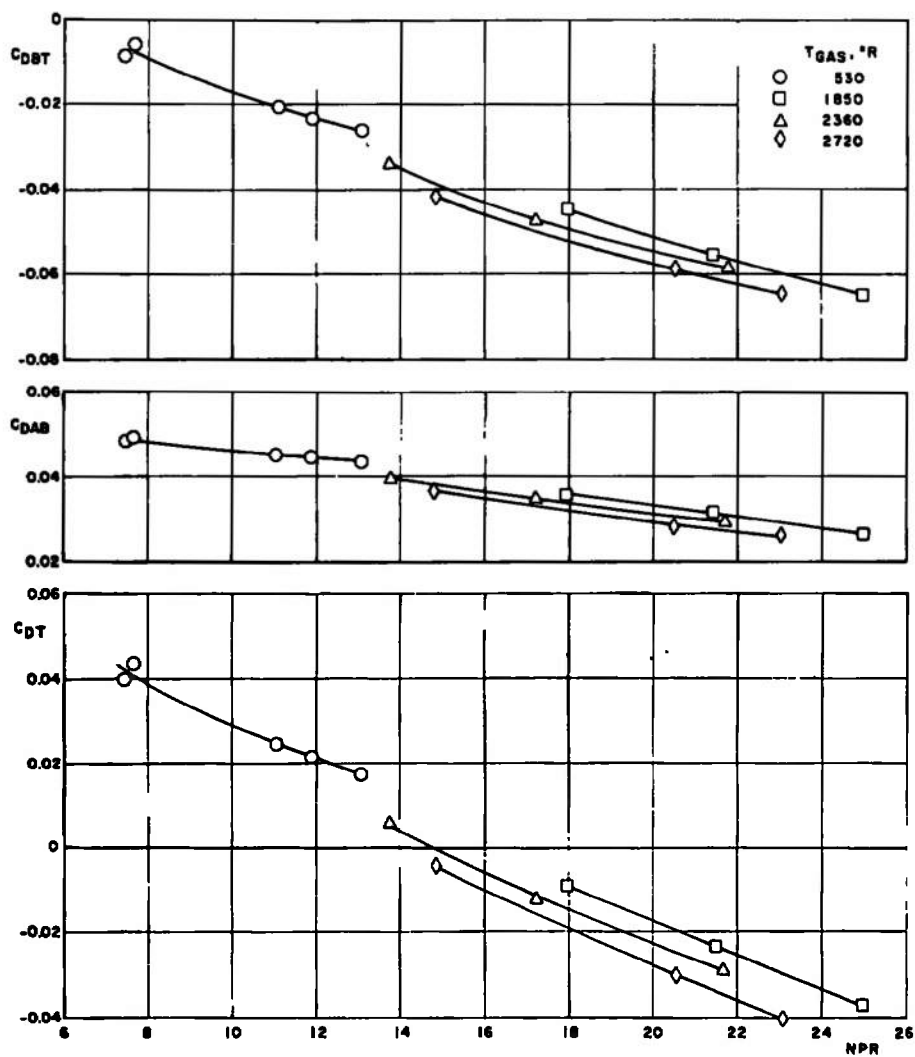
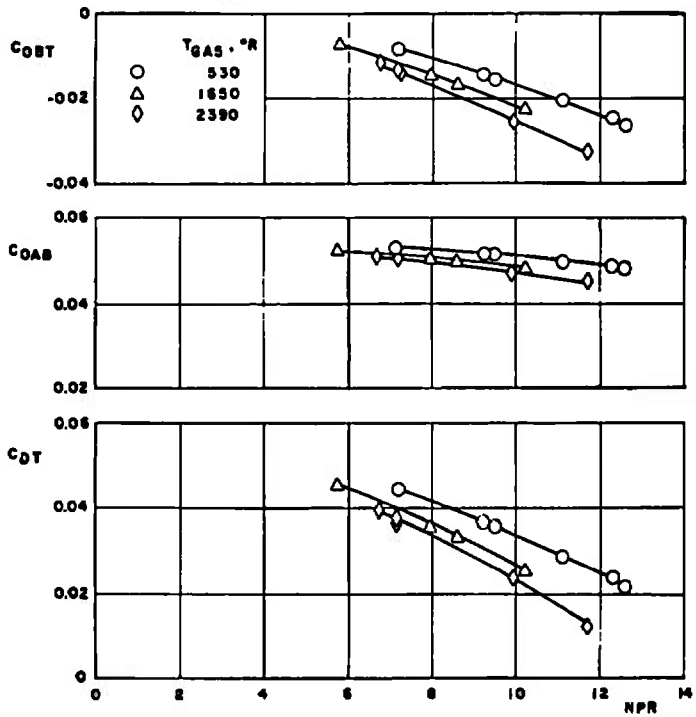
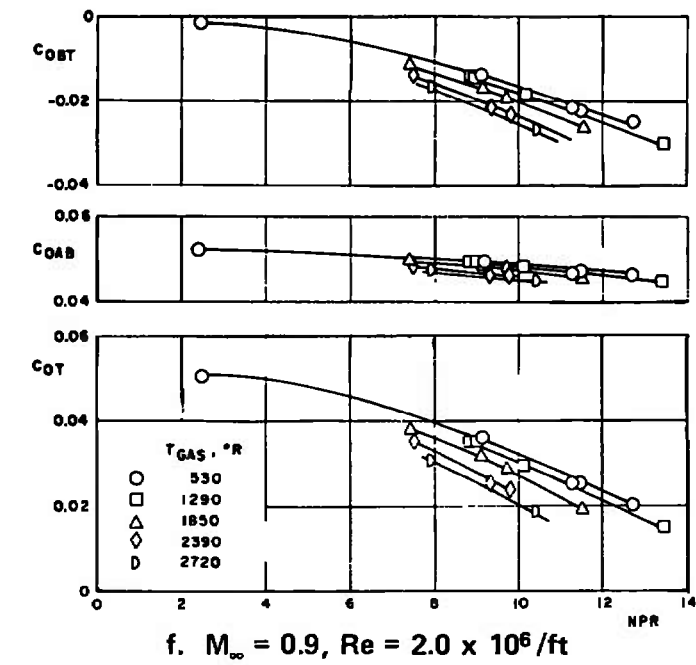


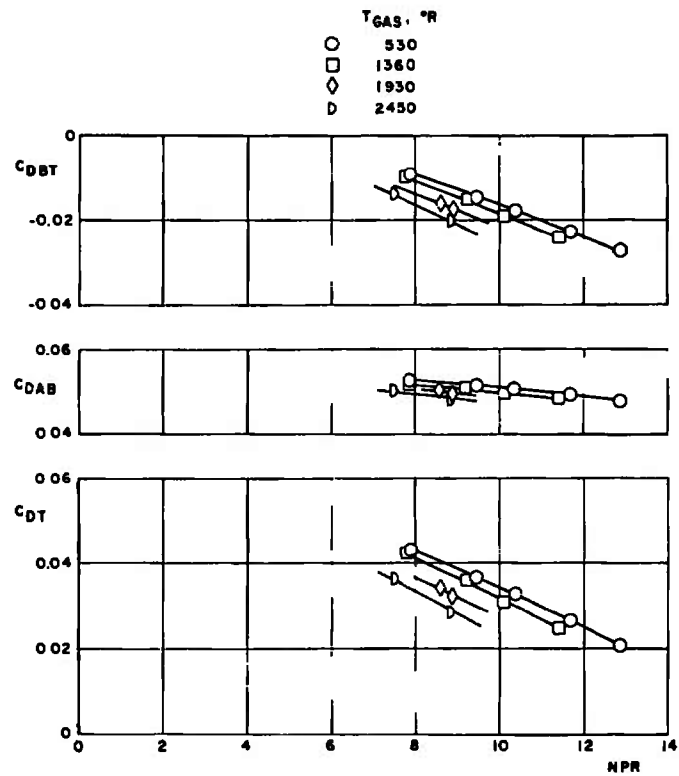
Fig. 16 Continued



e.  $M_\infty = 0.9$ ,  $Re = 1.0 \times 10^6/ft$   
Fig. 16 Continued



g.  $M_\infty = 0.9, Re = 2.5 \times 10^6/ft$   
Fig. 16 Continued



h.  $M_\infty = 0.9$ ,  $Re = 3.0 \times 10^6 / ft$   
Fig. 16 Concluded



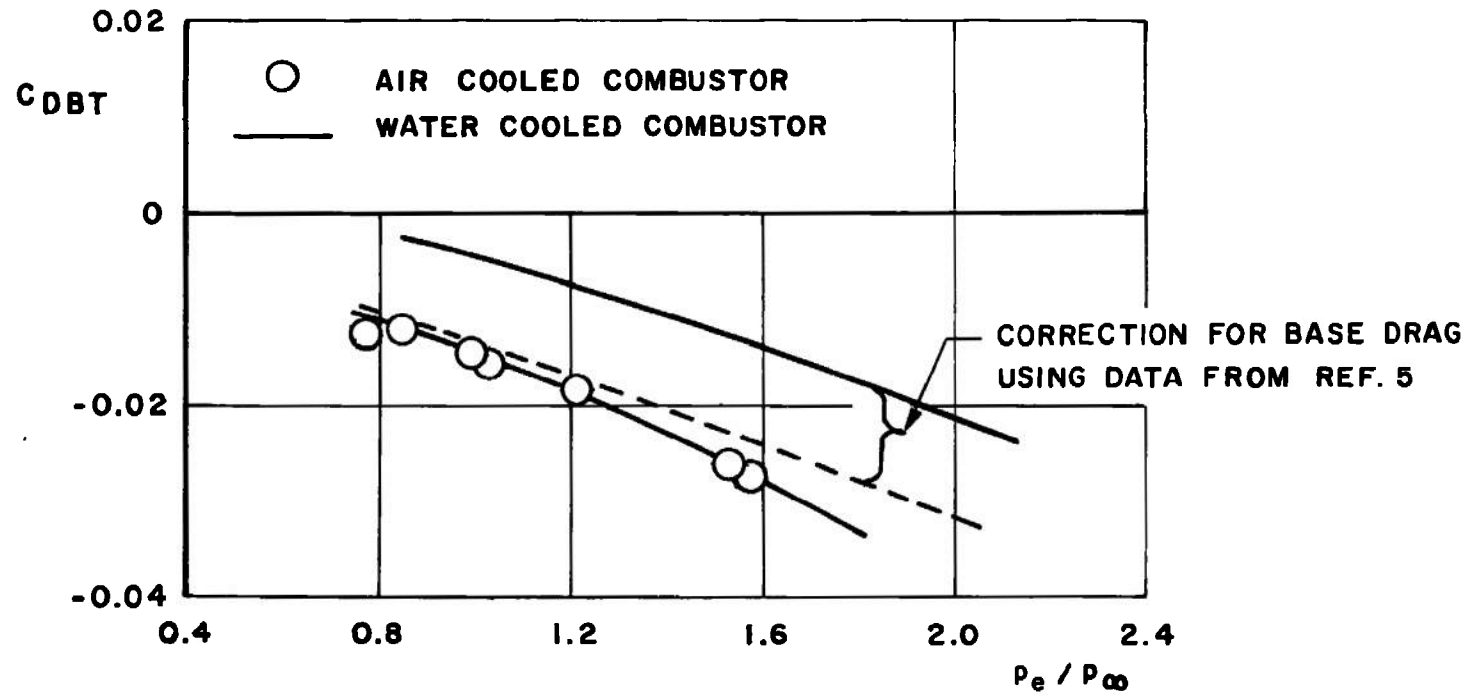


Fig. 17 Comparison of Boattail Drag Coefficient Levels Using Water-Cooled and Air-Cooled Combustors at  $M_\infty = 0.9$

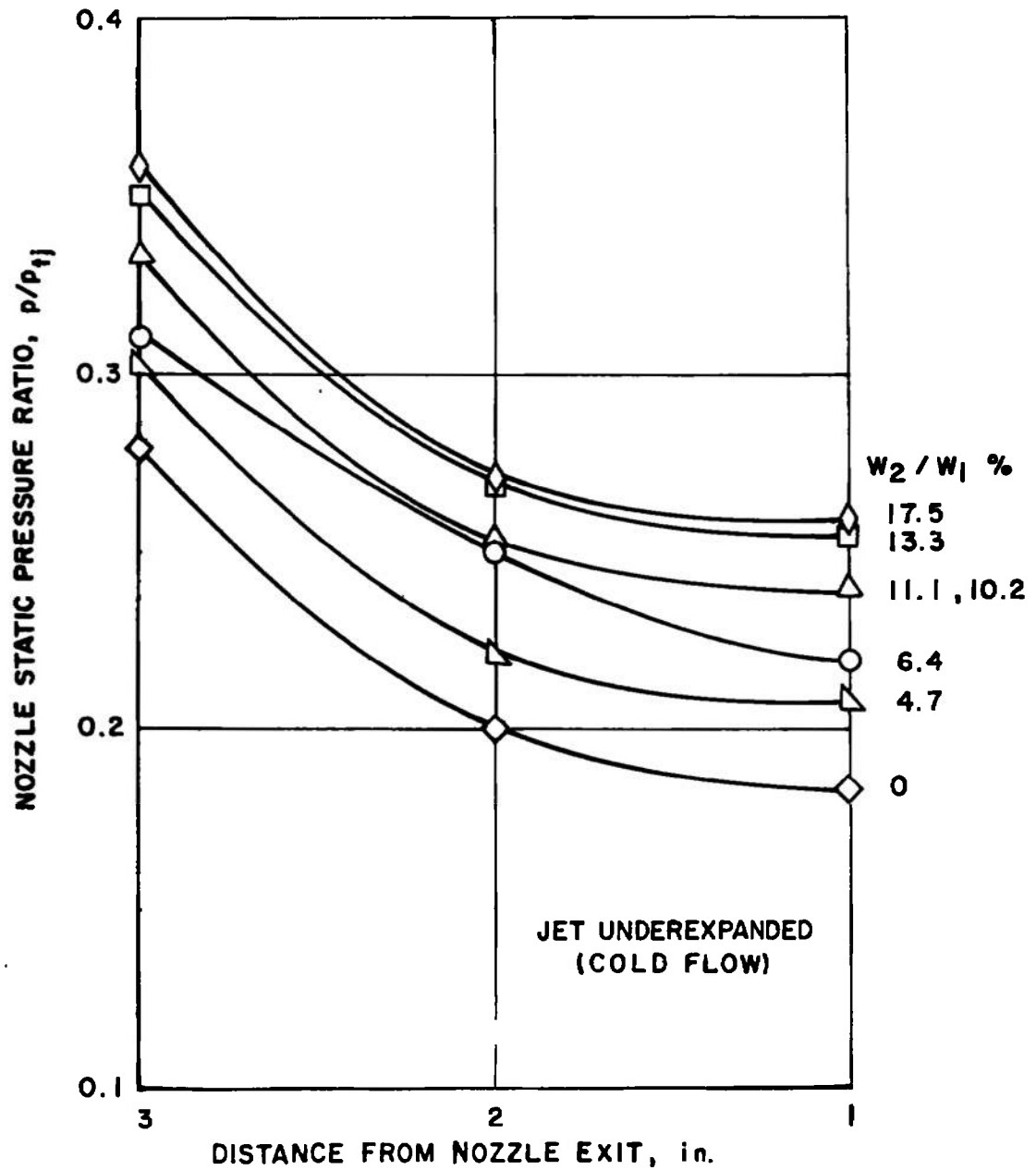


Fig. 18 Military Nozzle Internal Pressure Distribution Cold Flow Using an Air-Cooled Combustor

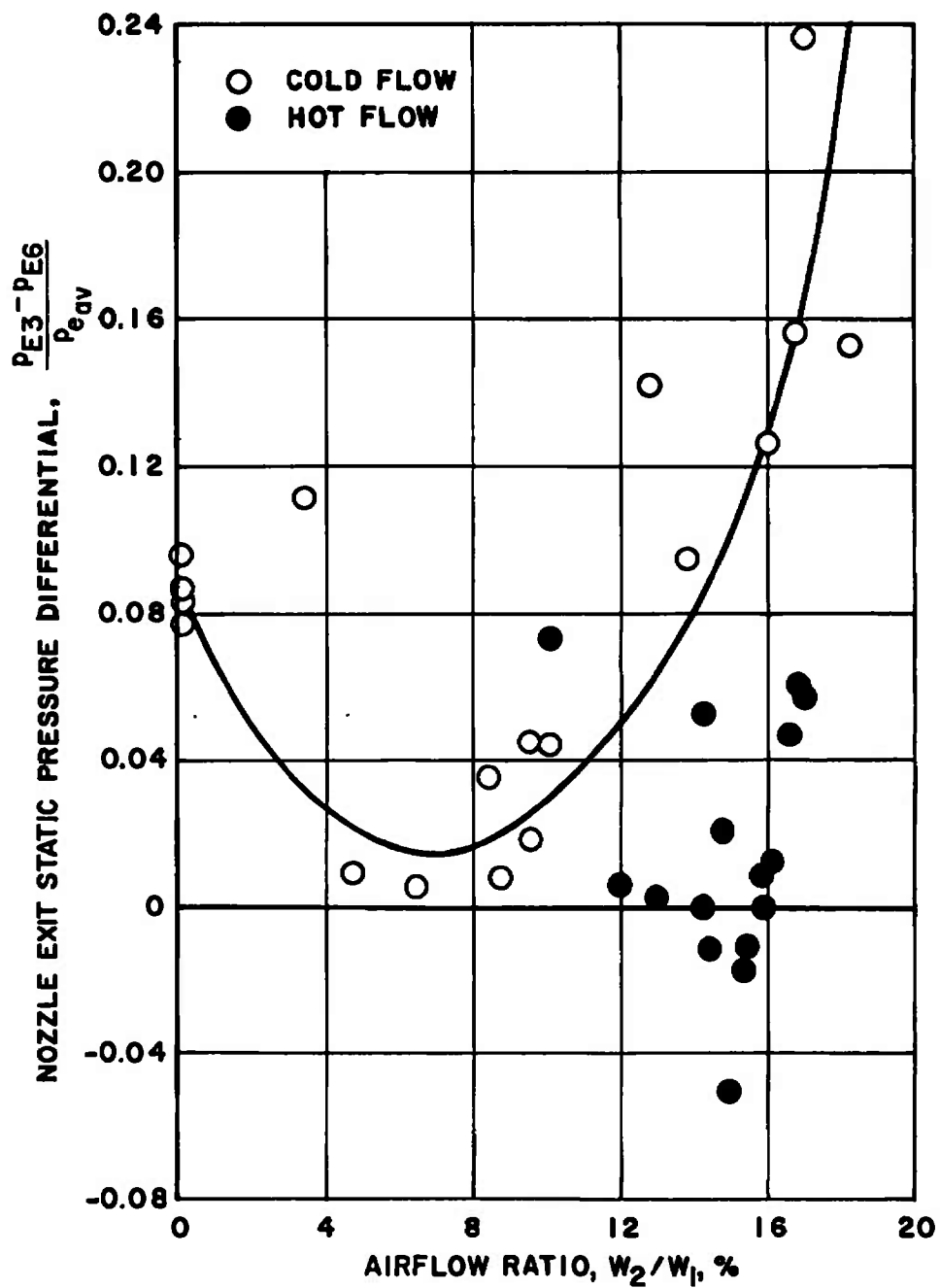


Fig. 19 Effect of Secondary Airflow Ratio on Transverse Nozzle Static Pressure Using an Air-Cooled Combustor

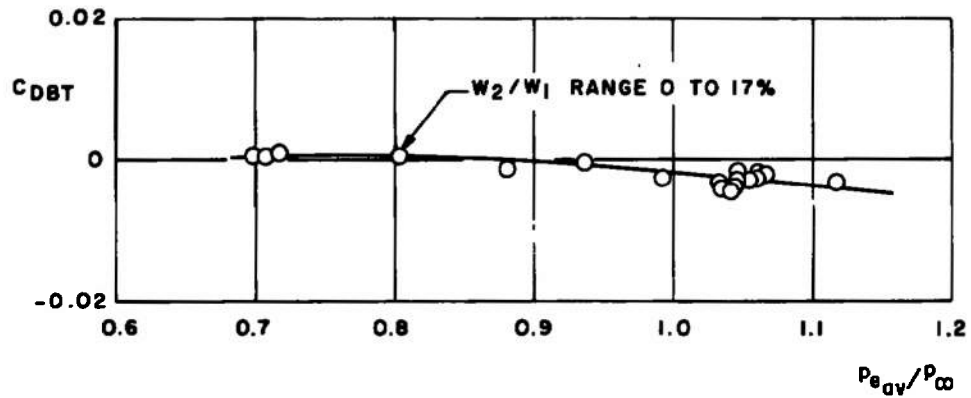
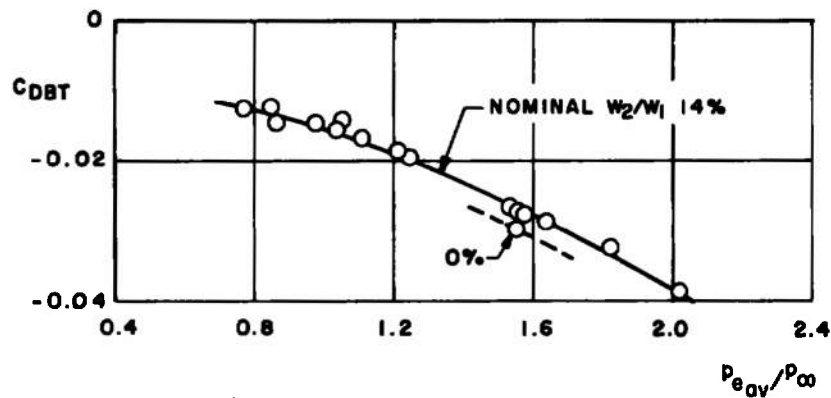
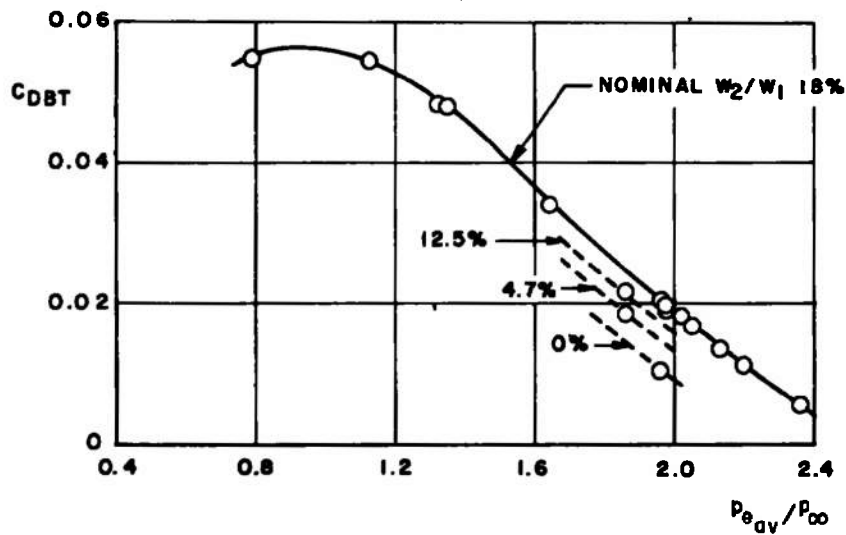
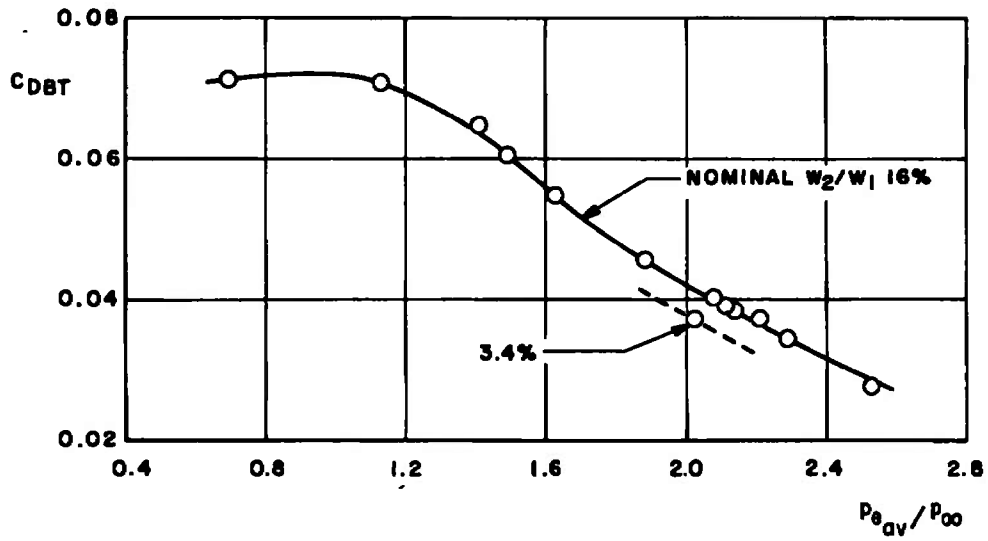
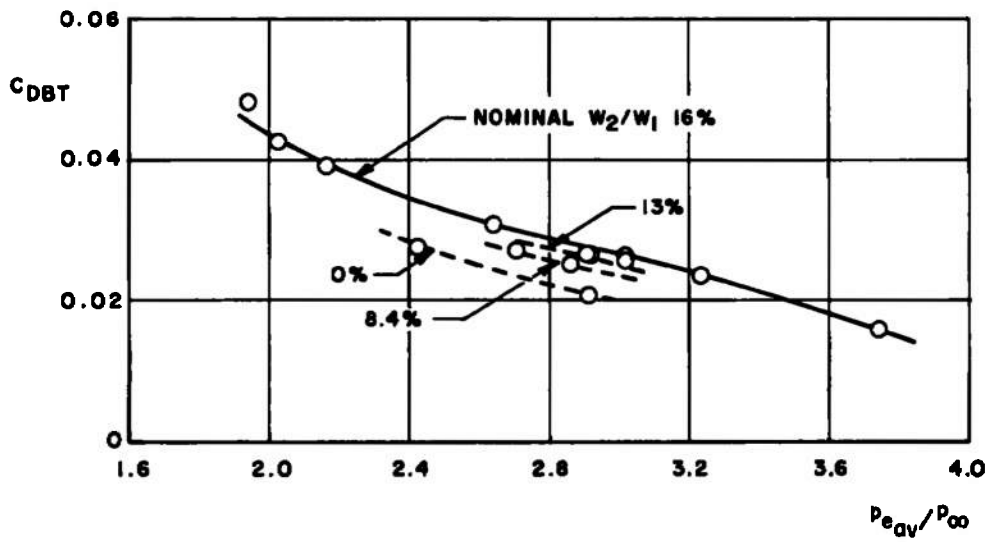
a.  $M_{\infty} = 0.6$ b.  $M_{\infty} = 0.9$ c.  $M_{\infty} = 1.1$ 

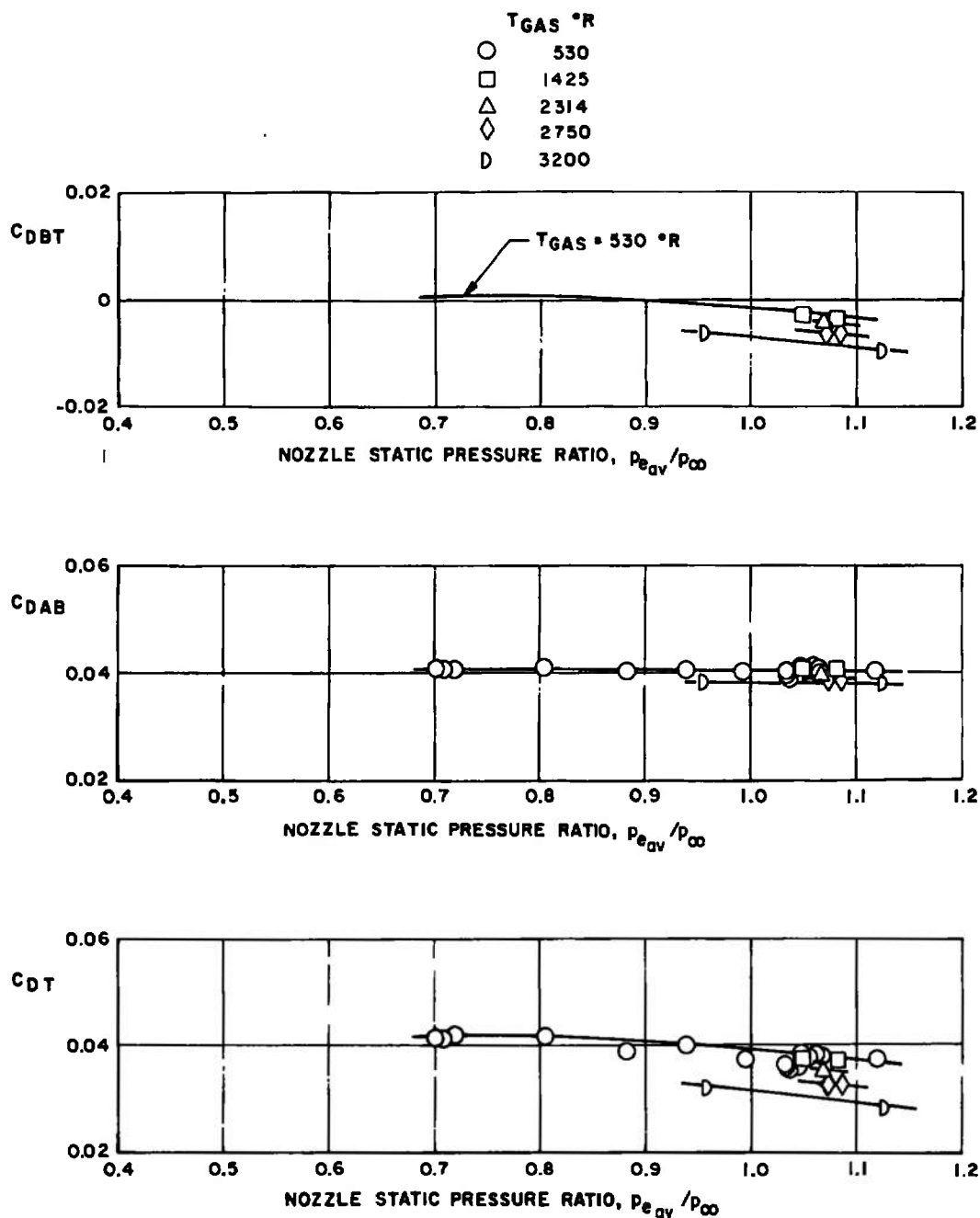
Fig. 20 Effect of Secondary Airflow Ratio on Turbojet Nozzle Component Drag Coefficients, Cold Flow, Using an Air-Cooled Combustor at  $Re = 2.5 \times 10^6/ft$



d.  $M_{\infty} = 1.2$

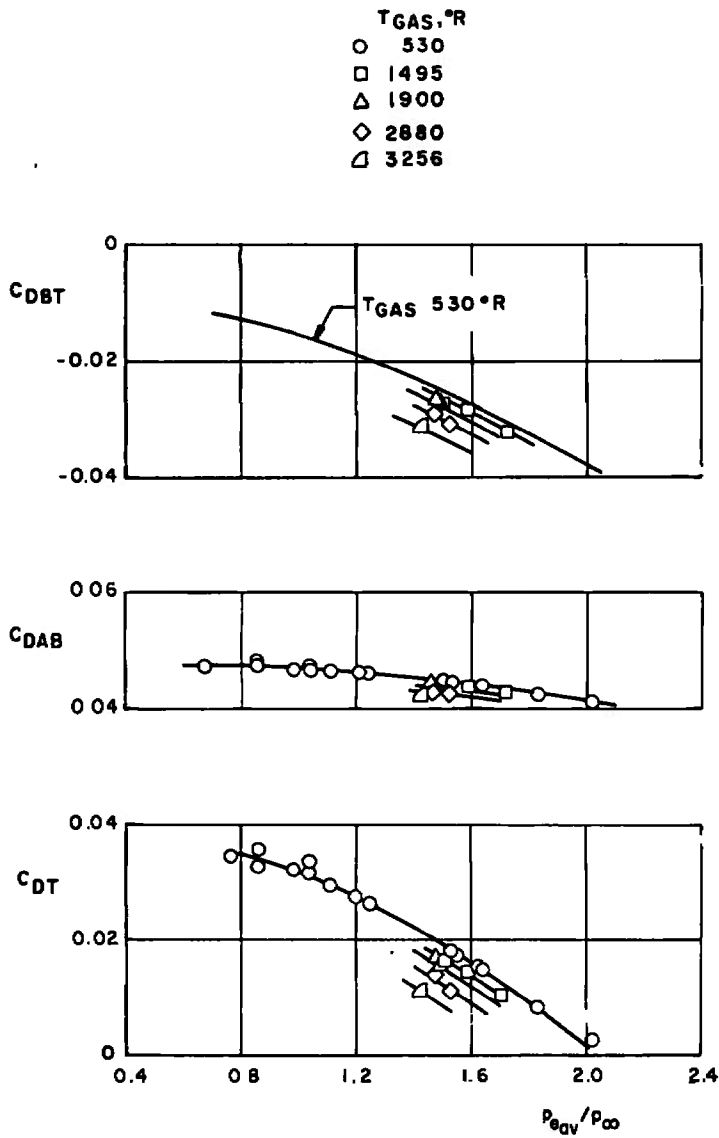


e.  $M_{\infty} = 1.5$   
Fig. 20 Concluded

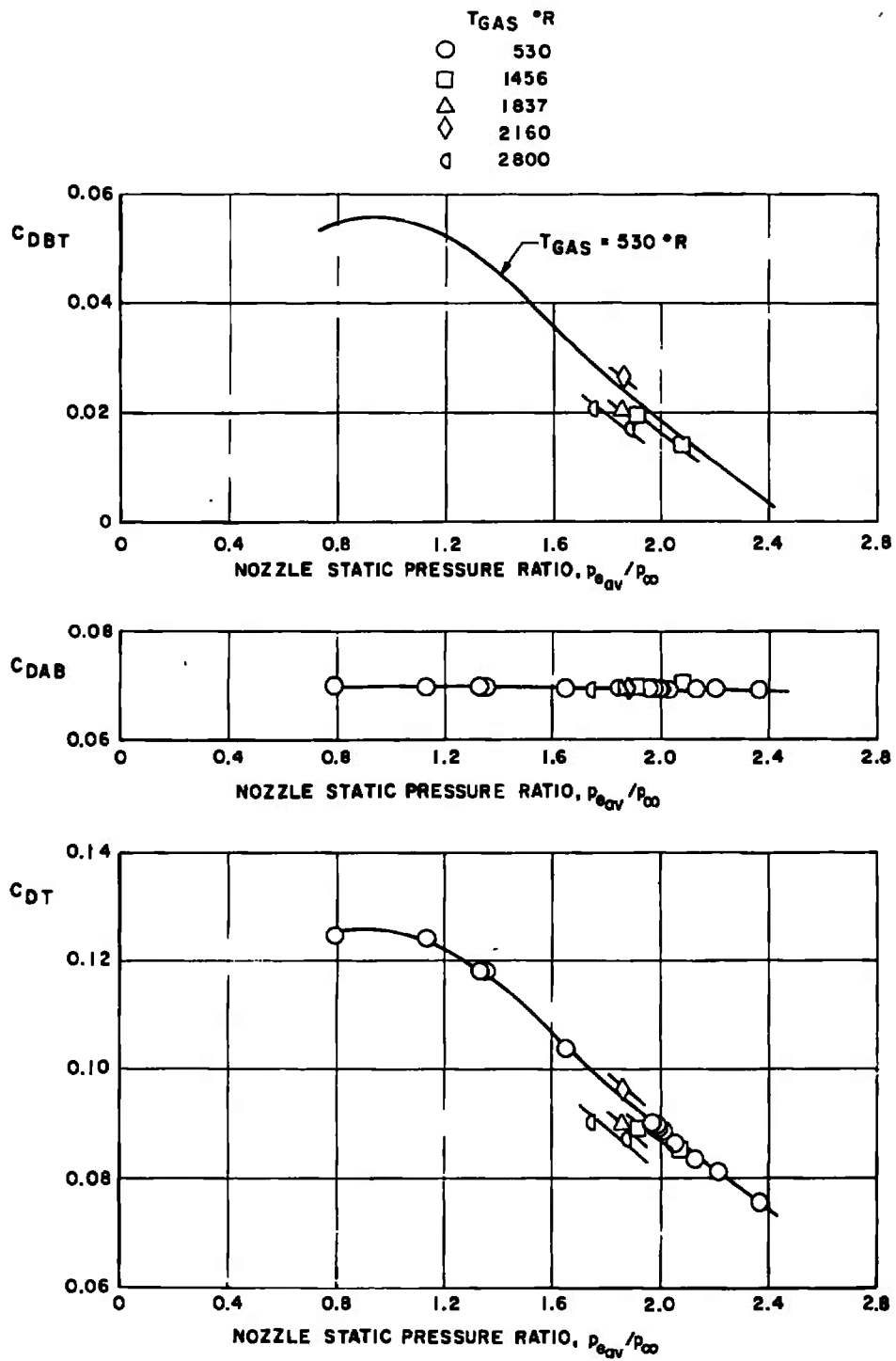


a.  $M_\infty = 0.6$

**Fig. 21 Effect of Nozzle Pressure Ratio on Turbojet Nozzle Component Drag Coefficients at Various Exhaust Jet Temperatures Using an Air-Cooled Combustor at  $Re = 2.5 \times 10^6/ft$**

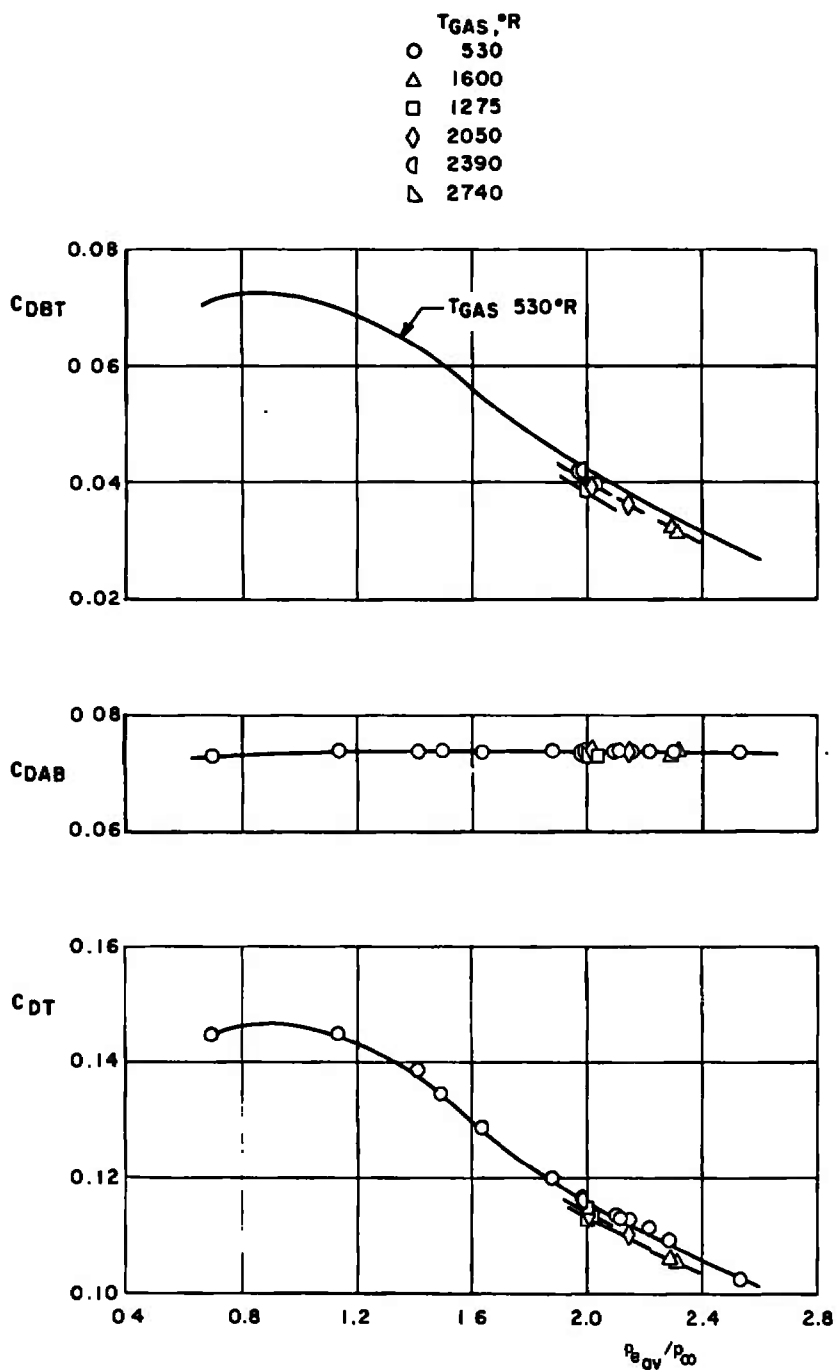


b.  $M_\infty = 0.9$   
Fig. 21 Continued



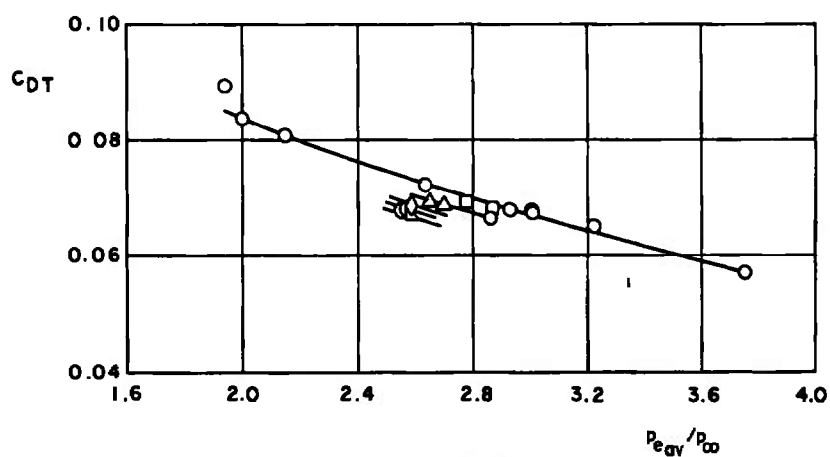
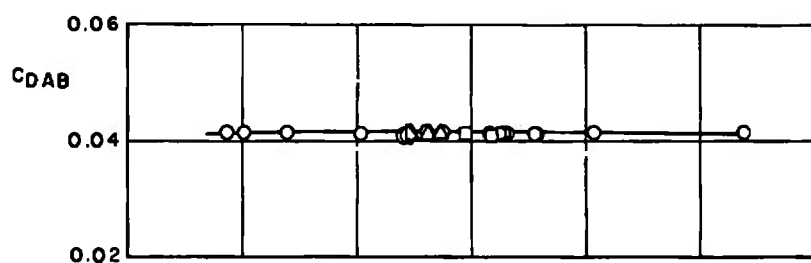
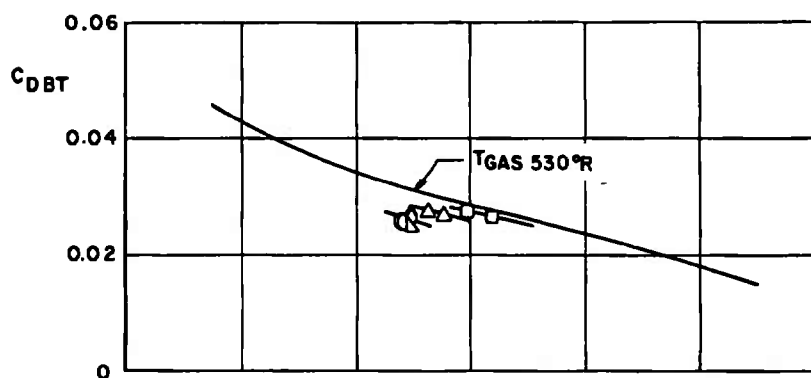
c.  $M_\infty = 1.1$   
 Fig. 21 Continued





d.  $M_\infty = 1.2$   
Fig. 21 Continued

T<sub>GAS</sub>, °R  
 ○ 530  
 □ 1375  
 △ 1990  
 ◇ 2207  
 ◻ 2640  
 ▽ 2930



e.  $M_{\infty} = 1.5$   
 Fig. 21 Concluded

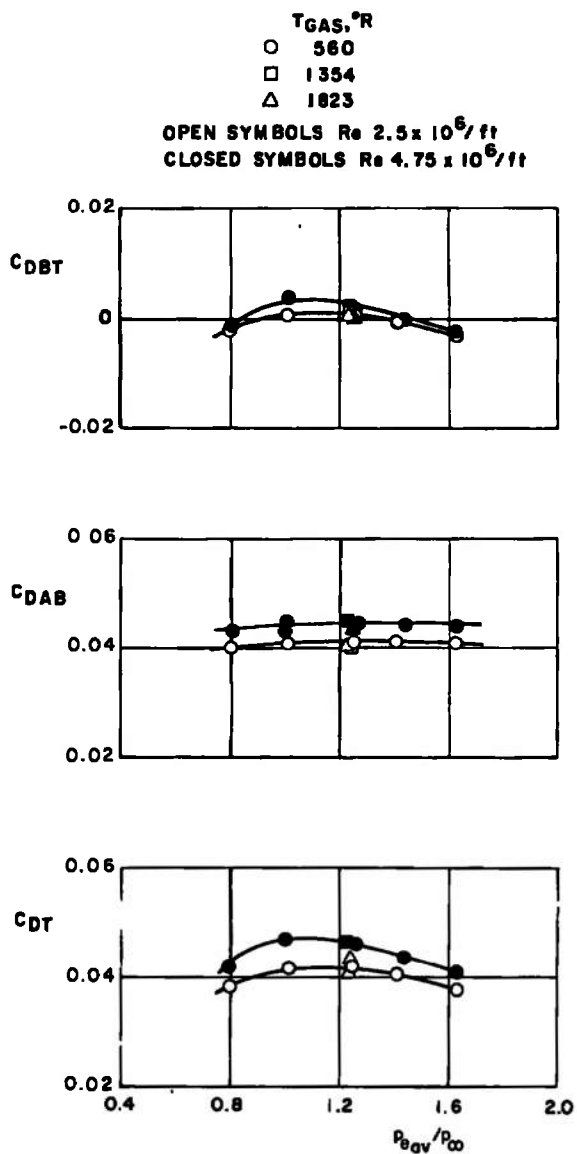
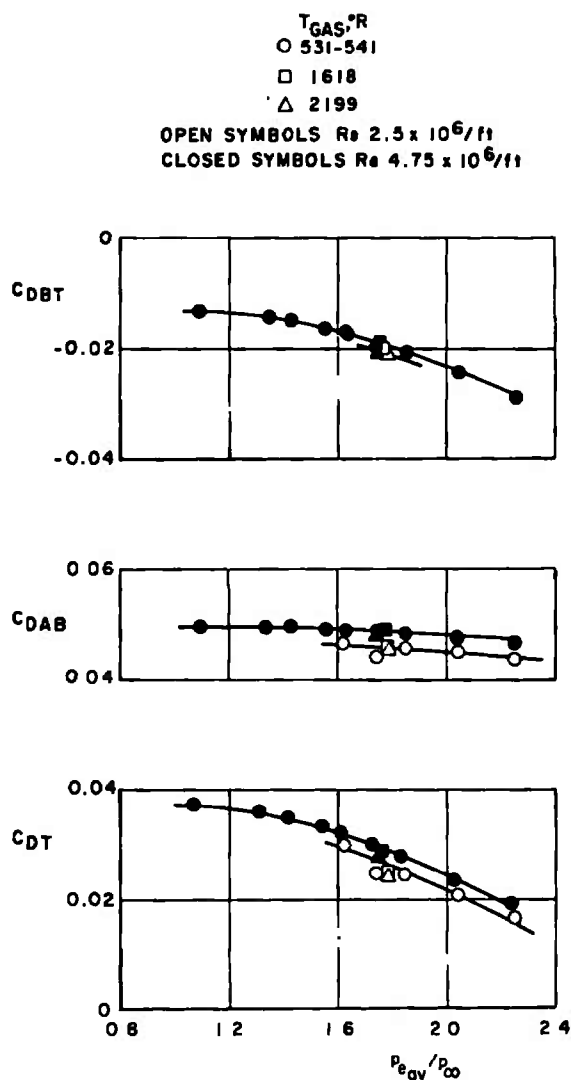
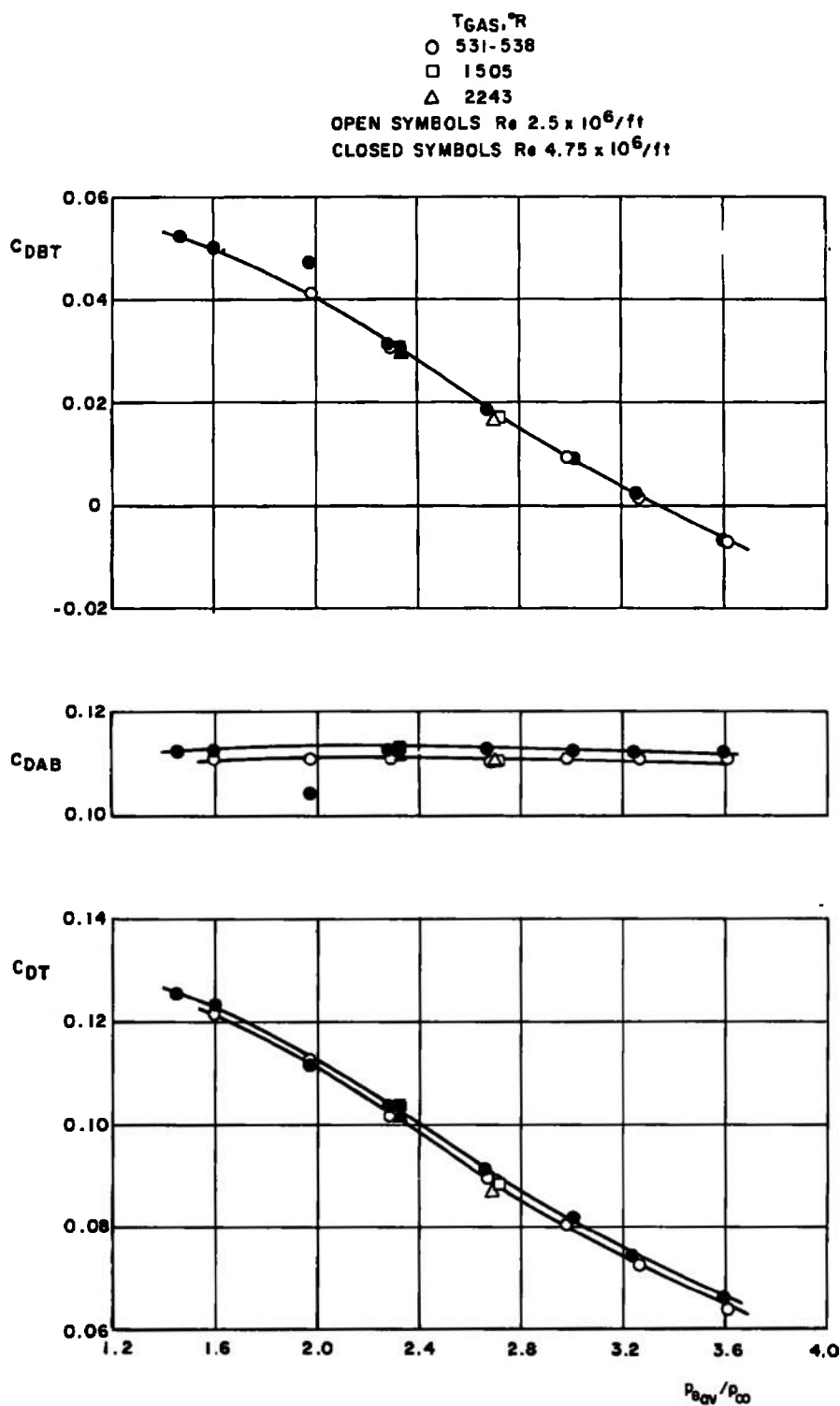


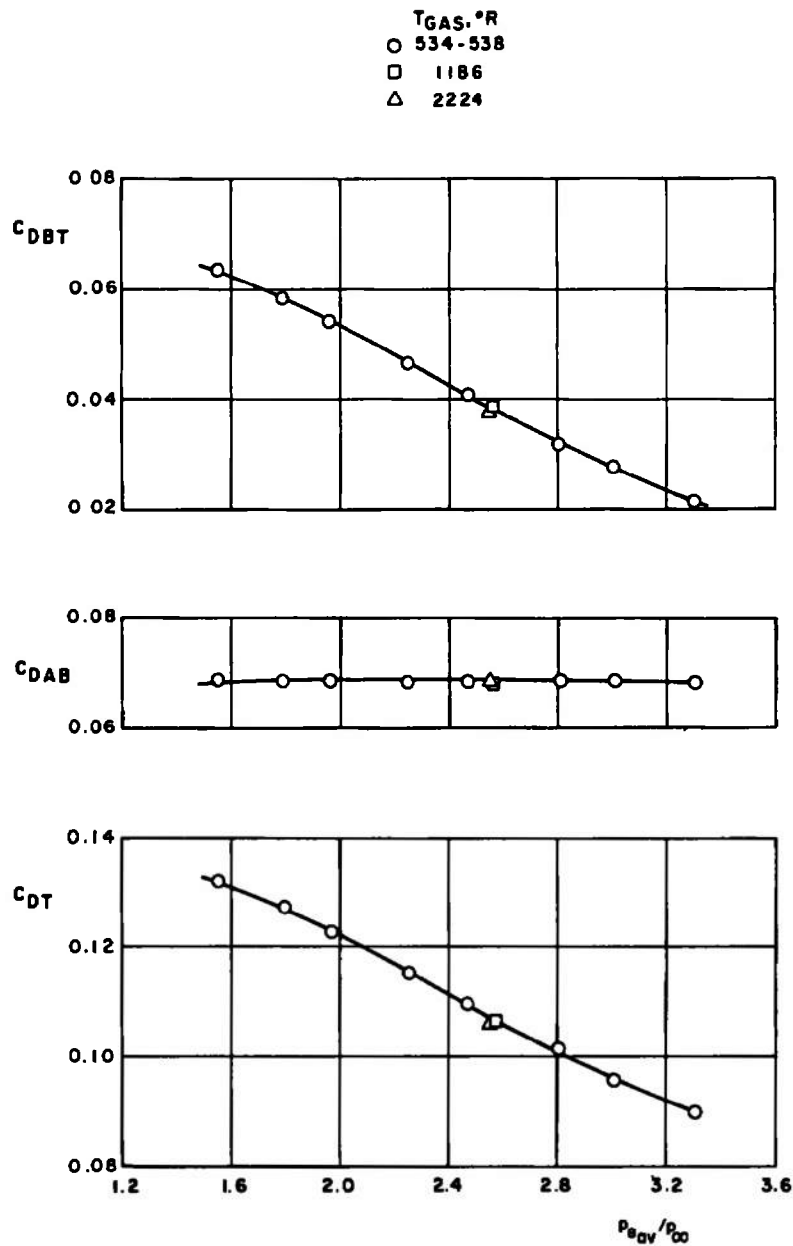
Fig. 22 Effect of Nozzle Pressure Ratio on Turbofan Nozzle Component Drag Coefficients at Various Exhaust Jet Temperatures Using an Air-Cooled Combustor



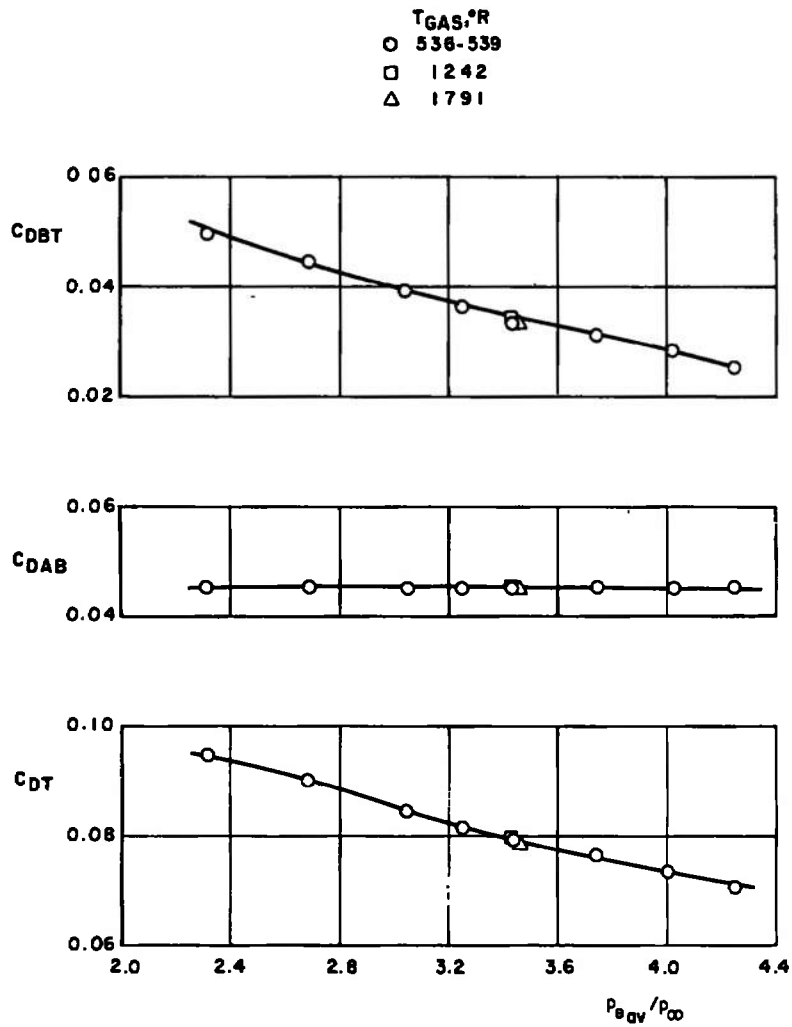
b.  $M_{\infty} = 0.9$   
 Fig. 22 Continued



c.  $M_{\infty} = 1.1$   
 Fig. 22 Continued



d.  $M_\infty = 1.2$ ,  $Re = 2.5 \times 10^6/ft$   
 Fig. 22 Continued



e.  $M_\infty = 1.5$ ,  $Re = 2.5 \times 10^6/ft$   
Fig. 22 Concluded

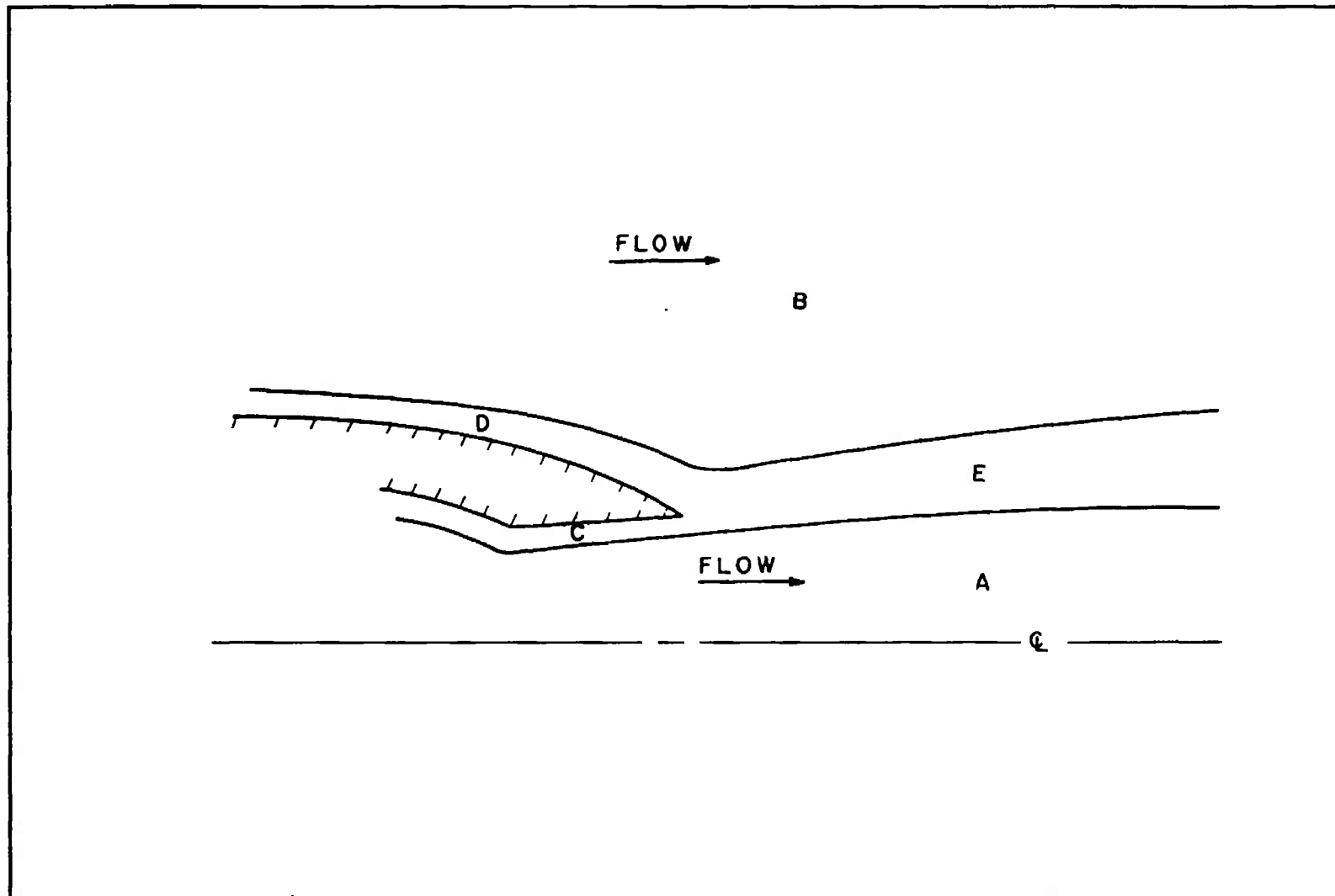


Fig. 23 Schematic of the Various Flow Regions Involved in the Afterbody Drag Calculation Problem



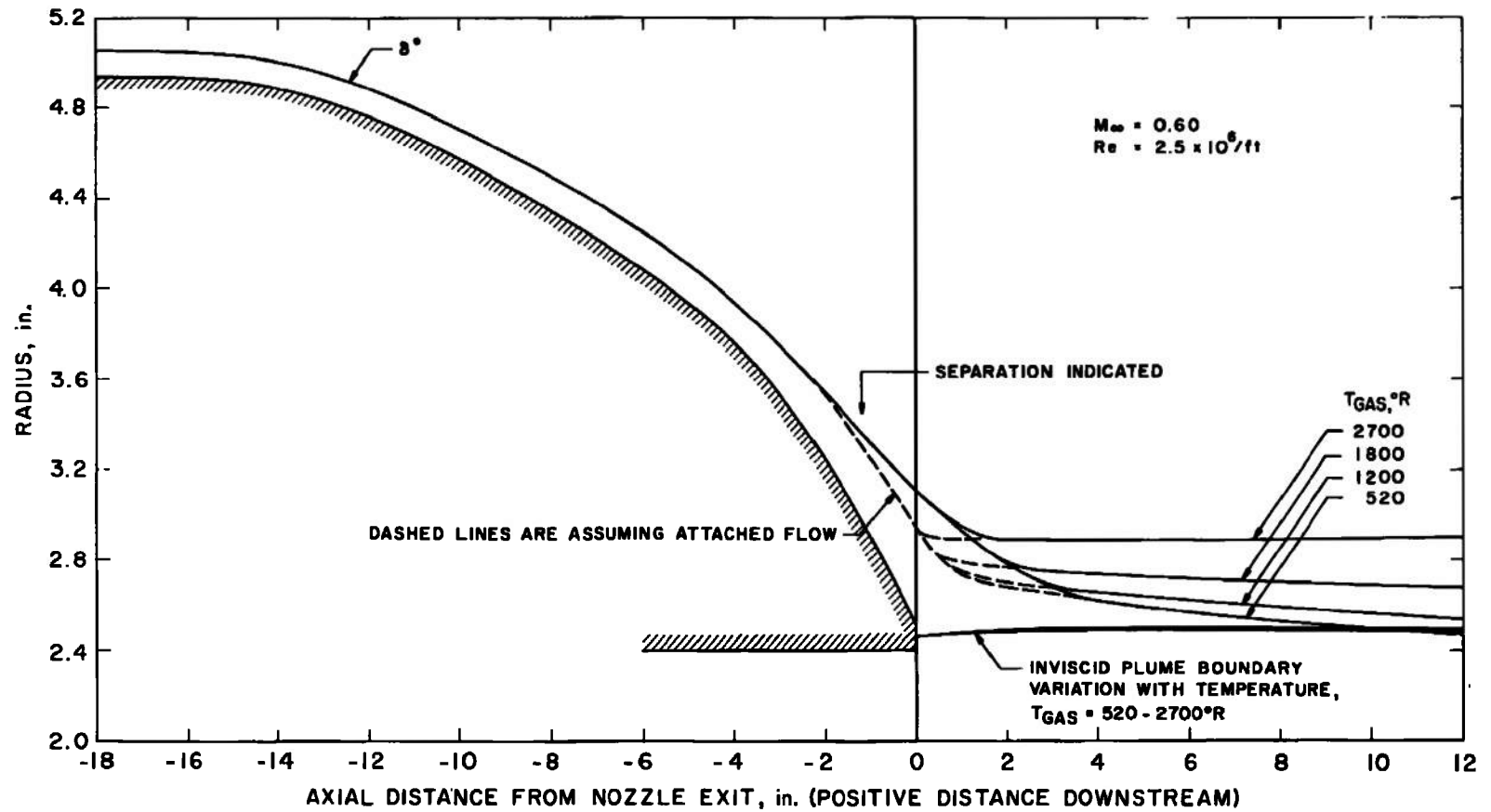


Fig. 24 Effective Displacement Boundaries for the External Flow at  $M_\infty = 0.6$  and  $Re = 2.5 \times 10^6/ft$

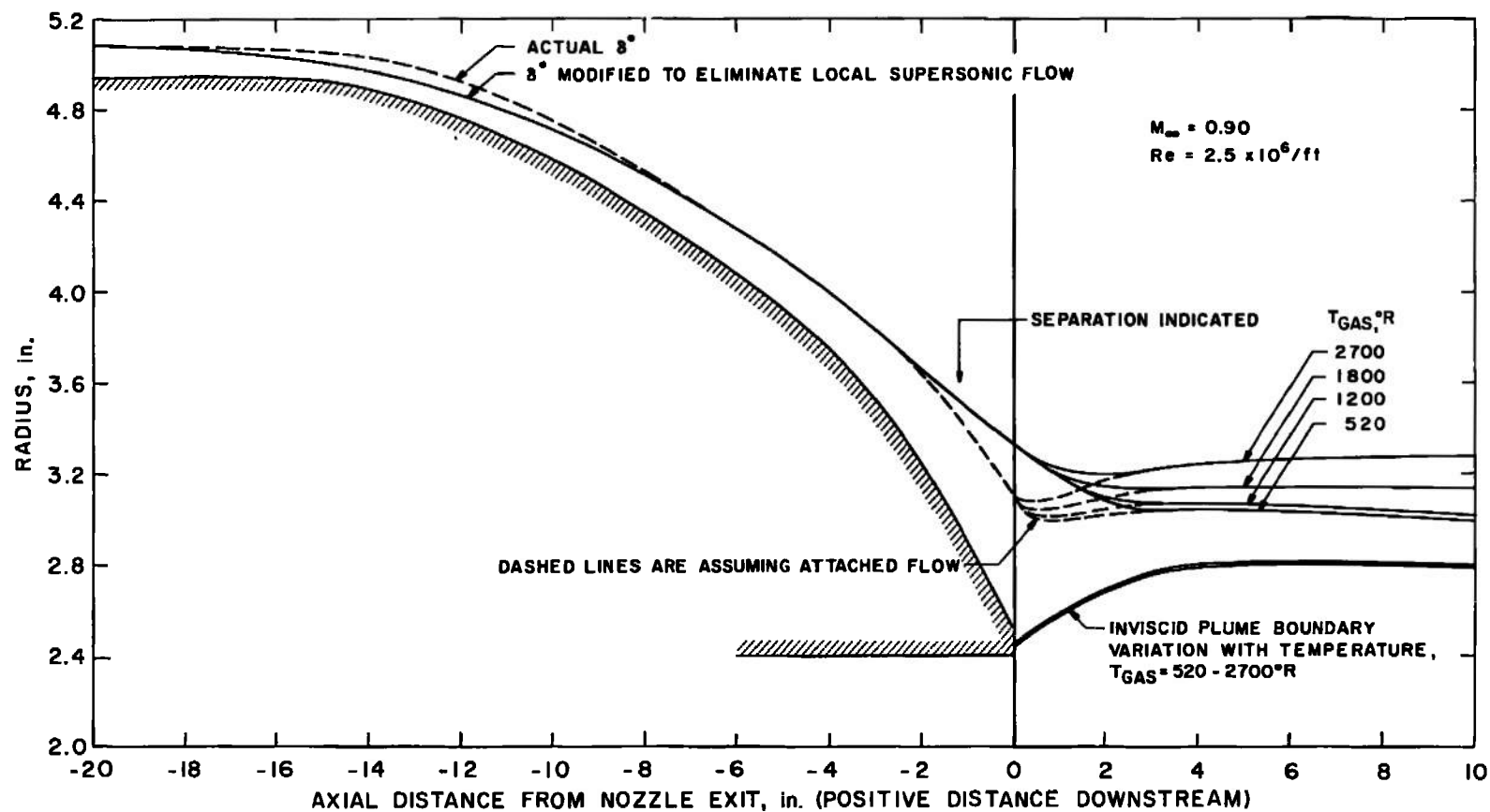


Fig. 25 Effective Displacement Boundaries for the External Flow at  $M_\infty = 0.9$  and  $Re = 2.5 \times 10^6/ft$

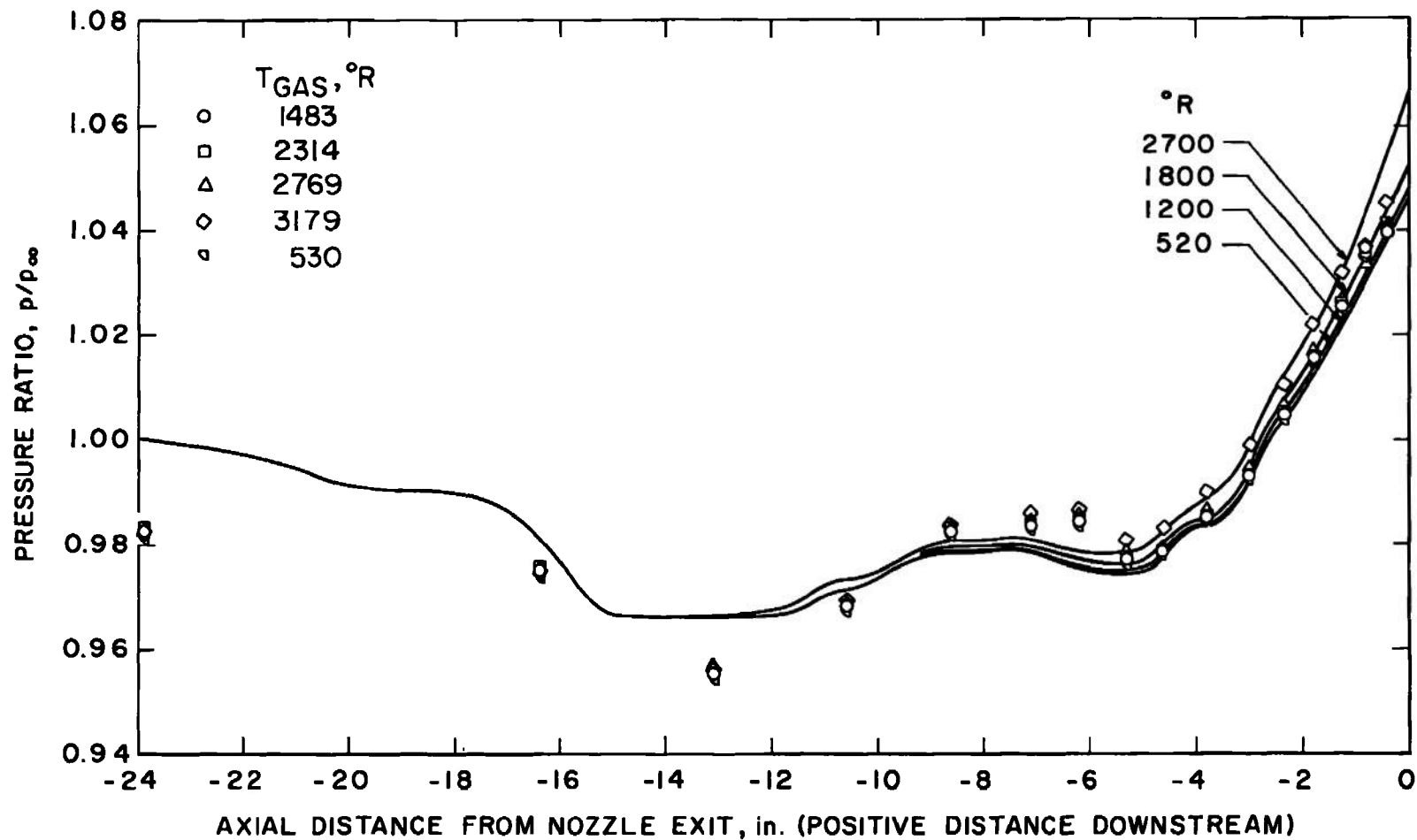


Fig. 26 Afterbody Pressure Distribution: Comparison Between Experiment and Theory for Various Plume Temperatures at  $M_\infty = 0.6$  and  $Re = 2.5 \times 10^6/ft$

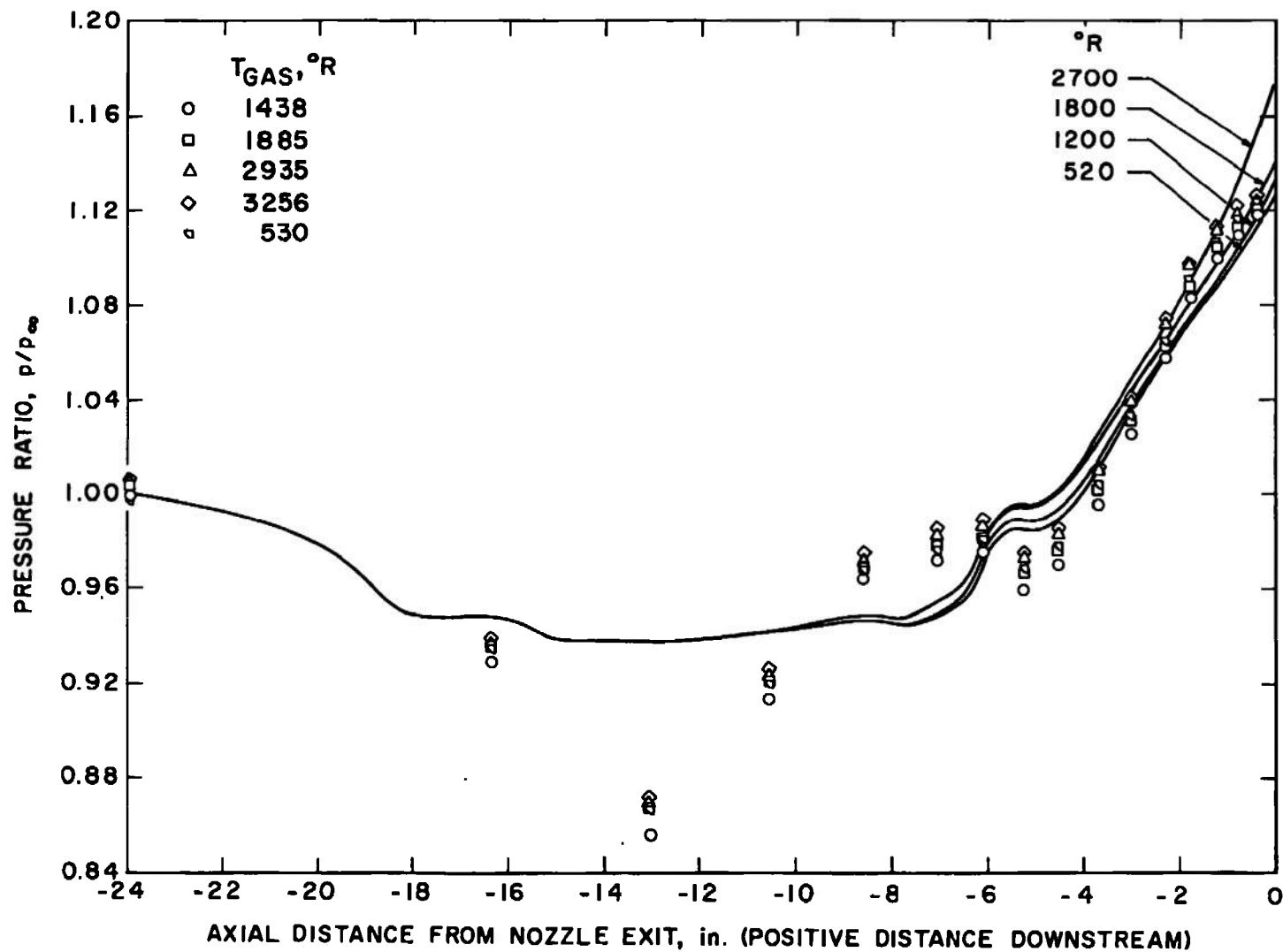


Fig. 27 Afterbody Pressure Distribution: Comparison Between Experiment and Theory for Various Plume Temperatures at  $M_\infty = 0.9$  and  $Re = 2.5 \times 10^6/\text{ft}$

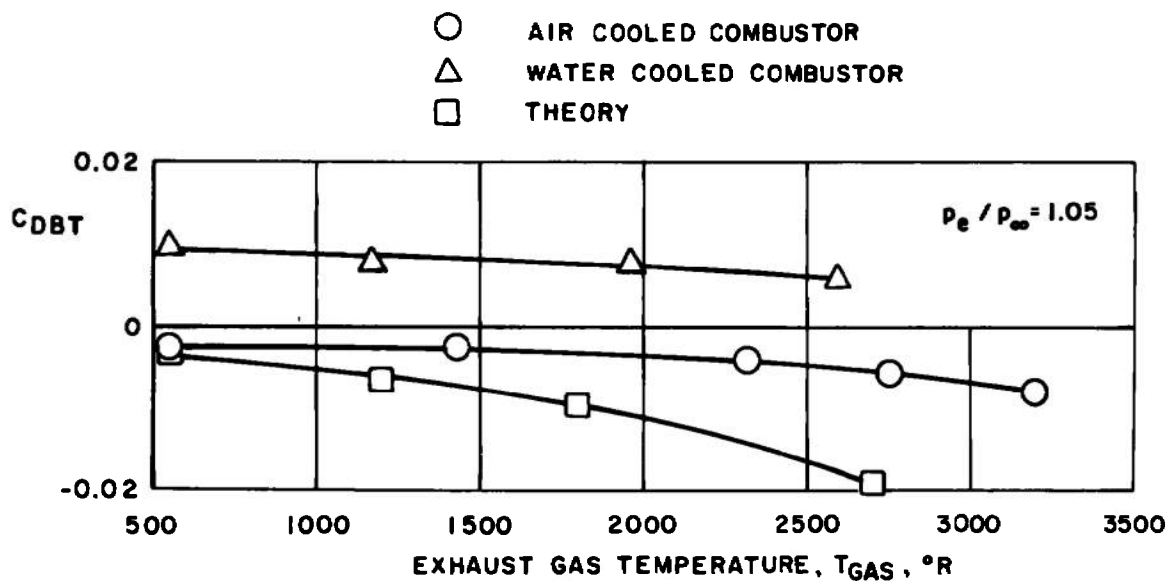
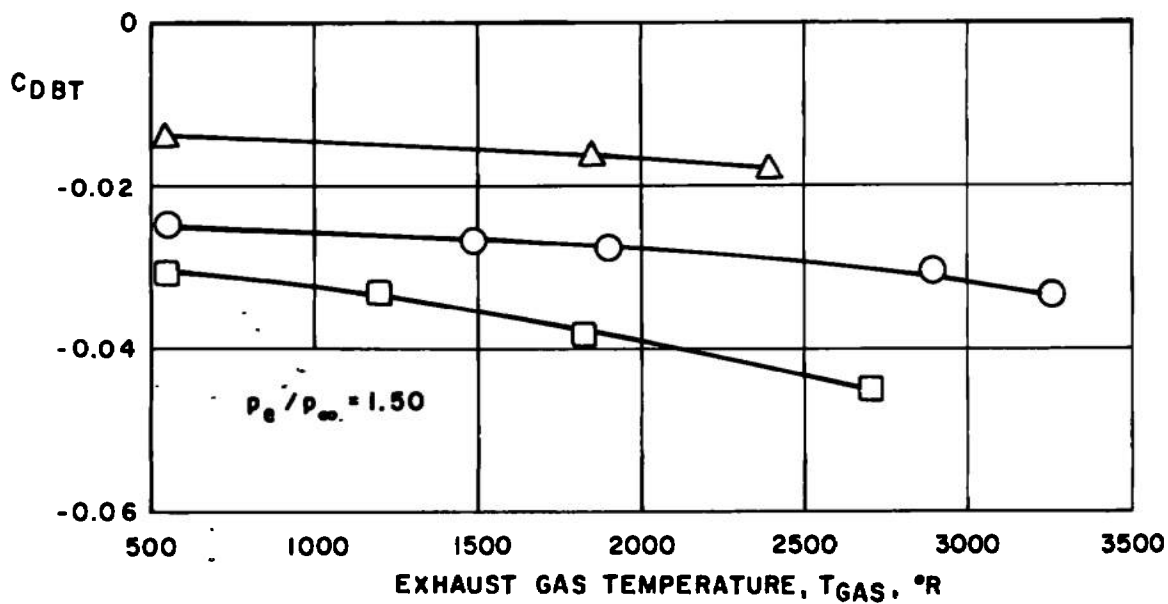
a.  $M_\infty = 0.6$ b.  $M_\infty = 0.9$ 

Fig. 28. Comparison of Theoretical and Experimental Boattail Drag Coefficients at  $Re = 2.5 \times 10^6/ft$

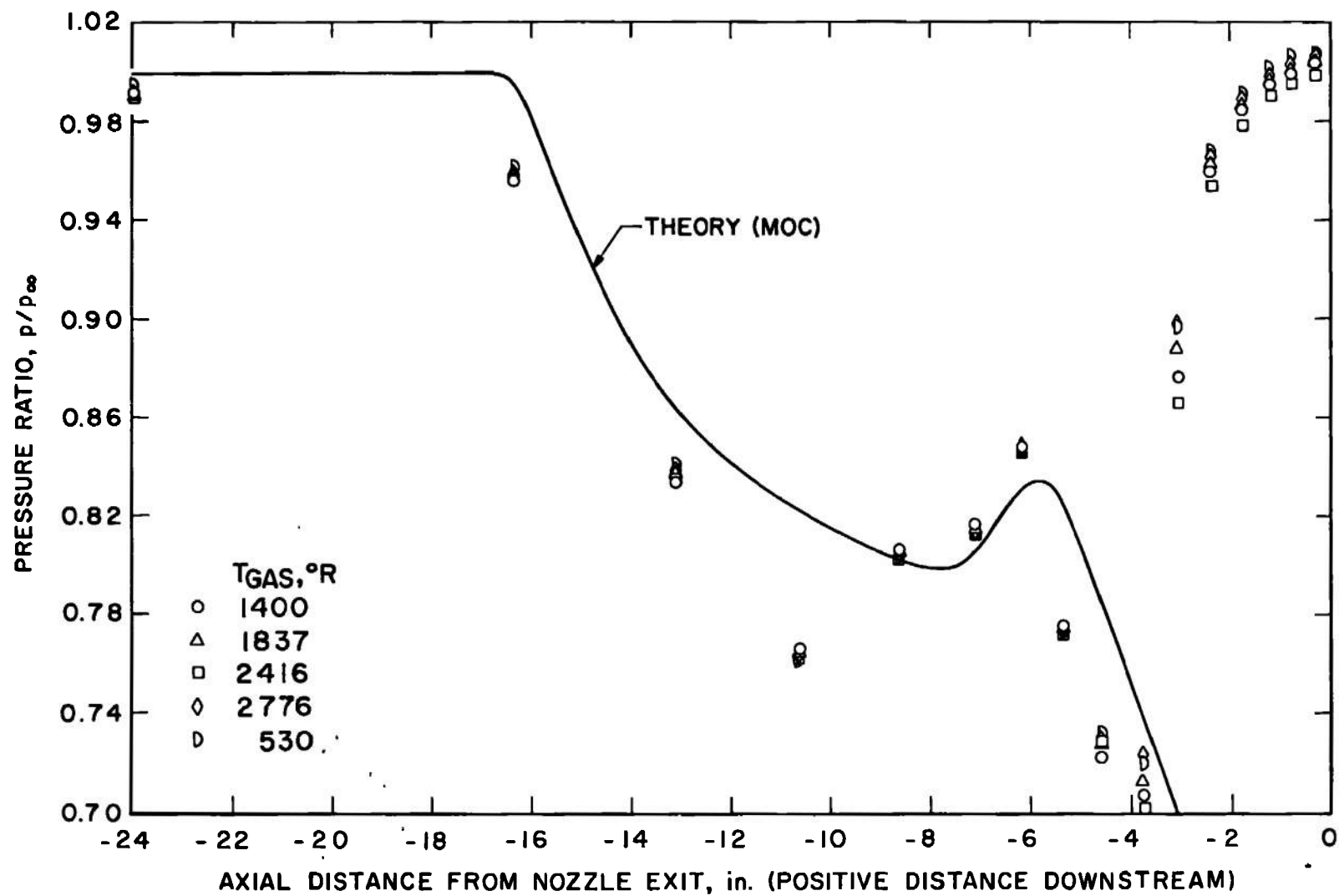


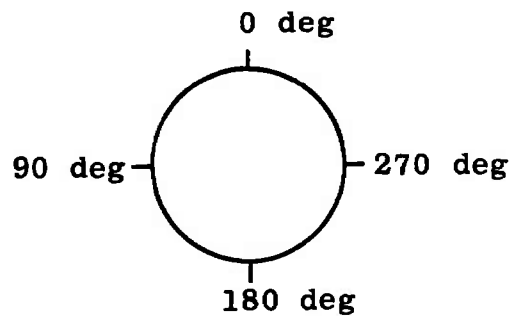
Fig. 29 Afterbody Pressure Distribution: Comparison Between Experiment and Theory for  $M_\infty = 1.2$  and  $Re = 2.5 \times 10^6/ft$

**TABLE I**  
**MEASUREMENT UNCERTAINTY**

Parameter	Uncertainty
Boattail Balance	
$F_N$	$\pm 0.95$ lbf
$F_Y$	$\pm 0.36$ lbf
$F_A$	$\pm 0.39$ lbf
$M_m$	$\pm 1.05$ in.-lbf
Afterbody Balance	
$F_N$	$\pm 7.41$ lbf
$F_Y$	$\pm 2.79$ lbf
$F_A$	$\pm 0.24$ lbf
$M_m$	$\pm 1.09$ in.-lbf
Boattail Static Pressures	$\pm 1.08$ psf
Nozzle Exit Static Pressures	$\pm 12.96$ psf
Air Venturi Plenum Pressure	$\pm 1.5$ psi
Ethylene Venturi Plenum Pressure	$\pm 1.5$ psi
Air Venturi Plenum Temperature	$\pm 1.5^\circ\text{R}$
Ethylene Venturi Plenum Temperature	$\pm 1.5^\circ\text{R}$
Air Venturi Flow Rate	$\pm 0.93$ percent
Ethylene Venturi Flow Rate	$\pm 0.93$ percent

**TABLE II**  
**NOZZLE BOATTAIL SURFACE PRESSURE INSTRUMENTATION**

Model Station, in.	Angle Orientation, deg					
	0	45	90	135	180	270
148.101	403	412	417	426	431	440
148.811	404		418		432	441
149.591	405	413	419	427	433	442
150.281	406		420		434	443
150.941	407	414	421	428	435	444
151.531	408		422		436	445
152.071	409	415	423	429	437	446
152.531	410		424		438	447
152.951	411	416	425	430	439	448

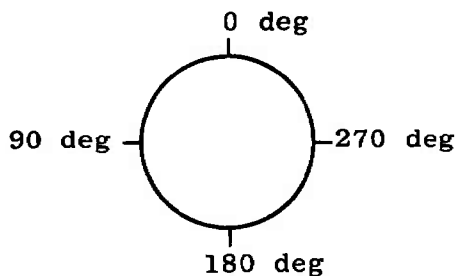


View Looking Upstream



**TABLE III**  
**FOREBODY AND AFTERBODY SURFACE PRESSURE INSTRUMENTATION**

Model Station, in.		Angle Orientation, deg					
		0	~20	90	180	~200	270
Forebody	15.00	503		504	505		506
	29.58	507					
	41.50	508					
	54.00	509					
	66.00	510					
	78.00	511			512		
	92.00	513			514		
	103.00	515			516		
	110.51		601			606	
	114.89		602			607	
	119.26		603			608	
	123.64		604			609	
	128.01		605			610	
	129.20	520			521		
Afterbody	136.97	522		528	531		537
	140.22	523			532		
	142.72	524		529	533		538
	144.72	525			534		
	146.22	526			535		
	147.22	527		530	536		539



View Looking Upstream

**TABLE IV  
BOUNDARY CONDITIONS**

Region	Boundary-Condition Type	Region from Which Boundary Condition Is Imposed
A	Solid Boundary Solid Boundary	C E
B	Solid Boundary Solid Boundary	D E
C	Pressure Gradient	A
D	Pressure Gradient	B
E	Axial Pressure Gradient Reference Line	A and B Match Pressure (Transverse) between A and B

**TABLE V  
COMPUTATIONAL METHODS**

Region	Description	Characteristics	Method
A	Internal Nozzle Flow and Plume	Inviscid - Supersonic	Lockheed MOC
B	External Flow (Isolated Nozzle)	Inviscid a. Subsonic b. Supersonic	a. Pratt & Whitney Transonic Flow Program b. Lockheed MOC
C	Nozzle Boundary Layer	Viscous	Patankar Option I
D	External Boundary Layer	Viscous	Patankar Option I
E	Mixing Layer	Viscous	Patankar Option II

UNCLASSIFIED

Security Classification

## DOCUMENT CONTROL DATA - R &amp; D

(Security classification of title, body of abstract and indexing annotation must be entered when the overall report is classified)

1. ORIGINATING ACTIVITY (Corporate author) Arnold Engineering Development Center Arnold Air Force Station, Tennessee 37389		2a. REPORT SECURITY CLASSIFICATION UNCLASSIFIED	
		2b. GROUP N/A	
3. REPORT TITLE EXHAUST PLUME TEMPERATURE EFFECTS ON NOZZLE AFTERBODY PERFORMANCE OVER THE TRANSONIC MACH NUMBER RANGE			
4. DESCRIPTIVE NOTES (Type of report and inclusive dates) Final Report -- April 4 through 11, 1973			
5. AUTHOR(S) (First name, middle initial, last name) C. E. Robinson, M. D. High, and E. J. Felderman, ARO, Inc.			
6. REPORT DATE July 1974		7a. TOTAL NO. OF PAGES 82	7b. NO. OF REFS 10
8a. CONTRACT OR GRANT NO.  b. PROJECT NO. 5975  c. Program Element 63741F  d.		9a. ORIGINATOR'S REPORT NUMBER(S) AEDC-TR-74-9  9b. OTHER REPORT NO(S) (Any other numbers that may be assigned this report) ARO-PWT-TR-73-112	
10. DISTRIBUTION STATEMENT  Approved for public release; distribution unlimited.			
11. SUPPLEMENTARY NOTES  Available in DDC.		12. SPONSORING MILITARY ACTIVITY Arnold Engineering Development Center Arnold Air Force Station, TN 37389	
13. ABSTRACT Results of an experimental and analytical research investigation on nozzle/afterbody drag are presented. Experimental afterbody (and boattail) drag coefficients and pressure distributions are discussed for an isolated, strut-mounted nozzle/afterbody model for the Mach number range from 0.6 to 1.5. Some data are also given for free-stream unit Reynolds numbers from one million to approximately four million per foot. The experimental data were obtained for the basic model with an air-cooled and a water-cooled Ethylene®/air combustor to provide hot-jet duplication as well as cold-jet simulation. The temperature of the nozzle exhaust gas was varied from 530°R (burner-off) to approximately 2100°R for several nozzle pressure ratios from jet-off to those corresponding to a moderately under-expanded exhaust plume. The initial series of experiments was conducted with the air-cooled combustor, and the effect of jet temperature on afterbody drag was somewhat masked by the effects of the secondary airflow from the cooling air. The general trend, however, shows a decreasing afterbody drag with increasing exhaust gas temperature and with decreasing secondary airflow at a fixed nozzle pressure ratio. The results from the water-cooled combustor show similar trends except that a maximum in the afterbody drag occurs at some intermediate exhaust gas temperature between 530 and 2100°R. This temperature appears to be a function of the free-stream Mach number. The differences between the cold-jet and hot-jet results are significant, and adjusting the cold-jet pressure ratio to correct for the changes in the jet specific heat ratio with temperature will not account for the differences observed. A parallel analytical investigation is described which attempts to predict the afterbody drag of isolated nozzle/afterbody configurations.			

DD FORM 1 NOV 65 1473

UNCLASSIFIED

Security Classification

**UNCLASSIFIED**

**Security Classification**

14.	KEY WORDS	LINK A		LINK B		LINK C	
		ROLE	WT	ROLE	WT	ROLE	WT
	wind tunnels						
	turbojet exhaust nozzles						
	turbofan engines						
	nozzle flow						
	transonic flow						
	pressure drag						
	aerodynamic drag						

**UNCLASSIFIED**

**Security Classification**